Correlated Double Ionization of the C_{60} Fullerene in Short Intense Laser Pulses

Masterarbeit
Zur Erlangung des akademischen Grades Master of Science

Eingereicht von: B. Sc. Ingmar Fabian Schubert

Gutachter: Prof. Dr. Alejandro Saenz
Prof. Dr. Thomas Brabec

Eingereicht am Institut für Physik der Humboldt-Universität zu Berlin am 23. April 2019

Abstract

Strong electromagnetic fields produced by a laser can be used to ionize molecules and atoms. This offers an interesting opportunity to design experiments that allow to probe for physical properties of the target and of the ionization process itself. This thesis in particular is concerned with ionization processes removing two electrons from the C_{60} fullerene during a very short time window that only lasts for half a cycle of the ionizing electromagnetic field. Due to this temporal confinement, such an experiment might reveal correlation effects between the photoelectrons. The Coulomb blockade effect, i.e. the suppression of double ionization due to the Coulomb interaction of the escaping electrons with each other, is especially interesting in this context. The C_{60} fullerene is a promising candidate for such an experiment due to its unique combination of size and high symmetry.

To provide a better theoretical understanding of the processes involved, a quantum mechanical model for single as well as correlated sequential and correlated simultaneous double ionization of the C_{60} fullerene in intense infrared half-cycle laser pulses is developed. The model is based on an extension to the method of steepest descent applied to the strong-field approximation. The results for single ionization are compared to a full solution of the time-dependent Schrödinger equation for a model potential. The results for double ionization are discussed with a special focus on the influence of the Coulomb blockade effect. Due to its analytical simplicity, the model allows for a more general discussion of the Coulomb blockade effect during the ionization of large molecules in intense half-cycle pulses.

Contents

Chapter 1

Introduction

1.1 Ionization of Atoms and Molecules in Electromagnetic Fields

The electromagnetic field of intense lasers, when focused on a target, can be sufficiently strong to create electromagnetic forces that are comparable with the Coulomb attraction of atomic and molecular systems. In this case, the electromagnetic field can change the chemical structure of the system. One of these changes is its single or multiple ionization, i.e. the removal of one or multiple electrons from the parent ion.

Since atoms and molecules are physical systems which, due to their size and energy scale, usually have to be described quantum mechanically, in many cases the ionization process of these systems has to be treated quantum mechanically as well. Indeed, after the quantum theory was established, it was applied to ionization processes of atoms and molecules, the first work of this kind being published by Oppenheimer in 1928 [1], where he correctly described the exponential dependency of the ionization rate of hydrogen in a weak and static electric field on the field strength. However, experimental verification of such experiments was not possible until the realization of the first laser [2] by Maiman in 1960. Ever since the laser has made ionization experiments of atoms and molecules possible, they — and their theoretical description — have been in the focus of scientific interest, as they offer a direct possibility to test predictions of quantum theory and its approximations.

A particular direction of the research around ionization experiments is fueled by the advances in the creation of laser fields with increasingly shorter pulse durations (see [3] for an overview). This opens up opportunities to perform time-resolved ionization experiments with increasingly high time resolution, granting access to physical processes happening on increasingly short time scales.

1.2 Ionization of the C_{60} Fullerene in Electromagnetic Fields

The C_{60} fullerene is a molecule consisting of 60 carbon atoms that are arranged in pentagons and hexagons to an icosahedral structure (see fig. 1.1). It was first synthesized by Kroto et al. [5] by evaporating graphite using a laser. For the discovery of C_{60} and other fullerenes, R. F. Curl, H. W. Kroto, and R. E.

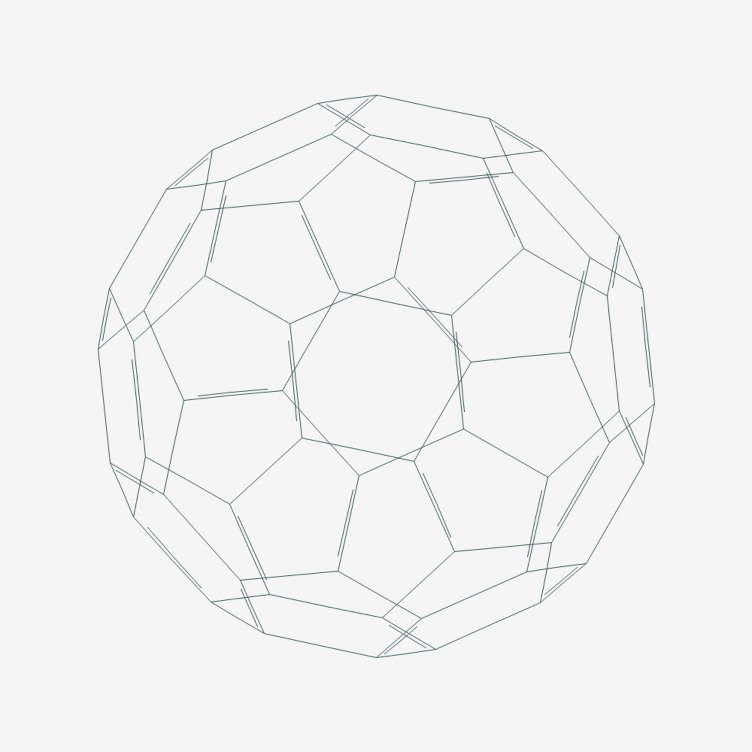

FIGURE 1.1: Chemical structure of C_{60} [4].

Smalley were awarded the 1996 Nobel Prize in Chemistry. The carbon atoms are sp_2-hybridized, the π-bonds being delocalized over the surface. Hence, there is one delocalized π valence electron per atom. The radius of the molecule is approximately 3.5 Å [6].

Its single and double ionization energies are 7.65 eV and 18.98 eV respectively [7], meaning that the second ionization energy is 11.24 eV. Due to the closeness of first and second ionization energies, the ejection of a second electron is not as suppressed compared to the first one as, for example, for atoms.

Together with its high symmetry that allows for relatively easy theoretical description, this makes C_{60} an interesting candidate to perform multi-electron ionization experiments on. Such experiments have already been performed in 2003 by Bhardwaj et al. [8, 9]. However, the ability to produce half-cycle pulses in the near infrared recently developed by the same group [10] now offers an interesting opportunity to examine the single and multiple ionization behavior of C_{60} in short half-cycle pulses. This is particularly interesting because such experiments might reveal correlation effects in multiple ionization.

The naive expectation is that, due to the very short pulse duration, all electrons are confined to escaping from the molecule within a short time window. If after the pulse, more than one electron was removed from the molecule, it is very likely that the electrons "blocked" each other during ionization due to their Coulomb repulsion. As all electrons are more likely to leave the molecule in the direction of the laser pulse, a linearly polarized electromagnetic field forces them into the same direction. In this case, the additional Coulomb interaction of the ejected electrons is added to the ionization potential of the entire process, which should suppress its probability exponentially. This effect is called the Coulomb blockade.

This master's thesis focuses on developing an approximate quantum mechanical model for such an experiment. More specifically, the focus lies on the prediction of double ionization yields and momentum distributions after correlated double ionization, i.e. the simplest case of correlated multiple ionization. The models developed to this end also allow for a more general discussion of correlation effects of two electrons being removed from a large molecule in a very short time window. Thus, this thesis also aims at contributing to a more general understanding of correlated double ionization of large molecules and the influence of parameters like the molecule size and the pulse duration.

This thesis is structured as follows: In chapter 2, an overview over the theoretical background used for the development of the model is given. In chapter 3, a model for single ionization is developed, followed by a validation. This model is generalized to the case of correlated double ionization in chapter 4, followed by a conclusion and discussion of limitations in chapter 5. Details on the numerical implementation are given in the appendices.

Chapter 2

Theoretical Background

Unless explicitly stated otherwise, atomic units are used throughout. This means that all physical quantities are expressed with respect to the base units $\hbar$, e, m_e and $4\pi\epsilon_0$. As these base units form a complete basis set in the subspace of physical quantities spanned by the SI units m, s, kg, and A, this can be done unambiguously. Furthermore, because of this, the units can be left out in the equations unambiguously.

2.1 Quantum-Mechanical Description of Molecules

A molecule is a quantum mechanical system consisting of negatively charged electrons and positively charged atomic nuclei, all interacting with each other via Coulomb forces. Any quantum mechanical system is fully described by its state $|\Psi\rangle$. In the non-relativistic limit applicable for velocity distributions well below the speed of light, the equation of motion for this state is the time-dependent Schrödinger equation (TDSE)

$$\hat{\mathrm{H}}\,|\Psi(t)\rangle = i\partial_t\,|\Psi(t)\rangle \quad . \tag{2.1}$$

The molecule's Hamiltonian $\hat{\mathrm{H}}$ is the sum

$$\hat{\mathrm{H}} = \hat{\mathrm{T}} + \hat{\mathrm{V}} \tag{2.2}$$

of its kinetic energy operator $\hat{\mathrm{T}}$ and its potential energy operator $\hat{\mathrm{V}}$. Consider a molecule with N electrons with mass m_e and P identical nuclei with mass m_n and charge Z. In this case, the kinetic energy operator reads

$$\hat{\mathrm{T}} = \sum_{i=1}^{N} -\frac{1}{2m_e}\vec{\nabla}^2_{\vec{r}_{\mathrm{ele},i}} + \sum_{j=1}^{P} -\frac{1}{2m_n}\vec{\nabla}^2_{\vec{r}_{\mathrm{nuc},j}} \quad , \tag{2.3}$$

and the potential energy operator reads

$$\hat{\mathrm{V}} = \sum_{i=1}^{N}\sum_{j=1}^{P} -\frac{Z}{|\hat{\vec{\mathrm{r}}}_{\mathrm{ele},i} - \hat{\vec{\mathrm{r}}}_{\mathrm{nuc},j}|} + \sum_{i=1}^{N}\sum_{j>i}^{N} \frac{1}{|\hat{\vec{\mathrm{r}}}_{\mathrm{ele},i} - \hat{\vec{\mathrm{r}}}_{\mathrm{ele},j}|} + \sum_{i=1}^{P}\sum_{j>i}^{P} \frac{Z^2}{|\hat{\vec{\mathrm{r}}}_{\mathrm{nuc},i} - \hat{\vec{\mathrm{r}}}_{\mathrm{nuc},j}|} \quad , \tag{2.4}$$

describing the interaction of the electrons with the nuclei, the interaction of the electrons with each other, and the interaction of the nuclei with each other, respectively. With regard to the Born-Oppenheimer approximation introduced later in this chapter, it is convenient to introduce the separation

$$\hat{\mathrm{H}} = \hat{\mathrm{H}}_{\mathrm{ele}} + \hat{\mathrm{T}}_{\mathrm{nuc}} \quad , \tag{2.5}$$

where

$$\hat{\mathrm{T}}_{\mathrm{nuc}} = \sum_{i=1}^{P} -\frac{1}{2m_n} \vec{\nabla}^2_{\vec{r}_{\mathrm{nuc},i}} \tag{2.6}$$

is the kinetic energy operator of the nuclei, and

$$\begin{aligned} \hat{\mathrm{H}}_{\mathrm{ele}} = &\sum_{i=1}^{N} -\frac{1}{2m_e} \vec{\nabla}^2_{\vec{r}_{\mathrm{ele},i}} \qquad\qquad (2.7) \\ &+ \sum_{i=1}^{N}\sum_{j=1}^{P} -\frac{Z}{|\hat{\vec{\mathrm{r}}}_{\mathrm{ele},i} - \hat{\vec{\mathrm{r}}}_{\mathrm{nuc},j}|} + \sum_{i=1}^{N}\sum_{j>i}^{N} \frac{1}{|\hat{\vec{\mathrm{r}}}_{\mathrm{ele},i} - \hat{\vec{\mathrm{r}}}_{\mathrm{ele},j}|} + \sum_{i=1}^{P}\sum_{j>i}^{P} \frac{Z^2}{|\hat{\vec{\mathrm{r}}}_{\mathrm{nuc},i} - \hat{\vec{\mathrm{r}}}_{\mathrm{nuc},j}|} \quad , \end{aligned}$$

the so-called electronic Hamiltonian, contains the rest. For time-independent Hamiltonians like $\hat{\mathrm{H}}$, the TDSE is solved by a set of states

$$|\Psi_n(t)\rangle = e^{-iE_n t} |\Phi_n\rangle \quad , \tag{2.8}$$

where the $|\Phi_n\rangle$ are eigenstates of the Hamiltonian $\hat{\mathrm{H}}$, i.e. they fulfill the time-independent Schrödinger equation (TISE)

$$\hat{\mathrm{H}} |\Phi_n\rangle = E_n |\Phi_n\rangle \quad , \tag{2.9}$$

where the eigenstates $|\Phi_n\rangle$ are states of the $(N + P)$-particle Hilbert space for the entire problem.

2.1.1 Approximate Solution Methods

Except for very few textbook examples for which analytical solutions exist, the Schrödinger equation has to be solved numerically. Numerical solutions of the Schrödinger equation however become exponentially more demanding with respect to storage space and computation time with growing number of particles. For complex quantum mechanical systems like molecules, it is therefore vital to use suitable approximations that simplify this task. The most fundamental one of these approximations, the Born-Oppenheimer approximation, is discussed in the following.

2.1.1.1 Born-Oppenheimer Approximation

Intuitively speaking, the Born-Oppenheimer approximation exploits that due to their much larger mass, the nuclei of a molecule move much slower than its electrons. On the timescale of the electronic motion, the nuclei are almost fixed in space and therefore create a time-independent potential landscape in which the electrons move. Even if this landscape slowly changes over time due to the slow nuclear motion, the electrons are able to follow this change adiabatically.

Within the Born-Oppenheimer approximation, an approximation to the eigenstates $|\Phi_n\rangle$ is found by first solving the electronic problem for fixed nuclei coordinates, i.e. by solving

$$\hat{\mathrm{H}}_{\mathrm{ele}}(\{\vec{r}_{\mathrm{nuc},i}\})\,|\phi_m(\{\vec{r}_{\mathrm{nuc},i}\})\rangle = \epsilon_m(\{\vec{r}_{\mathrm{nuc},i}\})\,|\phi_m(\{\vec{r}_{\mathrm{nuc},i}\})\rangle \quad , \tag{2.10}$$

where $\hat{\mathrm{H}}_{\mathrm{ele}}(\{\vec{r}_{\mathrm{nuc},i}\})$ and $|\phi_m(\{\vec{r}_{\mathrm{nuc},i}\})\rangle$ are an operator and state respectively of the N-particle Hilbert space of the N electrons only, and depend *parametrically* on the nuclei coordinates $\{\vec{r}_{\mathrm{nuc},i}\}$. This means that the electronic problem is solved for the set of Hamiltonians obtained for all $\{\vec{r}_{\mathrm{nuc},i}\}$, which yields a set of eigenvectors $|\phi_m(\{\vec{r}_{\mathrm{nuc},i}\})\rangle$ and eigenstates $\epsilon_m(\{\vec{r}_{\mathrm{nuc},i}\})$ as a function of the nuclear coordinates.

The operator

$$\hat{\mathrm{H}}^{(m)}_{\mathrm{nuc}} = \hat{\mathrm{T}}_{\mathrm{nuc}} + \epsilon_m(\{\hat{\vec{\mathrm{r}}}_{\mathrm{nuc},i}\}) \quad , \tag{2.11}$$

where the function $\epsilon_m(\{\hat{\vec{\mathrm{r}}}_{\mathrm{nuc},i}\})$ is now a function of the position operators $\{\hat{\vec{\mathrm{r}}}_{\mathrm{nuc},i}\}$, i.e. a potential operator, is an operator acting on the P-particle Hilbert space of the nuclear degrees of freedom, and its eigenstates and eigenvalues are

$$\hat{\mathrm{H}}^{(m)}_{\mathrm{nuc}}\,|\chi^{(m)}_q\rangle = E^{(m)}_q\,|\chi^{(m)}_q\rangle \quad . \tag{2.12}$$

For a single quantum number m, the states $\{|\chi^{(m)}_q\rangle\}^{\infty}_{q=1}$ form a complete set of the P-particle Hilbert space of the nuclear coordinates (due to the fact that $\hat{\mathrm{H}}^{(m)}_{\mathrm{nuc}}$ is hermitian). For the same reason, $\{|\phi_m(\{\vec{r}_{\mathrm{nuc},i}\})\rangle\}^{\infty}_{m=1}$ for a single value of $\{\vec{r}_{\mathrm{nuc},i}\}$ form a complete set of the N-particle Hilbert space of the electronic coordinates. Hence, the eigenstates $|\Phi_n\rangle$ of the complete Hamiltonian $\hat{\mathrm{H}}$ can be expanded in configurations according to

$$|\Phi_n\rangle = \sum_k c_{nk}\,|\gamma_k\rangle \quad , \tag{2.13}$$

where

$$|\gamma_k\rangle = \int \mathrm{d}^{3P} r_{\mathrm{nuc}}\ \ \langle\{\vec{r}_{\mathrm{nuc},i}\}|\chi^{(m_k)}_{q_k}\rangle\,|\{\vec{r}_{\mathrm{nuc},i}\}\rangle \otimes |\phi_{m_k}(\{\vec{r}_{\mathrm{nuc},i}\})\rangle \quad , \tag{2.14}$$

where $\{|\{\vec{r}_{\mathrm{nuc},i}\}\rangle\}$ is the position-space basis of the nuclear Hilbert space. One could allow an arbitrary choice of m_0 in $|\chi^{(m_0)}_{q_k}\rangle$ as well, because the nuclear basis is complete for each value of m_0. However, without loss of generality, m_k, i.e. the quantum number of the electronic part, is chosen here, which will prove more useful later. Notice that the nuclei are distinguishable from the electrons, therefore no (anti-) symmetrization between the nuclear and the electronic degrees of freedom is needed.

So far, no approximation has been introduced, and eq. (2.13) is a correct and complete ansatz for the solution of the time-independent Schrödinger equation for the entire problem in eq. (2.9). Insertion of the ansatz into the TISE yields

$$
\begin{aligned}
\hat{\mathrm{H}}\,|\Phi_n\rangle &= \hat{\mathrm{H}}_{\mathrm{ele}}\,|\Phi_n\rangle + \hat{\mathrm{T}}_{\mathrm{nuc}}\,|\Phi_n\rangle \qquad (2.15)\\
&= \sum_k c_{nk} \int \mathrm{d}^{3P} r_{\mathrm{nuc}} \;\; \langle\{\vec{r}_{\mathrm{nuc},i}\}|\chi_{qk}^{(m_k)}\rangle \, \Big[\hat{\mathrm{H}}_{\mathrm{ele}}\,|\{\vec{r}_{\mathrm{nuc},i}\}\rangle \otimes |\phi_{m_k}(\{\vec{r}_{\mathrm{nuc},i}\})\rangle \\
&\qquad + \hat{\mathrm{T}}_{\mathrm{nuc}}\,|\{\vec{r}_{\mathrm{nuc},i}\}\rangle \otimes |\phi_{m_k}(\{\vec{r}_{\mathrm{nuc},i}\})\rangle\,\Big]. \qquad (2.16)
\end{aligned}
$$

Notice that in this case, $\hat{\mathrm{H}}_{\mathrm{ele}}$ is not parametrically dependent on the core coordinates, but acts as an operator in the entire $(N+P)$-particle Hilbert space. As the nuclear degrees of freedom only occur as position-space operators in the potential energy in $\hat{\mathrm{H}}_{\mathrm{ele}}$, it is already diagonal in the position-space basis in this subspace, and one obtains

$$
\hat{\mathrm{H}}_{\mathrm{ele}}\,|\{\vec{r}_{\mathrm{nuc},i}\}\rangle \otimes |\phi_{m_k}(\{\vec{r}_{\mathrm{nuc},i}\})\rangle = \epsilon_{m_k}(\{\vec{r}_{\mathrm{nuc},i}\})\,|\{\vec{r}_{\mathrm{nuc},i}\}\rangle \otimes |\phi_{m_k}(\{\vec{r}_{\mathrm{nuc},i}\})\rangle \quad , \tag{2.17}
$$

which leads to

$$
\begin{aligned}
\hat{\mathrm{H}}\,|\Phi_n\rangle = \sum_k c_{nk} \int \mathrm{d}^{3P} r_{\mathrm{nuc}} \;\; \langle\{\vec{r}_{\mathrm{nuc},i}\}|\chi_{qk}^{(m_k)}\rangle \qquad (2.18)\\
\Big[\hat{\mathrm{T}}_{\mathrm{nuc}} + \epsilon_{m_k}(\{\vec{r}_{\mathrm{nuc},i}\})\Big]\,|\{\vec{r}_{\mathrm{nuc},i}\}\rangle \otimes |\phi_{m_k}(\{\vec{r}_{\mathrm{nuc},i}\})\rangle
\end{aligned}
$$

In the physical picture of the Born-Oppenheimer approximation, the electrons move so fast compared to the nuclei that the nuclei aren't sensitive to the dynamic motion, but only feel an averaged potential energy due to the electronic cloud that follows the nuclear motion adiabatically. Therefore, it is assumed that the kinetic energy of the nuclear motion is not modified by the electrons, which means that, intuitively speaking, the electrons don't dynamically pull the nuclei in a certain direction as they move due to their low mass, but they create a mean field that moves the nuclei over time. Formally, this means that

$$
\begin{aligned}
&\hat{\mathrm{T}}_{\mathrm{nuc}}\left(\int \mathrm{d}^{3P} r_{\mathrm{nuc}}\,\langle\{\vec{r}_{\mathrm{nuc},i}\}|\chi_{qk}^{(m_k)}\rangle\,|\{\vec{r}_{\mathrm{nuc},i}\}\rangle \otimes |\phi_{m_k}(\{\vec{r}_{\mathrm{nuc},i}\})\rangle\right) \qquad (2.19)\\
&\overset{\mathrm{B.O.}}{\approx} \int \mathrm{d}^{3P} r_{\mathrm{nuc}}\,\langle\{\vec{r}_{\mathrm{nuc},i}\}|\hat{\mathrm{T}}_{\mathrm{nuc}}|\chi_{qk}^{(m_k)}\rangle\,|\{\vec{r}_{\mathrm{nuc},i}\}\rangle \otimes |\phi_{m_k}(\{\vec{r}_{\mathrm{nuc},i}\})\rangle \quad , \qquad (2.20)
\end{aligned}
$$

i.e. the state of the system is factorized into a nuclear part and an electronic part, and, because of

$$
\epsilon_{m_k}(\{\vec{r}_{\mathrm{nuc},i}\})\,\langle\{\vec{r}_{\mathrm{nuc},i}\}| = \langle\{\vec{r}_{\mathrm{nuc},i}\}|\,\epsilon_{m_k}(\{\hat{\vec{\mathrm{r}}}_{\mathrm{nuc},i}\}) \quad , \tag{2.21}
$$

it follows — and here it comes in handy that the same m_k was chosen for the electronic and the nuclear part in the ansatz in eq. (2.14) — that

$$\begin{aligned}
\hat{\mathrm{H}}\,|\Phi_n\rangle &= \sum_k c_{nk} \int \mathrm{d}^{3P} r_{\mathrm{nuc}} \quad \langle\{\vec{r}_{\mathrm{nuc},i}\}|\hat{\mathrm{H}}^{(m_k)}_{\mathrm{nuc}}|\chi^{(m_k)}_{q_k}\rangle \\
&\qquad\qquad |\{\vec{r}_{\mathrm{nuc},i}\}\rangle \otimes |\phi_{m_k}(\{\vec{r}_{\mathrm{nuc},i}\})\rangle && (2.22)\\
&= \sum_k c_{nk} E^{(m_k)}_{q_k} \\
&\quad \int \mathrm{d}^{3P} r_{\mathrm{nuc}} \quad \langle\{\vec{r}_{\mathrm{nuc},i}\}|\chi^{(m_k)}_{q_k}\rangle\,|\{\vec{r}_{\mathrm{nuc},i}\}\rangle \otimes |\phi_{m_k}(\{\vec{r}_{\mathrm{nuc},i}\})\rangle && (2.23)\\
&= \sum_k c_{nk} E^{(m_k)}_{q_k}\,|\gamma_k\rangle \quad . && (2.24)
\end{aligned}$$

The meaning of this equation is that within the Born-Oppenheimer approximation, every single configuration $|\gamma_k\rangle$ is an approximate eigenstate to the complete Hamiltonian $\hat{\mathrm{H}}$:

$$\hat{\mathrm{H}}\,|\gamma_k\rangle = E^{(m_k)}_{q_k}\,|\gamma_k\rangle \quad . \tag{2.25}$$

Therefore, within the the Born-Oppenheimer approximation, it is sufficient to solve the electronic problem for only parametric nuclear coordinates, as in eq. (2.10), and then use the resulting energy landscape $\epsilon_m(\{\vec{r}_{\mathrm{nuc},i}\})$ as the potential to solve the nuclear problem in eq. (2.12), from which the eigenenergies $E^{(m)}_q$ are directly obtained along with the eigenstates $|\gamma_k\rangle$ according to eq. (2.14).

As already mentioned, numerical simulations of the Schrödinger equation become exponentially more demanding with respect to storage space and computation time with growing number of particles. Therefore, the Born-Oppenheimer approximation is very important, as it allows one to solve the N-particle problem of the electronic wave function separately from the P-particle problem of the nuclear wave function, instead of solving the complete $(N+P)$-body problem. Because the assumption that the electronic wave functions follows the nuclear motion adiabatically is usually fulfilled very well, this offers an opportunity to accurately simulate quantum mechanical systems for which a simulation would not be feasible otherwise. For example, the 4-body problem (or 3-body problem in center-of-mass (COM) coordinates) of the H_2 or similar molecules can be simplified to a $(2+2)$-body problem using the Born-Oppenheimer approximation. Combining the use of COM coordinates and the exploitation of symmetries, numerical simulations become feasible [11–15].

However, for more complex molecules, even the isolated electronic and nuclear problems become too hard to be fully solved numerically. In this case, approximations have to be introduced, like the Hartee-Fock approximation, which consists of finding a single configuration approximating the real many-configuration states of the N-body problem best, in the sense that it creates the lowest (and therefore, according to the variational principle, the most accurate) ground state energy. In the present case of C_{60}, a model assumption for the ground state is used, namely the rigid-rotor model.

2.1.1.2 Rigid-Rotor-Model of C_{60}

Within the rigid-rotor-model [16], the electrons of C_{60} are described as free particles that don't interact and move on a sphere of fixed radius r_0, i.e. they are described as a free 2D electron gas on a sphere. The Hamiltonian of such a system is the purely angular kinetic energy operator

$$\hat{\mathrm{H}}_0 = -\frac{1}{2m_e r_0^2}\Delta_{\theta,\phi} = -\frac{1}{2m_e r_0^2}\left(\frac{1}{\sin(\theta)}\frac{\partial}{\partial\theta}\left(\sin(\theta)\frac{\partial}{\partial\theta}\right) + \frac{1}{\sin^2(\theta)}\frac{\partial^2}{\partial\phi^2}\right) \quad , \tag{2.26}$$

whose eigenstates $|l, m\rangle$ fulfill

$$\hat{\mathrm{H}}_0 |l, m\rangle = E_l |l, m\rangle \tag{2.27}$$

and have the position-space representations

$$\langle\vec{r}|l, m\rangle = \frac{1}{r_0}\delta(r - r_0)Y_{lm}(\theta, \phi) \quad , \tag{2.28}$$

where

$$Y_{lm}(\theta, \phi) = \frac{1}{\sqrt{2\pi}} N_{lm} P_{l|m|}(\cos(\theta))e^{im\phi} \tag{2.29}$$

are the spherical harmonics with the associated Legendre polynomials

$$P_{lm}(x) = (-1)^m (1 - x)^2 \frac{\mathrm{d}^m}{\mathrm{d}x^m} P_l(x) \quad , \tag{2.30}$$

$P_l(x)$ are the Legendre polynomials, and

$$N_{lm} = (-1)^{\Theta(-m)m}\sqrt{\frac{2l + 1}{2}\frac{(l - |m|)!}{(l + |m|)!}} \tag{2.31}$$

is the normalization factor resulting from the normalization convention

$$\int \mathrm{d}\theta \int \mathrm{d}\phi \; \sin(\theta)Y^*_{l'm'}(\theta, \phi)Y_{lm}(\theta, \phi) = \delta_{ll'}\delta_{mm'} \quad . \tag{2.32}$$

The corresponding eigenenergies are

$$E_l = \frac{l(l + 1)}{2m_e r_0^2} \quad . \tag{2.33}$$

As pointed out in [16], the model assumes that the states are populated by the 60 π-electrons of C_{60}. In the ground state, they fill the states up to $l = 5$, where the last ($l = 5$)-level is filled with 10 electrons. Therefore, the highest occupied molecular orbit (HOMO) and lowest unoccupied molecular orbit (LUMO) correspond to $l = 5$ and $l = 6$, respectively. Assuming a radius of 3.5 Å [6], this results in a first allowed transition of 3.73 eV, which agrees quite well with experimental results that suggest 3.0 eV to 3.8 eV (see also [16]).

2.1.1.2.1 Symmetry adaption of the rigid-rotor eigenstates The Hamiltonian in the rigid-rotor model obviously has spherical symmetry, however C_{60} is not perfectly spherical. Instead, it has a discrete 60-fold rotational symmetry, and therefore is a regular icosahedron. When constructing the symmetry-adapted functions for the 11-fold degenerate ($l = 5$)-subspace, it splits up in 5 fully occupied lower-lying states denoted by H_u and $3 + 3$ unoccupied higher-lying states denoted by T_{1u} and T_{2u} [17]. Those symmetry-adapted states $|l, u\rangle$ can be constructed from the spherical harmonics using the coefficients in [17],

$$|l, u\rangle = \sum_m c_{um} |l, m\rangle \quad . \tag{2.34}$$

For the HOMO states, $l = 5$ and u can be one of the 5 H_u-states denoted by θ, ϵ, ξ, η, and ζ.

2.1.2 Numerical Solution in a Finite Basis

Consider an arbitrary Hamiltonian $\hat{\mathrm{H}}$, e.g. describing a molecule as in eq. (2.2), and a discrete basis $\{|i\rangle\}$ of the same Hilbert space. Because $\{|i\rangle\}$ is a basis, for every state $|\psi_p\rangle$ of its Hilbert space, there exists a *unique* vector of coefficients $\{\mathbb{C}_{ip}\}_{i=0}^{\infty}$ such that

$$|\psi_p\rangle = \sum_i \mathbb{C}_{ip} |i\rangle \quad . \tag{2.35}$$

Using this, the equation

$$\sum_j \langle i|\hat{\mathrm{H}}|j\rangle\, \mathbb{C}_{jp} = E_p \sum_j \langle i|j\rangle\, \mathbb{C}_{jp} \tag{2.36}$$

follows from the TISE (2.9) after multiplying it with $\langle i|$ from the left side. This allows for the reformulation of the Schrödinger equation as a generalized discrete eigenvector problem (in general with infinite dimensions) according to

$$\mathbb{HC} = \mathbb{ESC} \quad , \tag{2.37}$$

where $\mathbb{H}$ is the Hamiltonian matrix with the coefficients

$$\mathbb{H}_{ij} = \langle i|\hat{\mathrm{H}}|j\rangle \quad , \tag{2.38}$$

$\mathbb{E}$ is a diagonal matrix with the energies on the diagonal

$$\mathbb{E}_{ij} = E_p \delta_{pi} \delta_{pj} \quad , \tag{2.39}$$

and $\mathbb{S}$ is the overlap matrix with the coefficients

$$\mathbb{S}_{ij} = \langle i|j\rangle \quad . \tag{2.40}$$

Notice that this is the general case where $\{|i\rangle\}$ is an arbitrary basis. In the special case of an orthonormal basis, i.e.

$$\mathbb{S}_{ij} = \delta_{ij} \quad , \tag{2.41}$$

the matrix $\mathbb{S}$ is the identity.

While some Hilbert spaces of quantum mechanical systems, like, for example, a spin-$\frac{1}{2}$-system, have finite dimensionality, in general quantum mechanical Hilbert spaces have infinite dimensionality. Discretizing the TISE into a matrix eigenvector problem like in eq. (2.37) using only a finite set of basis states $\{|i\rangle\}$ therefore is an approximation in the general case, regardless of how many states are used. However, by doing so, eq. (2.37) becomes a generalized eigenvalue problem for which standard eigenvector algorithms from linear algebra exist. Depending on the system parameters, the observable one is interested in, and the basis set used, the results converge with the number of basis states used for the discretization.

2.1.2.1 B Spline Basis

B spline basis sets are a special kind of basis sets often used for numerical simulations, and are described in the following. As this is what is used later in this work, the discussion is restricted to the case of a single electron in a spherical potential. The corresponding Hamiltonian of such a particle reads

$$\hat{\mathrm{H}} = \frac{\hat{\mathrm{p}}^2}{2m} + V(r) \quad , \tag{2.42}$$

and, due to the spherical symmetry of $\hat{\mathrm{H}}$, the TISE of the system

$$\hat{\mathrm{H}} \left|\psi_p\right\rangle = E_{n_p l_p} \left|\psi_p\right\rangle \tag{2.43}$$

can be solved by a state $|\psi_p\rangle$ with the position-space representation

$$\langle r, \theta, \phi | \psi_p \rangle = \frac{R_{n_p l_p}(r)}{r} Y_{l_p m_p}(\theta, \phi) \quad , \tag{2.44}$$

where $Y_{lm}(\theta, \phi)$ are the spherical harmonics (see eq. 2.29), and $R_{nl}(r)$ fulfills the radial TISE

$$\left[-\frac{1}{2m} \frac{\mathrm{d}^2}{\mathrm{d}r^2} + V(r) + \frac{1}{2m} \frac{l(l+1)}{r^2} \right] R_{nl}(r) = E_{nl} R_{nl}(r) \quad . \tag{2.45}$$

The choice of basis for such a problem ideally makes use of this symmetry in order to efficiently use numerical resources. A suitable choice of basis functions therefore could be

$$\langle \vec{r} | i \rangle = \frac{B_{\alpha_i}(r)}{r} Y_{l_i m_i}(\theta, \phi) \quad , \tag{2.46}$$

where $B_\alpha(r)$ is a B spline, i.e. a special kind of polynomial function defined on a finite interval. This means that the discretized eigenfunctions take the form (see eq. (2.35))

$$\langle r, \theta, \phi | \psi_p \rangle = \sum_i \mathbb{C}_{ip} \langle r, \theta, \phi | i \rangle \tag{2.47}$$

$$= Y_{l_p m_p}(\theta, \phi) \sum_i \mathbb{C}_{ip} \frac{B_{\alpha_i}(r)}{r} \quad . \tag{2.48}$$

2.1.2.1.1 B splines B splines were first mentioned as such in [18], and have been used for numerical analysis in different fields of atomic and molecular physics. For an extensive overview, please refer to [19]. B splines are polynomial functions mapping from the real interval $I = [a, b]$ to the real numbers that are $\mathcal{L}^2$-integrable, i.e.

$$\int_a^b |f(x)|^2 < \infty \quad . \tag{2.49}$$

A (non-complete) B spline basis $\mathbb{B}$ over an interval $[a, b]$ can be defined by specifying

- its polynomial degree k and
- a tuple of knot positions $K = (x_0 = a, x_1, x_2, ..., x_m = b)$ in non-decreasing order.

The $m+1$ knot positions x_i can occur multiple times with multiplicity $\mu(x_i) \geq 1$. The corresponding B spline basis $\mathbb{B}$ consists of $N = m - k$ B spline functions $B_i(x)$. The i-th B spline $B_i(x) \in \mathbb{B}$ is defined recursively as

$$B_i(x) := B_{i,k}(x) := \frac{x - x_i}{x_{i+k} - x_i} B_{i,k-1}(x) + \frac{x_{i+k+1} - x}{x_{i+k+1} - x_{i+1}} B_{i+1,k-1}(x) \quad . \tag{2.50}$$

$$B_{i,0}(x) := \begin{cases} 1 & \text{if } x_i \leq x \leq x_{i+1} \\ 0 & \text{otherwise} \end{cases} \quad , \tag{2.51}$$

where i is running over $0 \leq i \leq m - k - 1$. The set of *unique* knot positions, i.e. the set

$$P = \{x_i : x_i \in K\} \tag{2.52}$$

is called the breakpoints of the B spline basis.

When B splines are applied to radial wavefunctions like in this work, $a = 0$ and $b = r_{\text{max}}$ are chosen for the boundaries, i.e. the interval is artificially confined to some r_{max}. A common practice for the knot positions is to choose the knot positions $a = 0$ and $b = r_{\text{max}}$ both k times, and to distribute the knot positions between 0 and r_{max} with multiplicity 1 according to a sine law, i.e.

$$\begin{aligned} x_0 = x_1 = \ldots = x_{k-1} &= 0 \\ x_i &= r_{\text{max}} \sin\left(\frac{\pi}{2}\left(\frac{i-k+1}{m-2d+2}\right)^y\right) \quad \text{for} \quad k \leq i \leq m-k \\ x_{m+1-k} = \ldots = x_m &= r_{\text{max}} \quad , \end{aligned} \tag{2.53}$$

where y is chosen such that $x_d = \Delta r$, i.e.

$$y = -\frac{\log\left(\frac{2}{\pi}\arcsin\left(\frac{\Delta r}{r_{\text{max}}}\right)\right)}{\log(m-2d+1)} \quad . \tag{2.54}$$

Here, Δr is a parameter which specifies the first nonzero knot position.

This knot sequence is also used for the calculations done in this work. For example, for the interval $[a = 0, b = r_{\text{max}} = 1]$, a B spline basis of degree $k = 2$ with $N = 6$ basis functions can be obtained using eq. (2.53) with $\Delta r = 0.05$ to

$$K \approx (0, 0, 0.05, 0.19, 0.40, 0.66, 0.89, 1, 1) \quad . \tag{2.55}$$

The corresponding B spline basis, obtained with the `BSplineBasis` function in `Wolfram Mathematica`, is shown in fig. (2.1). A thorough description of the properties of B splines and an overview of applications can be found in [20]

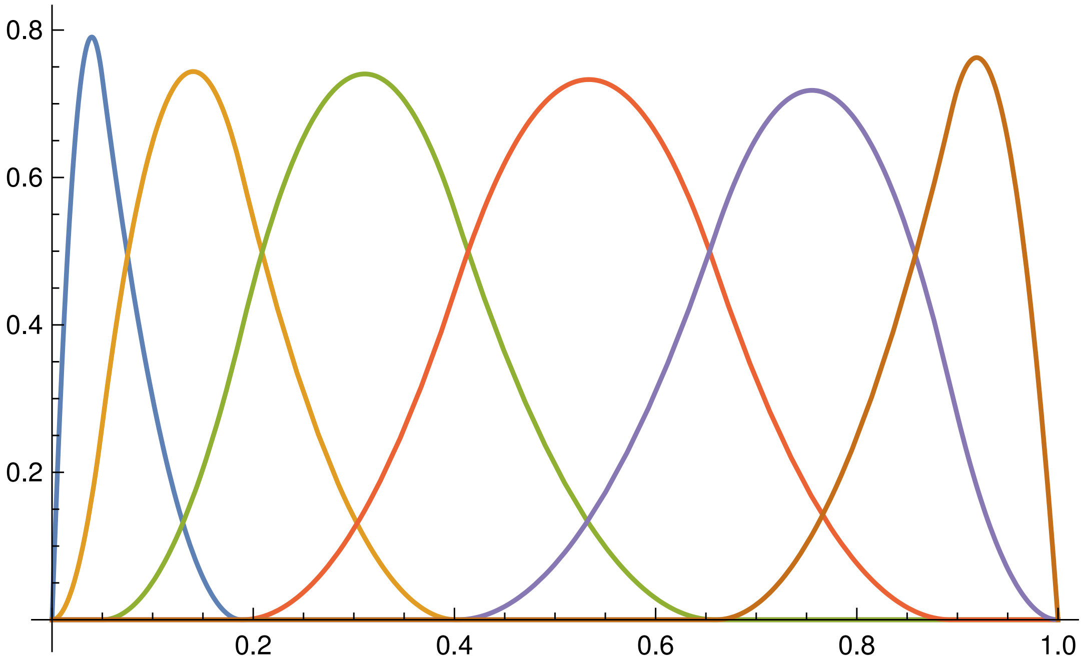

FIGURE 2.1: The $N = 6$ B spline basis functions for the interval $[a = 0, b = 1]$, obtained for degree $k = 2$ and $\Delta r = 0.05$, using the knot sequence in eq. (2.55).

2.1.2.1.2 Boundary conditions As already mentioned, when using B splines as a basis for the radial part $R_{nl}(r)$, the extent of the state is artificially confined to some size r_{max}, if for the interval $[a = 0, b = r_{\text{max}}]$ is chosen. For $r \to 0$, the basis functions in eq. (2.46) have to approach a constant value or go to 0. Therefore, only B splines for which $B_i(x = 0) = 0$ can be included in the basis.

For a bound particle, i.e. a particle being in a state with energy

$$E_{nl} < V(r)\ \forall r \quad , \tag{2.56}$$

the corresponding radial state $R_{nl}(r)$ decays exponentially with growing r, as long as $V(r)$ vanishes at $r \to \infty$, whereas for free continuum states with

$$E_{nl} > V(r)\ \forall r \quad , \tag{2.57}$$

the absolute value $|R_{nl}(r)|$ approaches a constant value asymptotically with large values of r. This means that for continuum states, the confinement to $[0, r_{\text{max}}]$ would in general lead to a discontinuity at r_{max}, which obviously is an unphysical solution. As pointed out in [21], this can be overcome by artificially applying the additional boundary condition

$$R_{nl}(r_{\text{max}}) = 0 \quad , \tag{2.58}$$

which means that only B splines for which $B_i(x = r_{\text{max}}) = 0$ can be included in the basis. This boundary condition leads to a quantization of the energies of the continuum states, which is also discussed in [21]. For growing box sizes r_{max}, this discretization becomes denser.

The box size r_{max}, the number of B splines N, their degree k, and the first nonzero value Δr are parameters of the B spline basis, and in principle these parameters all have to be checked for convergence when calculating physical observables. In case the spherical symmetry of the system is broken, (for example by an external electric field), states with different l and m are coupled, such that the maximum l_{max} contained in the basis set (see eq. (2.46)) is another parameter that must be checked for convergence.

In this work, a B spline electronic structure calculation is done for the model potential approach presented in section 3.2. To this end, an existent code from the AMO group at Humboldt-Universität zu Berlin, which is a modified version [22] of a code from the group of P. Lambropoulos [23], was modified by the author to support the model potential used in section 3.2.

2.2 Charged Particles in Electromagnetic Fields

The interaction of a quantum mechanical system of charged particles with an external classical (i.e. non-quantized) electromagnetic field is discussed in the following. To keep the notation simple, only a single particle of mass $m = 1$ and charge q is considered. The generalization to a many-particle system like a molecule is however straightforward.

2.2.1 Minimal Coupling

Consider a single particle of charge q and mass $m = 1$ moving in the external potential $V(\vec{r})$. It is described by its state $|\psi(t)\rangle$ determined by the time-dependent Schrödinger equation (TDSE)

$$\hat{\mathrm{H}}_0 \, |\psi(t)\rangle = i\partial_t \, |\psi(t)\rangle \tag{2.59}$$

with the field-free Hamiltonian

$$\hat{\mathrm{H}}_0 = \frac{\hat{\mathrm{p}}^2}{2} + V(\hat{\vec{\mathrm{r}}}) \quad . \tag{2.60}$$

In order to provide gauge invariance of the Schrödinger equation, the coupling of the particle to an external electric field described by its vector potential $\vec{A}(\vec{r}, t)$ and its scalar potential $\Phi(\vec{r}, t)$ is described by modifying its momentum operator according to

$$\hat{\vec{\mathrm{p}}} \to \hat{\vec{\mathrm{p}}} - q\vec{A}(\hat{\vec{\mathrm{r}}}, t) \tag{2.61}$$

and updating the time derivative according to

$$i\partial_t \to i\partial_t - q\Phi(\hat{\vec{\mathrm{r}}}, t) \quad . \tag{2.62}$$

This can be reformulated as a new TDSE

$$\hat{\mathrm{H}}(t) \, |\psi(t)\rangle = i\partial_t \, |\psi(t)\rangle \tag{2.63}$$

using the now time-dependent Hamiltonian

$$\hat{\mathrm{H}}(t) = \hat{\mathrm{H}}_0 + \frac{1}{2}\left(q^2 A^2(\hat{\vec{\mathrm{r}}}, t) - q\left(\hat{\vec{\mathrm{p}}}\vec{A}(\hat{\vec{\mathrm{r}}}, t) + \vec{A}(\hat{\vec{\mathrm{r}}}, t)\hat{\vec{\mathrm{p}}}\right)\right) + q\Phi(\hat{\vec{\mathrm{r}}}, t) \quad . \tag{2.64}$$

2.2.2 Dipole Approximation

In dipole approximation, it is assumed that the spatial expansion of the state $|\psi(t)\rangle$ is so small on the length scale on which the electric field changes significantly for fixed t that the electric field the state $|\psi(t)\rangle$ is exposed to is independent of the location $\vec{r}$ for all $\vec{r}$ the state $|\psi(t)\rangle$ spans. Formally, for the electric field $\vec{F}(\vec{r}, t)$, this means that

$$\vec{F}(\vec{r}, t) = \vec{F}(t) \quad , \tag{2.65}$$

and similarly,

$$\vec{A}(\vec{r}, t) = \vec{A}(t) \tag{2.66}$$

for the vector potential. It follows that

$$\Phi(\vec{r}, t) = -\left(\vec{F}(t) + \frac{\partial \vec{A}(t)}{\partial t}\right)\vec{r} \tag{2.67}$$

up to the gauge freedom.

Dipole approximation means that the interaction of the quantum mechanical system with the external electromagnetic field is considered to lowest multipole order. To lowest order, the electric field is homogeneous and the magnetic field vanishes. In case the electromagnetic field is created by a laser, its length scale is determined by the laser's wavelength λ. For optical or infrared wavelengths from 400 nm, this scale is much larger than the typical size of a few-atom molecule, e.g. the 0.7 nm diameter of the C_{60} fullerene, which means that the electric field can be assumed to be homogeneous in the vicinity of the molecule at any instant of time. It is however noticeable that the dipole approximation not only breaks down in the short wavelength limit where the wavelength becomes comparable to the target size (which might be intuitive), but also for very long wavelengths and very large intensities, as pointed out in [24]. This is due to the fact that the dipole approximation assumes the magnetic field $\vec{B}(\vec{r},t)$ to be zero, as

$$\vec{B}(\vec{r},t) = \vec{\nabla} \times \vec{A}(t) = \vec{0} \quad , \tag{2.68}$$

and therefore neglects effects of the magnetic field. This is justified as long as the typical velocity v of the particle the field is interacting with is small compared to the speed of light, an assumption that breaks down for long wavelengths and large intensities.

2.2.3 Gauge Invariance

The time-dependent Schrödinger equation corresponding to the Hamiltonian in minimal coupling (eq. (2.64)) is formulated with respect to the scalar potential $\Phi(\vec{r},t)$ and the vector potential $\vec{A}(\vec{r},t)$. However, as those quantities can not be observed, but only the magnetic and electric field can, the TDSE in minimal coupling underlies the gauge invariance like every other law of electrodynamics, meaning that its predictions must be invariant under the transformations

$$\vec{A}(\vec{r},t) \to \vec{A}(\vec{r},t) + \vec{\nabla}_{\vec{r}} f(\vec{r},t) \tag{2.69}$$

$$\Phi(\vec{r},t) \to \Phi(\vec{r},t) - \partial_t f(\vec{r},t) \quad , \tag{2.70}$$

where $f(\vec{r},t)$ is an arbitrary function. Per construction, the choice of the gauge function $f(\vec{r},t)$ does not affect the results of any measurable prediction, as long as the exact calculation is done. However, as approximate descriptions of quantum mechanics like the strong-field approximation discussed in section 2.1.2 are not gauge-invariant in general, different gauges may lead to different results.

2.2.3.1 Radiation Gauge

The radiation gauge is a useful choice for systems without source, such as the electromagnetic field produced by a laser that is far away. In the radiation gauge, the vector potential and the scalar potential fulfill the relations

$$\vec{\nabla} \cdot \vec{A}_R(\vec{r},t) = 0 \quad , \quad \Phi_R(\vec{r},t) = 0 \quad . \tag{2.71}$$

A gauge function $f_{Q\to R}(\vec{r},t)$ that transforms the potentials in any gauge denoted by Q into radiation gauge R can always be found, as long as there are no sources present. From

$$0 \overset{!}{=} \Phi_R(\vec{r},t) = \Phi_Q(\vec{r},t) - \partial_t f_{Q\to R}(\vec{r},t) \quad , \tag{2.72}$$

it follows as one possible solution that

$$f_{Q\to R}(\vec{r},t) = \int^t \mathrm{d}t' \; \Phi_Q(\vec{r},t') \quad , \tag{2.73}$$

and this can be inserted into

$$0 \overset{!}{=} \vec{\nabla}\vec{A}_R(\vec{r},t) = \vec{\nabla}\left(\vec{A}_Q + \vec{\nabla}\int^t \mathrm{d}t' \; \Phi_Q(\vec{r},t')\right) \quad . \tag{2.74}$$

For the potentials in arbitrary gauge, it follows directly from the Maxwell equations that

$$\nabla^2\Phi_Q(\vec{r},t) = -4\pi\rho(\vec{r},t) - \partial_t(\vec{\nabla}\vec{A}_Q(\vec{r},t)) \quad , \tag{2.75}$$

where the charge density $\rho(\vec{r},t) \equiv 0$ for source-free fields. Insertion of eq. (2.75) into eq. (2.74) shows that the choice for $f_{Q\to R}(\vec{r},t)$ fulfills eq. (2.74) too.

In strong-field physics, there are 2 types of gauges mainly used in conjunction with the dipole approximation, namely velocity gauge and length gauge. As pointed out in detail in [21], radiation, velocity, and length gauge can be seen as particular cases of a family of gauges denoted as X gauge.

2.2.3.2 X Gauge

For simplicity, $q = -1$ is assumed as the particle's charge in the following. X gauge is the family of gauges denoted by the 2 parameters $X = (x_1, x_2)$ that can be obtained from radiation gauge using the gauge functions

$$f_{R\to X}(\vec{r},t) = -\left(x_1\vec{A}_R(\vec{r},t)\vec{r} + \frac{x_2}{2}\int^t \mathrm{d}t' \; \vec{A}_R^2(\vec{r},t')\right) \quad . \tag{2.76}$$

Using **dipole approximation**, $\vec{A}(\vec{r},t) = \vec{A}(t)$ can be assumed. The transformed potentials then read

$$\vec{A}_X(t) = \vec{A}_R(t)(1-x_1) \tag{2.77}$$

$$\vec{\Phi}_X(\vec{r},t) = -x_1\vec{F}(t)\hat{\vec{\mathrm{r}}} + x_2\frac{\vec{A}_R^2(t)}{2} \quad , \tag{2.78}$$

where it was used that $\vec{F}(t) = -\partial_t \vec{A}_R(t)$, as $\vec{\Phi}_R(\vec{r},t) \equiv 0$. The corresponding Hamiltonian in X gauge and dipole approximation reads

$$\begin{aligned}\hat{\mathrm{H}}^{(X)}(t) &= \hat{\mathrm{H}}_0 + \frac{1}{2}\left(\left((1-x_1)^2 - x_2\right) A_R^2(t) + (1-x_1)\left(\hat{\vec{\mathrm{p}}}\vec{A}_R(t) + \vec{A}_R(t)\hat{\vec{\mathrm{p}}}\right)\right) \\ &\quad + x_1 \vec{F}(t)\vec{r} \qquad (2.79)\\ &= \hat{\mathrm{H}}_0 + \left((1-x_1)^2 - x_2\right)\frac{A_R^2(t)}{2} + (1-x_1)\vec{A}_R(t)\hat{\vec{\mathrm{p}}} + x_1\vec{F}(t)\vec{r} \quad . \qquad (2.80)\end{aligned}$$

Radiation gauge, velocity gauge and length gauge are special cases of this family of gauges. They correspond to $X = (0,0)$ (no transformation), $X = (0,1)$, and $X = (1,0)$ respectively.

2.2.3.3 Velocity Gauge

Velocity gauge is X gauge with $X = (0,1)$, therefore the time-dependent Hamiltonian of a particle of charge -1 interacting with an external electromagnetic field reads

$$\hat{\mathrm{H}}^{(V)}(t) = \hat{\mathrm{H}}_0 + \vec{A}_R(t)\hat{\vec{\mathrm{p}}} \qquad (2.81)$$

in non-relativistic dipole approximation and velocity gauge.

2.2.3.4 Length Gauge

Length gauge is X gauge with $X = (1,0)$, hence the time-dependent Hamiltonian of a particle of charge -1 interacting with an external electromagnetic field reads

$$\hat{\mathrm{H}}^{(L)}(t) = \hat{\mathrm{H}}_0 + \vec{F}(t)\hat{\vec{\mathrm{r}}} \qquad (2.82)$$

in non-relativistic dipole approximation and length gauge. This allows for the interpretation of the external field as an additive time-dependent potential that tilts the potential included in $\hat{\mathrm{H}}_0$, depending on the field strength (see also fig. 2.2).

2.3 Description of Ionization Dynamics in Strong Fields

A typical application of a mathematical description of the interaction of a quantum mechanical system with a classical electromagnetic field is the calculation of (differential) ionization probabilities of the system after interacting with the electromagnetic field.

2.3.1 Subdivision into Ionization Regimes

A wave packet exposed to a sufficiently slowly varying electric field $\vec{F}(t)$ created by a laser is able to follow the field adiabatically, such that at each instant of time t_0, the wave packet is in the ground state of the corresponding Hamiltonian $\hat{\mathrm{H}}[F(t_0)]$. This type of interaction dynamics is called quasi-static. An electric field's variation is sufficiently slow if the time scale on which it oscillates is much longer than the characteristic time scale of the wave packet, which is given by the energy difference of the populated states. On the other hand, for rapidly varying fields, this is not true anymore, and the dominant ionization process is described as multiphoton ionization. The distinction between those two regimes has been introduced by Keldysh [25] for (dipole approximated) fields of the form

$$\vec{F}(t) = \vec{F}_0 \sin(\omega t) \quad . \tag{2.83}$$

There it was introduced what became known as the Keldysh adiabaticity parameter, meaning the ratio

$$\gamma_{\mathrm{Kel}} = \frac{\omega}{\omega_t} \quad , \tag{2.84}$$

where ω is the frequency of the laser field, and ω_t is the threshold frequency marking the boundary between the quasi-static regime and the multiphoton regime. For field frequencies well below this threshold, the wave packet can follow the perturbation adiabatically, while for much larger frequencies, it can not. Accordingly, $\gamma_{\mathrm{Kel}} \ll 1$ corresponds to quasi-static ionization dynamics, and $\gamma_{\mathrm{Kel}} \gg 1$ corresponds to the multiphoton regime. In [25], a semiclassical derivation is given for ω_t, based on the width of the potential barrier of an atomic system, which reads

$$\omega_t = \frac{F_0}{\sqrt{2I_P}} \quad , \tag{2.85}$$

where I_P is the ionization potential. The explicit form of the Keldysh parameter therefore reads

$$\gamma_{\mathrm{Kel}} = \omega \frac{\sqrt{2I_P}}{F_0} \quad . \tag{2.86}$$

Within the quasi-static regime, another qualitative differentiation of the ionization processes can be made naturally based on the field strength. In the length gauge picture (see eq. (2.82)) the effect of the electromagnetic field can be interpreted as an additional (time-dependent, but quasi-static) linear potential that tilts the Coulomb potential of the inter-particle interactions. If the field is strong enough, the electronic wave packet can leave the ion without tunneling through a classically forbidden barrier. This process is called quasi-static over-the-barrier ionization. On the other hand, if the field is weaker, the wave packet has to tunnel in order to escape from the ion, therefore ionization happens in the quasi-static tunneling regime. Fig. 2.2 shows a schematic representation of over-the-barrier and tunneling ionization in the quasi-static regime, and fig. 2.3 shows a summary of the ionization regimes for the case of hydrogen.

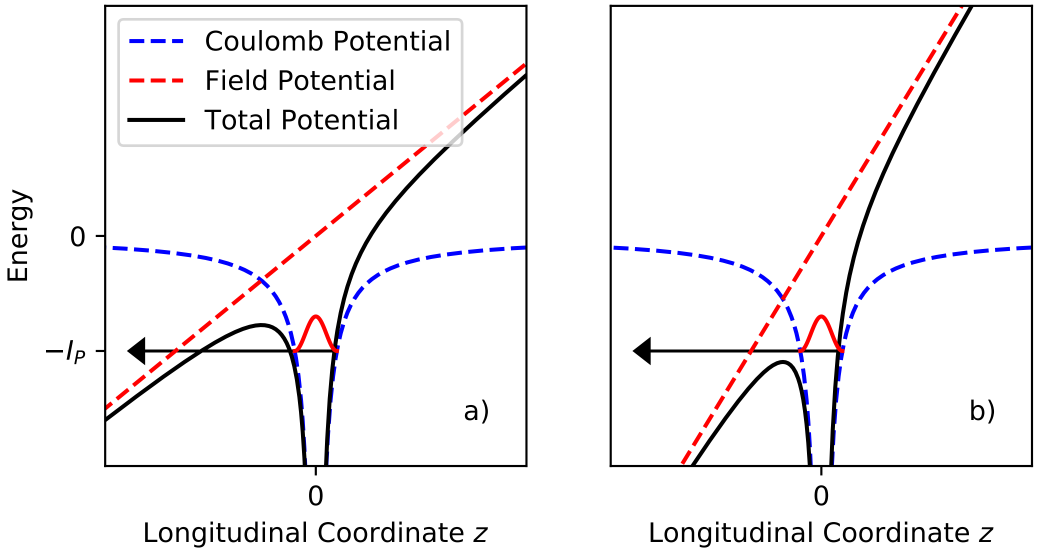

FIGURE 2.2: Schematic representation of (a) tunneling ionization and (b) over-the-barrier ionization within the quasi-static regime. In length gauge, the quasi-static field can be seen as an additional potential tilting the pure Coulomb potential. (a) For weaker field strengths, the field bends the potential, but the resulting barrier is higher than the energy of the wave packet $-I_P$, meaning that the wave packet can only escape via tunneling. (b) For stronger field strengths, the Coulomb potential is bent sufficiently such that the wave packet can ionize over the barrier.

2.3.2 Numerical Simulation

Consider a system of N particles with charge q moving in an external field. Its explicitly time-dependent Hamiltonian reads

$$\hat{\mathrm{H}}(t) = \hat{\mathrm{H}}_0 + \hat{\mathrm{H}}_I(t) \tag{2.87}$$

with the time-independent part $\hat{\mathrm{H}}_0$ and the interaction $\hat{\mathrm{H}}_I(t)$. Assuming that the interaction of the system with the field can be described in dipole approximation and length gauge is chosen, the interaction Hamiltonian reads

$$\hat{\mathrm{H}}_I(t) = -q\vec{F}(t)\sum_{i=1}^{N}\hat{\vec{\mathrm{r}}}_i \quad . \tag{2.88}$$

For the sake of simplicity, it is assumed in the following that $\vec{F}(t)$ is linearly polarized along $\vec{e}_z$, such that

$$\vec{F}(t) = F(t)\vec{e}_z \quad . \tag{2.89}$$

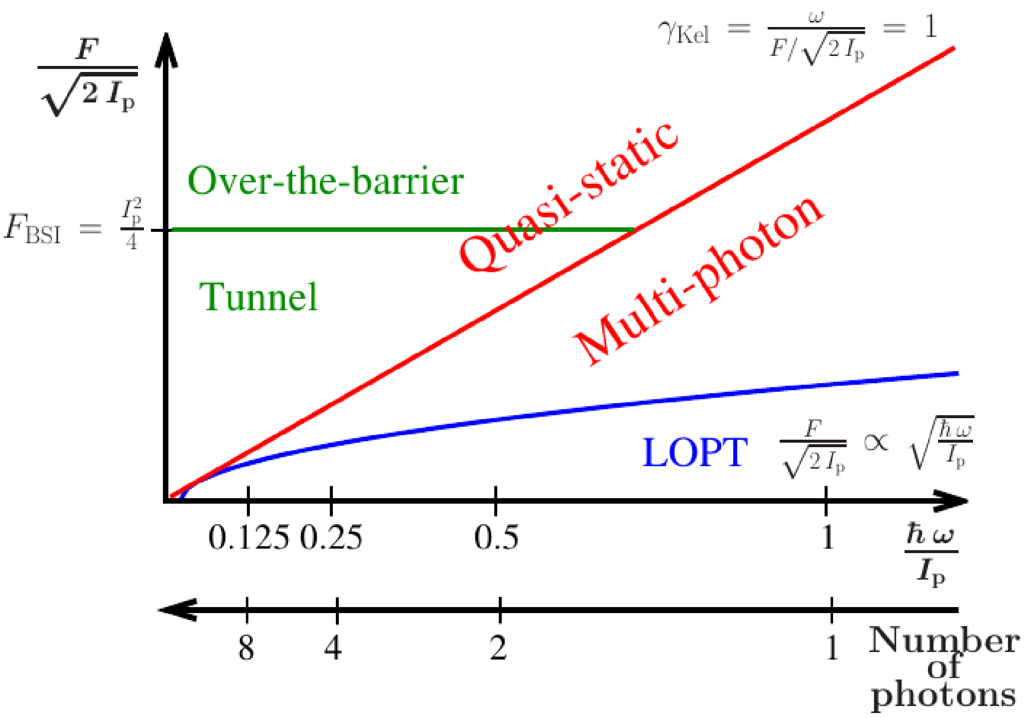

FIGURE 2.3: Subsection of the ionization processes based on the laser frequency F and field amplitude ω for the example of hydrogen. For $\gamma_{\text{Kel}} \ll 1$, the ionization dynamics are quasi-static, while $\gamma_{\text{Kel}} \gg 1$ corresponds to the multiphoton regime. Within the quasi-static regime, tunneling occurs for lower field strengths, and over-the-barrier ionization occurs for larger field strengths. Lowest order perturbation theory (LOPT) can be performed for sufficiently weak fields in case the frequency is not zero. Internal figure from the AMO group at Humboldt-Universität zu Berlin, created by Prof. Dr. A. Saenz.

Any discretized description of the TISE in a finite basis $\{|i\rangle\}$ can be used to find an approximation to the normalized eigenstates $|\psi_p\rangle$ of $\hat{\text{H}}_0$ with

$$\hat{\text{H}}_0 \, |\psi_p\rangle = E_p \, |\psi_p\rangle \quad . \tag{2.90}$$

As discussed in section 2.1.2, the states $|\psi_p\rangle$ are represented by a matrix of coefficient vectors according to

$$|\psi_p\rangle = \sum_i \mathbb{C}_{ip} \, |i\rangle \quad . \tag{2.91}$$

The matrix representation of $\hat{\text{H}}(t)$ can then be written in the finite basis set formed by the approximate eigenstates $|\psi_p\rangle$ (eigenbasis). Assuming that the basis states found within the finite-basis approximation are orthonormal, one has

$$\mathbb{H}^{(0)}_{pq} := \langle\psi_p|\hat{\mathrm{H}}_0|\psi_q\rangle \approx \delta_{pq}E_p \quad . \tag{2.92}$$

Notice that for any Hermitian operator, a basis set of orthonormal eigenstates can always be found. Similarly, one can define the transition dipole matrix

$$\mathbb{D}_{pq} := \left\langle \psi_p \middle| \sum_{i=1}^{N} \hat{\mathrm{z}}_i \middle| \psi_q \right\rangle \quad . \tag{2.93}$$

To calculate $\mathbb{D}_{pq}$, it is often less convenient to calculate the right side of eq. (2.93) directly, but it is often more convenient to calculate the transition dipole matrix in the original basis (see e.g. eq. (2.46) for the case of a B spline basis) first. This means that the matrix elements

$$\tilde{\mathbb{D}}_{ij} := \left\langle i \middle| \sum_{k=1}^{N} \hat{\mathrm{z}}_k \middle| j \right\rangle \tag{2.94}$$

are calculated before the matrix is transformed to the eigenbasis via matrix multiplication of the coefficient matrix

$$\mathbb{D}_{pq} = \sum_{ij} \mathbb{C}^*_{ip}\tilde{\mathbb{D}}_{ij}\mathbb{C}_{jq} \tag{2.95}$$

$$\Longleftrightarrow \quad \mathbb{D} = \mathbb{C}^\dagger\tilde{\mathbb{D}}\mathbb{C} \quad . \tag{2.96}$$

Using this, given any state $|\phi\rangle$ with a representation in the basis of eigenstates

$$|\phi\rangle = \sum_p a_p\,|\psi_p\rangle \quad , \tag{2.97}$$

the TDSE for this state can also be written in discretized form

$$i\partial_t\vec{a} = \mathbb{H}^{(0)}\vec{a} - qF(t)\mathbb{D}\vec{a} \quad , \tag{2.98}$$

where $(\vec{a})_p = a_p$. This is a coupled linear differential equation in N variables a_p. The shape of $\mathbb{H}^{(0)}$ is very simple: It is a diagonal matrix with the energies on the diagonal, so it induces no coupling between the a_p. Depending on the symmetry of the problem, $\mathbb{D}_{pq}$ can in many cases be separated into blocks of different symmetry, such that not all a_p are coupled with each other. For example, in the case of a single electron in a spherically symmetric potential, it has been discussed in section 2.1.2.1 that the eigenbasis can be chosen such that it takes the form

$$\langle r,\theta,\phi|\psi_p\rangle = \frac{R_{n_p,l_p}(r)}{r}Y_{l_p,m_p}(\theta,\phi) \quad . \tag{2.99}$$

Due to symmetry relations of the spherical harmonics, this results in selection rules of the form

$$\mathbb{D}_{pq} \propto \delta_{m_p,m_q} \left(C_1 \delta_{l_p,l_q+1} + C_2 \delta_{l_p,l_q-1} \right) \quad . \tag{2.100}$$

The described numerical solution of the finite basis set representation of the TDSE in the eigenbasis (eq. (2.98)) under consideration of the selection rules (eq. (2.100)) in this work is done with the `AMO_TOOLS`, in particular with the `TP_ATOM_1e` code [26]. As the eigenbasis $\{\psi_p\}$, this code uses the numerical B spline solution that was described in section 2.1.2. Hence, the eigenfunctions are represented as (see eq. (2.47))

$$\langle r, \theta, \phi | \psi_p \rangle = Y_{l_p,m_p} \sum_i \mathbb{C}_{pi} \frac{B_{\alpha_i}(r)}{r} \quad . \tag{2.101}$$

As different angular momentum quantum numbers l couple via the transition dipole moment (eq. (2.100)), results obtained from a numerical time propagation using a finite basis set not only have to be checked for convergence with respect to the set of B splines used for the spherical part, but also with respect to the l quantum numbers included. In this work, this is done by varying a parameter $l_{\max}$, where only $|\psi_p\rangle$ with $l_p \leq l_{\max}$ are included in the calculation.

2.3.3 Strong-Field Approximation (SFA)

Consider a charged particle of charge $q = -1$ and mass $m = m_e$ in an arbitrary potential $V(\vec{r})$, interacting with an electromagnetic field. Its TDSE reads

$$i\partial_t \left| \psi(t) \right\rangle = \hat{\mathrm{H}}^{(X)}(t) \left| \psi(t) \right\rangle \tag{2.102}$$

with the time-dependent Hamiltonian

$$\hat{\mathrm{H}}^{(X)}(t) = \hat{\mathrm{H}}_0 + \hat{\mathrm{H}}_I^{(X)}(t) \tag{2.103}$$

with

$$\hat{\mathrm{H}}_0 = \frac{\hat{\vec{\mathrm{p}}}^2}{2m_e} + V(\hat{\vec{\mathrm{r}}}) \quad , \tag{2.104}$$

where $\hat{\vec{\mathrm{p}}}$ is the quantum-mechanical momentum operator, and $\hat{\vec{\mathrm{r}}}$ is the position operator. $\hat{\mathrm{H}}_I^{(X)}(t)$ describes the time-dependent interaction of the electron with the external electromagnetic field in X gauge.

By formal integration of the TDSE (2.102), one can derive the state $|\psi(t)\rangle$ at any time t given a state $|\psi(t_0)\rangle$ at t_0:

$$\left| \psi^{(X)}(t) \right\rangle = \hat{\mathrm{U}}^{(X)}(t, t_0) \left| \psi(t_0) \right\rangle \tag{2.105}$$

with the unitary time-propagation operator

$$\hat{\mathrm{U}}^{(X)}(t,t_0) = \hat{\mathrm{T}}\exp\left(-i\int_{t_0}^{t}\hat{\mathrm{H}}^{(X)}(t')\mathrm{d}t'\right) \quad , \tag{2.106}$$

where $\hat{\mathrm{T}}$ is the time-ordering operator. One can then write the transition amplitude of the system at time t_f to a state $|\psi_f\rangle$ given that it starts in $|\psi_i\rangle$ at time t_i as

$$M_{i\to f}^{(X)} = \langle\psi_f|\hat{\mathrm{U}}^{(X)}(t_f,t_i)|\psi_i\rangle \quad . \tag{2.107}$$

This solution however is not feasible in practice, as the explicit form of $\hat{\mathrm{U}}(t,t_0)$ is usually not known.

The strong-field approximation [25, 27, 28] aims at solving this problem approximately by expanding $\hat{\mathrm{U}}(t,t_0)$ into a series that is truncated at some order, typically at linear order. To this end, a partitioning of the Hamiltonian

$$\hat{\mathrm{H}}^{(X)}(t) = \hat{\mathrm{H}}_1^{(X)}(t) + \hat{\mathrm{H}}_2^{(X)}(t) \tag{2.108}$$

is introduced. The corresponding time propagation operators are

$$\hat{\mathrm{U}}_1^{(X)}(t,t_0) = \hat{\mathrm{T}}\exp\left(-i\int_{t_0}^{t}\hat{\mathrm{H}}_1^{(X)}(t')\mathrm{d}t'\right) \tag{2.109}$$

and

$$\hat{\mathrm{U}}_2^{(X)}(t,t_0) = \hat{\mathrm{T}}\exp\left(-i\int_{t_0}^{t}\hat{\mathrm{H}}_2^{(X)}(t')\mathrm{d}t'\right) \quad . \tag{2.110}$$

$\hat{\mathrm{U}}^{(X)}(t,t_0)$ can be expressed with respect to $\hat{\mathrm{U}}_1^{(X)}(t,t_0)$ as

$$\hat{\mathrm{U}}^{(X)}(t,t_0) = \hat{\mathrm{U}}_1^{(X)}(t,t_0) - i\int_{t_0}^{t}\mathrm{d}t'\ \hat{\mathrm{U}}^{(X)}(t,t')\hat{\mathrm{H}}_2^{(X)}(t')\hat{\mathrm{U}}_1^{(X)}(t',t_0) \quad , \tag{2.111}$$

which is still a correct but implicit equation, as the sought after $\hat{\mathrm{U}}^{(X)}(t,t_0)$ appears on both sides.

The time propagation operator $\hat{\mathrm{U}}^{(X)}(t,t')$ on the right-hand side of this equation can be expressed using *another* partitioning of the total Hamiltonian $\hat{\mathrm{H}}^{(X)}(t)$ into

$$\hat{\mathrm{H}}^{(X)}(t) = \hat{\mathrm{H}}_{\mathrm{free}}^{(X)}(t) + V(\hat{\mathrm{r}}) \quad , \tag{2.112}$$

where

$$\hat{\mathrm{H}}_{\mathrm{free}}^{(X)}(t) = \frac{\hat{\mathrm{p}}^2}{2m_e} + \hat{\mathrm{H}}_I^{(X)}(t) \tag{2.113}$$

describes an unbound electron (without external potential) interacting with the external electromagnetic field. In complete analogy to eq. (2.111), the equation

$$\hat{\mathrm{U}}^{(X)}(t,t_0) = \hat{\mathrm{U}}^{(X)}_{\mathrm{free}}(t,t_0) - i\int_{t_0}^{t} \mathrm{d}t'\ \hat{\mathrm{U}}^{(X)}(t,t')V(\hat{\vec{\mathrm{r}}})\hat{\mathrm{U}}^{(X)}_{\mathrm{free}}(t',t_0) \tag{2.114}$$

can be derived from this second partitioning. Here, $\hat{\mathrm{U}}^{(X)}_{\mathrm{free}}(t,t_0)$ denotes the time propagation operator corresponding to $\hat{\mathrm{H}}^{(X)}_{\mathrm{free}}(t)$. Inserting eq. (2.114) into eq. (2.111) yields

$$\begin{aligned}\hat{\mathrm{U}}^{(X)}(t,t_0) = \hat{\mathrm{U}}^{(X)}_{1}(t,t_0) &- i\int_{t_0}^{t} \mathrm{d}t'\ \hat{\mathrm{U}}^{(X)}_{\mathrm{free}}(t,t')\hat{\mathrm{H}}^{(X)}_{2}(t')\hat{\mathrm{U}}^{(X)}_{1}(t',t_0) \\ &- \int_{t_0}^{t}\mathrm{d}t' \int_{t'}^{t}\mathrm{d}t''\ \hat{\mathrm{U}}^{(X)}(t,t'')V(\hat{\vec{\mathrm{r}}})\hat{\mathrm{U}}^{(X)}_{\mathrm{free}}(t'',t')\hat{\mathrm{H}}^{(X)}_{2}(t')\hat{\mathrm{U}}^{(X)}_{1}(t',t_0) \quad ,\end{aligned} \tag{2.115}$$

which is again an exact but implicit equation in $\hat{\mathrm{U}}^{(X)}(t,t_0)$.

In lowest order SFA, it is assumed that the field is strong enough to allow for the assumption that the shape of the potential $V(\vec{r})$ does not influence the ionization process significantly[1]. Formally, this means that the full time propagation $\hat{\mathrm{U}}^{(X)}(t,t_0)$ during ionization is dominated by the time propagation caused by $\hat{\mathrm{U}}^{(X)}_{\mathrm{free}}(t,t_0)$, such that the first-order expression

$$\hat{\mathrm{U}}^{(X)}(t,t_0) \approx \hat{\mathrm{U}}^{(X)}_{\mathrm{free}}(t,t_0) \tag{2.116}$$

can be inserted into the right-hand side of eq. (2.111), which yields

$$\hat{\mathrm{U}}^{(X)}(t,t_0) \approx \hat{\mathrm{U}}^{(X)}_{\mathrm{SFA}}(t,t_0) = \hat{\mathrm{U}}^{(X)}_{1}(t,t_0) - i\int_{t_0}^{t} \mathrm{d}t'\ \hat{\mathrm{U}}^{(X)}_{\mathrm{free}}(t,t')\hat{\mathrm{H}}^{(X)}_{2}(t')\hat{\mathrm{U}}^{(X)}_{1}(t',t_0) \quad . \tag{2.117}$$

This simplifies the calculation of $M^{(X)}_{i\to f}$, as typically one is interested in a plane-wave state as $|\psi_f\rangle$, and in this case, $\langle\psi_f|\,\hat{\mathrm{U}}^{(X)}_{\mathrm{free}}(t_f,t)$ is given by the Volkov states, as is discussed later in this chapter.

As already discussed in section 2.2.3, eq. (2.117) represents an approximation to the TDSE that, unlike the exact solution, can lead to different results depending on the chosen gauge. Furthermore, the results obviously depend on the partitioning

$$\hat{\mathrm{H}}^{(X)}(t) = \hat{\mathrm{H}}^{(X)}_{1}(t) + \hat{\mathrm{H}}^{(X)}_{2}(t) \tag{2.118}$$

that was chosen, as the expansion is truncated after a finite number of summands. Therefore, both the choice of gauge and the choice of partitioning influence the approximate observable prediction obtained in SFA. In fact, for the special case of the X gauge family, it has been shown in [21] that there

---

[1] Notice that, however, the state present before the onset of the interaction with the field of course typically depends on the potential, and so does its energy. This is not neglected in SFA.

exists a family of partitionings denoted by a set of parameters Λ such that the SFA result for every pair of X and Λ can be achieved with other combinations of X and Λ as well. This equivalence between choice of gauge and choice of partitioning in SFA is briefly discussed in the following.

2.3.3.1 Λ-Partitioning and X-Gauge

In [21], the family of partitionings

$$\hat{\mathrm{H}}^{(X)}(t) = \hat{\mathrm{H}}_1^{(X,\Lambda)}(t) + \hat{\mathrm{H}}_2^{(X,\Lambda)}(t) \quad , \tag{2.119}$$

is discussed, where

$$\hat{\mathrm{H}}_1^{(X,\Lambda)}(t) = e^{i\gamma_\Lambda(\hat{\vec{\mathrm{r}}},t)}\hat{\mathrm{H}}_0 e^{-i\gamma_\Lambda(\hat{\vec{\mathrm{r}}},t)} - \partial_t \gamma_\Lambda(\hat{\vec{\mathrm{r}}},t) \tag{2.120}$$

is a transformation of the field-free Hamiltonian $\hat{\mathrm{H}}_0$ using the function

$$\gamma_\Lambda(\vec{r},t) = \lambda_1 \vec{A}_R(t)\vec{r} + \frac{\lambda_2}{2}\int^t \mathrm{d}t' \ \vec{A}_R^2(t') \quad , \tag{2.121}$$

where $\Lambda = (\lambda_1, \lambda_2)$. In order to fulfill eq. (2.119), the interaction part reads

$$\begin{aligned}\hat{\mathrm{H}}_2^{(X,\Lambda)}(t) =& \frac{A_R^2(t)}{2}\big((1-x_1)^2 - \lambda_1^2 - (x_2-\lambda_2)\big) + (1-x_1+\lambda_1)\vec{A}_R(t)\hat{\vec{\mathrm{p}}} \\ &+ (x_1-\lambda_1)\,\vec{F}(t)\vec{r}\end{aligned} \tag{2.122}$$

in dipole approximation and X gauge. For example, by choosing $\Lambda = (0,0)$ and $X = (1,0)$ (length gauge), one obtains

$$\hat{\mathrm{H}}_2^{(X=L,\Lambda=(0,0))}(t) = \vec{F}(t)\hat{\vec{\mathrm{r}}} \quad , \tag{2.123}$$

as the interaction part of the untransformed field-free Hamiltonian $\hat{\mathrm{H}}_0$ in length gauge as written down in eq. (2.82). However, the same expression can be obtained for

$$\hat{\mathrm{H}}_2^{(X=L,\ \Lambda=(0,0))}(t) = \hat{\mathrm{H}}_2^{(X=V,\ \Lambda=(-1,1))}(t) = \hat{\mathrm{H}}_2^{(X=R,\ \Lambda=(-1,0))}(t) \quad . \tag{2.124}$$

This shows that the form of the interaction Hamiltonian $\hat{\mathrm{H}}_2^{(X,\Lambda)}(t)$ used in eq. (2.117) not only depends on the choice of gauge, but also on the choice of partitioning. Also in [21], it is shown that, if a plane wave

$$|\psi_f\rangle = |\vec{k}\rangle \tag{2.125}$$

is chosen as the final state, with

$$\langle\vec{r}|\vec{k}\rangle = \frac{1}{(2\pi)^{3/2}}e^{i\vec{k}\vec{r}} \quad , \tag{2.126}$$

the transition matrix element in SFA

$$M_{i\to f}^{\mathrm{SFA},(X,\Lambda)} = \langle\vec{k}|\hat{\mathrm{U}}_{\mathrm{SFA}}^{(X,\Lambda)}(t_f,t_i)|\psi_i\rangle \tag{2.127}$$

only depends on the differences $\lambda_1 - x_1$ and $\lambda_2 - x_2$, such that the same SFA result can be obtained for the transition amplitude for different gauges, as long as the partitioning is chosen accordingly. This shows that when comparing SFA approaches, it is important to not only compare the gauge choice, but also the partitioning choice.

2.3.3.2 $\Lambda = (0,0)$-Partitioning and Length Gauge

In the following, the SFA in $\Lambda = (0,0)$-partitioning and length gauge is discussed. As already mentioned, the partitioned Hamiltonians read

$$\hat{\mathrm{H}}_1^{(L,\Lambda=(0,0))}(t) = \hat{\mathrm{H}}_0 \tag{2.128}$$

$$\hat{\mathrm{H}}_2^{(L,\Lambda=(0,0))}(t) = \vec{F}(t)\hat{\vec{\mathrm{r}}} \quad , \tag{2.129}$$

such that the time propagation operator in SFA reads (leaving the indices for gauge and partitioning aside from now on)

$$\hat{\mathrm{U}}_{\mathrm{SFA}}(t,t_0) = \hat{\mathrm{U}}_0(t,t_0) - i\int_{t_0}^{t} \mathrm{d}t' \; \hat{\mathrm{U}}_{\mathrm{free}}(t,t')\vec{F}(t')\hat{\vec{\mathrm{r}}}\,\hat{\mathrm{U}}_0(t',t_0) \quad , \tag{2.130}$$

where $\hat{\mathrm{U}}_0(t',t_0)$ is the time propagation operator corresponding to the field-free Hamiltonian $\hat{\mathrm{H}}_0$. The resulting transition matrix element reads

$$M_{i\to f}^{\mathrm{SFA}} = \langle\psi_f|\hat{\mathrm{U}}_0(t_f,t_i)|\psi_i\rangle - i\int_{t_i}^{t_f} \mathrm{d}t' \; \langle\psi_f|\hat{\mathrm{U}}_{\mathrm{free}}(t_f,t')\vec{F}(t')\hat{\vec{\mathrm{r}}}\,\hat{\mathrm{U}}_0(t',t_i)|\psi_i\rangle \tag{2.131}$$

$$= \langle\psi_f|\psi_i^I(t_f)\rangle - i\int_{t_i}^{t_f} \mathrm{d}t' \; \langle\psi_f|\hat{\mathrm{U}}_{\mathrm{free}}(t_f,t')\vec{F}(t')\hat{\vec{\mathrm{r}}}\,|\psi_i^I(t')\rangle \quad , \tag{2.132}$$

where

$$|\psi_i^I(t)\rangle = \hat{\mathrm{U}}_0(t,t_i)\,|\psi_i\rangle \tag{2.133}$$

is the now time-dependent representation of $|\psi_i\rangle$ in the interaction picture, assuming that $|\psi_i^I(t=0)\rangle = |\psi_i\rangle$. The 0-th order term here is just the overlap of $|\psi_i^I(t_f)\rangle$ with $|\psi_f\rangle$, that also occurs if no field is present. As long as both states have no overlap, for example because they are different eigenstates of the same Hamiltonian, it is 0. The first order to contribute to ionization is

$$M_{\mathrm{ion}}^{\mathrm{SFA}} = -i\int_{t_i}^{t_f} \mathrm{d}t' \; \langle\psi_f|\hat{\mathrm{U}}_{\mathrm{free}}(t_f,t')\vec{F}(t')\hat{\vec{\mathrm{r}}}\,\hat{\mathrm{U}}_0(t',t_i)|\psi_i\rangle \tag{2.134}$$

$$M_{\mathrm{ion}}^{\mathrm{SFA}} = -i\int_{t_i}^{t_f} \mathrm{d}t' \; \langle\psi_f|\hat{\mathrm{U}}_{\mathrm{free}}(t_f,t')\vec{F}(t')\hat{\vec{\mathrm{r}}}\,|\psi_i^I(t')\rangle \quad . \tag{2.135}$$

2.3.3.2.1 Interpretation The first order expression in 2.134 can be interpreted as follows: The approximate ionization amplitude is the integral over all differential ionization amplitudes at times t'. This part of the amplitude describes an initially (at t_i) bound wave packet being propagated until t' using $\hat{\mathrm{U}}_0(t', t_i)\,|\psi_i\rangle$, i.e. textitneglecting the external field. Then, at t', the coupling to the ionized state "happens", with its strength being proportional to the transition dipole moment and the field at that time, i.e. to the matrix element with respect to the operator $\vec{F}(t')\hat{\vec{\mathrm{r}}}$. After the coupling at t', the wave packet is propagated from t' to t_f, using the time evolution operator $\hat{\mathrm{U}}_{\mathrm{free}}(t_f, t')$, which textitneglects the potential of the ion. That means that in this description, any influence of the external field on the ground state before the coupling happens is neglected, and any influence of the potential on the ionized state after the coupling is neglected as well.

An important consequence of the latter approximation is that the tunneling exponent resulting from the length gauge SFA in combination with the saddle point approximation (to be introduced in section 2.3.4) is blind to the exact shape of the binding potential, which can be seen e.g. when comparing to the WKB method, as done in section 5.2.1.2. On the other hand, an important consequence of the former approximation is that, regardless of the time t', the ground state does not deplete, as it is propagated with $\hat{\mathrm{H}}_0$ for infinitely long times. Saturation effects of the ionization are therefore neglected, which has to be accounted for when ionization yields come close to probability 1.

2.3.3.2.2 Final Volkov State If the plane-wave state

$$|\psi_f\rangle = |\vec{k}\rangle \tag{2.136}$$

is chosen as the final state, the explicit solution

$$|\psi_V(t)\rangle = \hat{\mathrm{U}}^{-1}_{\mathrm{free}}(t_f, t)\,|k\rangle \tag{2.137}$$

is known as the Volkov state [29] in length gauge. It reads

$$|\psi_V(t)\rangle = e^{-iS_{\vec{k}}(t)}\,|\vec{k} - \int_{t_f}^{t} \mathrm{d}t'\ \vec{F}(t')\rangle \quad , \tag{2.138}$$

with the time-dependent phase (action)

$$S_{\vec{k}}(t) = \frac{1}{2m_e}\int_{t_f}^{t} \mathrm{d}t' \left(\vec{k} - \int_{t_f}^{t'} \mathrm{d}t''\ \vec{F}(t'')\right)^2 \quad . \tag{2.139}$$

Using this, one obtains

$$M^{\mathrm{SFA}}_{\mathrm{ion}} = -i\int_{t_i}^{t_f} \mathrm{d}t'\ \langle\vec{k} - \int_{t_f}^{t'} \mathrm{d}t''\ \vec{F}(t'')|\vec{F}(t')\hat{\vec{\mathrm{r}}}|\psi_i^{(I)}(t')\rangle\, e^{iS_{\vec{k}}(t')} \tag{2.140}$$

for the ionization amplitude from $|\psi_i\rangle$ at t_i to $|\psi_f\rangle = |\vec{k}\rangle$ at t_f in SFA in length gauge and $\Lambda = (0, 0)$-partitioning.

2.3.4 Saddle Point Approximation

The SFA is often used in combination with the saddle point approximation (also known as method of steepest descent), which allows for the evaluation of the integral over t' in eq. (2.140) in an analytical form. It was first developed by Riemann in 1892 [30]. The saddle point approximation is applicable to integrals of the form

$$I = \int_{t_i}^{t_f} \mathrm{d}t' g(t') e^{f(t')} \quad . \tag{2.141}$$

The integrand $g(t)e^{f(t)}$ is a function of a real argument t, defined in a set $\mathbb{D}$. However, Cauchy's integral theorem can be applied if there exists an analytic continuation of the integrand to an open set $\mathbb{M}$ with $\mathbb{D} \subset \mathbb{M} \subseteq \mathbb{C}$, i.e. if there is an analytic (or holomorphic, which is equivalent) function defined in the open set $\mathbb{M}$ that is equal to the original integrand in $\mathbb{D}$. Let $\mathbb{M} \subseteq \mathbb{C}$ be an open set such that there exists an analytic continuation of $g(z)e^{f(z)}$ to $\mathbb{M}$ and let $\alpha, \beta : [0,1] \to \mathbb{M}$ be two homotopic curves in $\mathbb{M}$ with $\alpha(0) = \beta(0)$ and $\alpha(1) = \beta(1)$. Then

$$\int_\alpha g(z) e^{f(z)} \mathrm{d}z = \int_\beta g(z) e^{f(z)} \mathrm{d}z \quad . \tag{2.142}$$

According to the theorem, the complex path integral over a holomorphic function defined on an open set is the same for two different paths that are homotopic to each other, as long as they share the same starting and end points. Here, this can be used to replace the integral over the real axis from t_i to t_f with any homotopic path through the complex plane, as sketched in fig. 2.4. The idea of the saddle point approximation is to find a pathway that on its way through

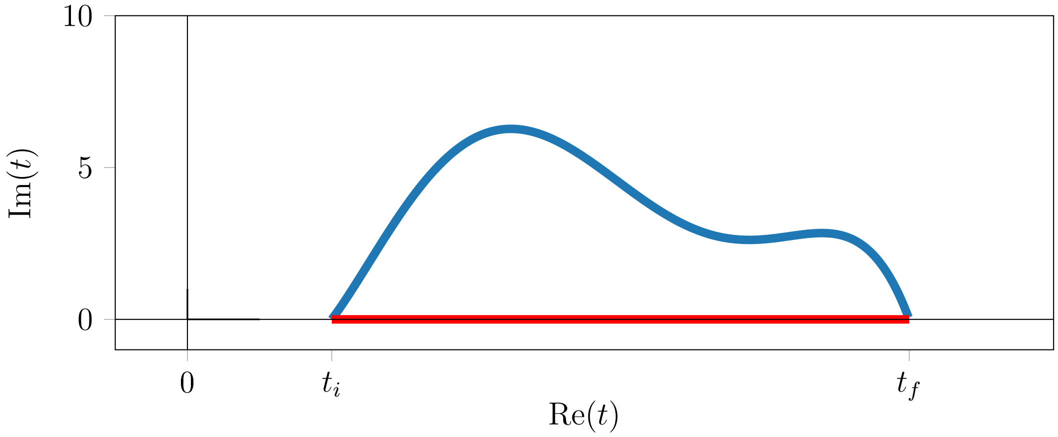

FIGURE 2.4: Application of Cauchy's integral theorem to an integrand of real argument. If there exists a holomorphic continuation of the function to an open set and if the blue path and the red path within the open set are homotopic to each other, the integral over each pathway is the same as long as they share the same starting and end points.

the complex plane from t_i to t_f crosses a sharply peaked maximum of the integrand. If this peak is sufficiently large, it dominates the value of the entire path integral. In this case, the value of the integral can be approximated by the integrand's value at the saddle point multiplied with the width of the peak. If furthermore the exponential part $e^{f(z)}$ of the integrand changes its value much faster in the vicinity of the peak than the prefactor $g(z)$ does, the position and the width of the peak of the entire integrand are given by the position and width of the peak of $e^{f(z)}$ alone.

If one finds a path from t_i to t_f that leads over such a single dominating peak (saddle point) at a complex "time" t_0, the integrand can be approximated as a Gaussian centered at t_0 with a width fitted to the integrand's curvature at t_0. In this case, the integral I from eq. (2.141) can be approximated as

$$I = \int_{t_i}^{t_f} \mathrm{d}t' g(t') e^{f(t')} \approx \sqrt{\frac{2\pi}{-\eta^2 \left.\frac{\mathrm{d}^2 f(t)}{\mathrm{d}t^2}\right|_{t=t_0}}} \eta g(t_0) e^{f(t_0)} \quad , \tag{2.143}$$

where η is a phase, i.e. $|\eta| = 1$, that has to be chosen such that $\eta^2 \left.\frac{\mathrm{d}^2 f(t)}{\mathrm{d}t^2}\right|_{t=t_0}$ is negative and real. The expression

$$g(t_0) e^{f(t_0)} \tag{2.144}$$

is the value of the integrand at the saddle point, the prefactor

$$\sqrt{\frac{2\pi}{-\eta^2 \left.\frac{\mathrm{d}^2 f(t)}{\mathrm{d}t^2}\right|_{t=t_0}}} \tag{2.145}$$

accounts for the width of the integrand's peak around the saddle point.

Because the integrand is holomorphic at the saddle point, its real and imaginary part $u, v : \mathbb{R}^2 \to \mathbb{R}$ with

$$g(z) e^{f(z)} = u(\mathrm{Re}(z), \mathrm{Im}(z)) + iv(\mathrm{Re}(z), \mathrm{Im}(z)) \tag{2.146}$$

fulfill the Cauchy-Riemann differential equations

$$\frac{\partial u}{\partial \,\mathrm{Re}(z)} = \frac{\partial v}{\partial \,\mathrm{Im}(z)} \quad , \quad \frac{\partial u}{\partial \,\mathrm{Im}(z)} = -\frac{\partial v}{\partial \,\mathrm{Re}(z)} \quad , \tag{2.147}$$

and therefore

$$\frac{\partial^2 u}{\partial (\mathrm{Re}(z))^2} = -\frac{\partial^2 u}{\partial (\mathrm{Im}(z))^2} \quad , \quad \frac{\partial^2 v}{\partial (\mathrm{Re}(z))^2} = -\frac{\partial^2 v}{\partial (\mathrm{Im}(z))^2} \quad . \tag{2.148}$$

From this, one can see that a holomorphic function never has a maximum in the complex plane, but only saddle points. If the second derivative in the one direction is negative, i.e. a maximum is reached, it is always positive in the orthogonal direction. Therefore, the path from t_i to t_f has to be chosen such that it crosses the saddle point in the direction of maximum negative curvature, i.e. it has to cross the saddle point like a car on a mountain pass crosses the lowest point of a mountain range which is the highest point in the trajectory of the car. If it doesn't, the path doesn't assume its maximum in t_0, but a local minimum, and the saddle point approximation is not applicable. In eq. (2.143), the phase factor η allows for controlling the direction of the crossing.

2.3.5 Example: Strong-Field Ionization of Hydrogen

An exemplary calculation for the removal of an electron originally bound in a scaled 1s-state of hydrogen is performed in the following, using both the SFA in length gauge and $\Lambda = (0, 0)$-partitioning and the saddle point approximation. This will allow for the examination of the relation between the spatial size of the ground state and the applicability of the saddle point approximation to the calculation of the SFA amplitude in length gauge and $\Lambda = (0, 0)$-partitioning. What can be learned from this is used in section 3.1, where a formalism is presented to overcome the difficulties shown in this section, which is then applied to the spatially larger ground state of C_{60}.

Between $t_i = 0$ and $t_f = \frac{\pi}{\omega}$, the system is exposed to a laser creating an electric field at the location of the atom (in the sense of the dipole approximation) with the time dependence

$$\vec{F}(t) = \begin{cases} 0 & t < t_i = 0 \\ \vec{e}_z F_0 \sin(\omega t) & 0 \leq t \leq \frac{\pi}{\omega} \\ 0 & t > t_f = \frac{\pi}{\omega} \end{cases} \quad . \tag{2.149}$$

This corresponds to a half-cycle pulse with a rectangular envelope (see the upper plot in fig. 2.5).

2.3.5.1 Ionization Amplitude in SFA

Initially, at t_i, the electron is in the 1s-state

$$\langle \vec{r} | \psi_i \rangle = \frac{1}{\sqrt{\pi} \alpha^{3/2}} e^{-r/\alpha} \tag{2.150}$$

with energy $E_0 = -0.5\,\text{a.u.}$ For hydrogen, $\alpha = 1\,\text{a.u.}$, however α is kept as a variable in this example. This will prove useful when investigating spatially larger ground states ($\alpha > 1$) or smaller ground states ($\alpha<1$); in particular the former case is interesting when calculating the ionization amplitude of C_{60} as done in chapter 3. The time-dependent state in interaction picture reads

$$\begin{aligned} |\psi_i^I(t)\rangle &= \hat{\mathrm{U}}^{(0)}(t, t_i)\, |\psi_i\rangle \qquad (2.151) \\ &= e^{-iE_0 t}\, |\psi_i\rangle \quad . \qquad (2.152) \end{aligned}$$

In order to evaluate the expression for the ionization amplitude in SFA $M_{\text{ion}}^{\text{SFA}}$ from eq. (2.140), the transition dipole moment

$$\langle \vec{k} | \hat{\mathrm{H}}_I(t) | \psi_i \rangle \tag{2.153}$$

is needed, which can be calculated analytically.

$$\langle\vec{k}|\hat{\mathrm{H}}_I(t)|\psi_i\rangle = \frac{F_0\sin(\omega t)}{\sqrt{\pi}\,(2\pi\alpha)^{3/2}}\int \mathrm{d}^3r\; e^{-i\vec{k}\vec{r}}ze^{-r/\alpha} \tag{2.154}$$

$$= i\frac{F_0\sin(\omega t)}{\sqrt{\pi}\,(2\pi\alpha)^{3/2}}\frac{\partial}{\partial k_z}\int \mathrm{d}^3r\; e^{-i\vec{k}\vec{r}}e^{-r/\alpha} \quad , \tag{2.155}$$

and after expanding the plane waves into

$$e^{-i\vec{k}\vec{r}} = 4\pi\sum_{l=0}^{\infty}\sum_{m=-l}^{l}(-i)^l j_l(kr)Y_{lm}(\hat{\vec{k}})Y^*_{lm}(\hat{\vec{r}}) \quad , \tag{2.156}$$

where $Y_{lm}(\theta,\phi)$ are the spherical harmonics and $j_l(x)$ are the spherical Bessel functions, one can write

$$\langle\vec{k}|\hat{\mathrm{H}}_I(t)|\psi_i\rangle = i\frac{\sqrt{2}}{\pi\alpha^{3/2}}F_0\sin(\omega t)\frac{\partial}{\partial k_z}\int_0^{\infty}\mathrm{d}r\; r^2 j_0(kr)e^{-r/\alpha} \quad . \tag{2.157}$$

Using

$$\int_0^{\infty}\mathrm{d}r\; r^2 j_0(kr)e^{-r/\alpha} = \frac{2\alpha^3}{(\alpha^2k^2+1)^2} \tag{2.158}$$

yields

$$\langle\vec{k}|\hat{\mathrm{H}}_I(t)|\psi_i\rangle = F_0\sin(\omega t)\frac{-8\sqrt{2}i\alpha^{7/2}}{\pi}\frac{k_z}{(\alpha^2k^2+1)^3} \quad . \tag{2.159}$$

Using eq. (2.152) and

$$\int_{t_f}^{t'}\mathrm{d}t''\;\vec{F}(t'') = \int_{\frac{\pi}{\omega}}^{t'}\mathrm{d}t''\;\vec{F}(t'') \tag{2.160}$$

$$= -\frac{F_0}{\omega}\left[1+\cos(\omega t')\right] \tag{2.161}$$

for $0 \leq t' \leq \frac{\pi}{\omega}$, one obtains

$$M_{\mathrm{ion}}^{\mathrm{SFA}} = -\frac{8\sqrt{2}F_0\alpha^{7/2}}{\pi}\int_{t_i}^{t_f}\mathrm{d}t'\;\frac{\sin(\omega t')\left(k_z+\frac{F_0}{\omega}\left[1+\cos(\omega t')\right]\right)e^{i\left(S_{\vec{k}}(t')-E_0t'\right)}}{\left(\alpha^2\left({k_\perp}^2+\left(k_z+\frac{F_0}{\omega}\left[1+\cos(\omega t')\right]\right)^2\right)+1\right)^3} \quad , \tag{2.162}$$

where $k_\perp^2 = k_x^2 + k_y^2$. The explicit form of $S_{\vec{k}}(t')$ can also be calculated analytically and reads

$$S_{\vec{k}}(t') = \left[\frac{1}{4}\left(2k_z^2 + 4k_z\frac{F_0}{\omega} + 3\left(\frac{F_0}{\omega}\right)^2\right)t'' \right. \tag{2.163}$$

$$\left. + \frac{8(k_z + \frac{F_0}{\omega})\frac{F_0}{\omega}\sin(\omega t'') + \left(\frac{F_0}{\omega}\right)^2\sin(2\omega t'')}{8\omega} + \frac{k_\perp^2}{2}t''\right]_{t''=\pi/\omega}^{t'} \tag{2.164}$$

for $t_f = \frac{\pi}{\omega}$.

2.3.5.2 Saddle Point Approximation

The integrand $g(t')e^{f(t')}$ with

$$g(t') = \sin(\omega t')\frac{k_z + \frac{F_0}{\omega}\left[1 + \cos(\omega t')\right]}{\left(\alpha^2\left({k_\perp}^2 + \left(k_z + \frac{F_0}{\omega}\left[1+\cos(\omega t')\right]\right)^2\right) + 1\right)^3} \tag{2.165}$$

$$f(t') = i\left(S_{\vec{k}}(t') - E_0 t'\right) \tag{2.166}$$

and its factors $g(t')$ and $e^{f(t')}$ alongside with the time-dependent field $F(t)$ are shown in fig. 2.5. For reasons that are discussed later on (see fig. 2.9), the laser parameters are chosen as

$$\omega = 0.01 \tag{2.167}$$

$$F_0 = 0.09 \quad , \tag{2.168}$$

the scale of the hydrogen 1s state is set to $\alpha = 0.3$, and for the final momentum, $k_z = -\frac{F_0}{\omega}$ and $k_\perp = 0$ are chosen. It is clearly visible that the integral over $g(t)e^{f(t)}$ approximately cancels out everywhere except for times t near the peak of the electric field at $t = \frac{1}{2}\frac{\pi}{\omega}$. For any time t, the derivative of the exponent is

$$\left|\frac{\mathrm{d}}{\mathrm{d}t}f(t)\right| = \frac{\mathrm{d}}{\mathrm{d}t}\left(S_{\vec{k}}(t) - E_0 t\right) \tag{2.169}$$

$$= \frac{1}{2m_e}\left(\vec{k} + \int_t^{t_f}\mathrm{d}t'\vec{F}(t')\right)^2 - E_0 \quad . \tag{2.170}$$

Consider a classical electron present in free space at time t. Due to its negative charge, it would gain the additional momentum

$$-\int_t^{t_f}\mathrm{d}t'\vec{F}(t') \tag{2.171}$$

in the field. If the electron arrives at a detector at time t_f with the momentum $\vec{k}$, its momentum at time t was

$$\vec{k} + \int_t^{t_f}\mathrm{d}t'\vec{F}(t') \quad . \tag{2.172}$$

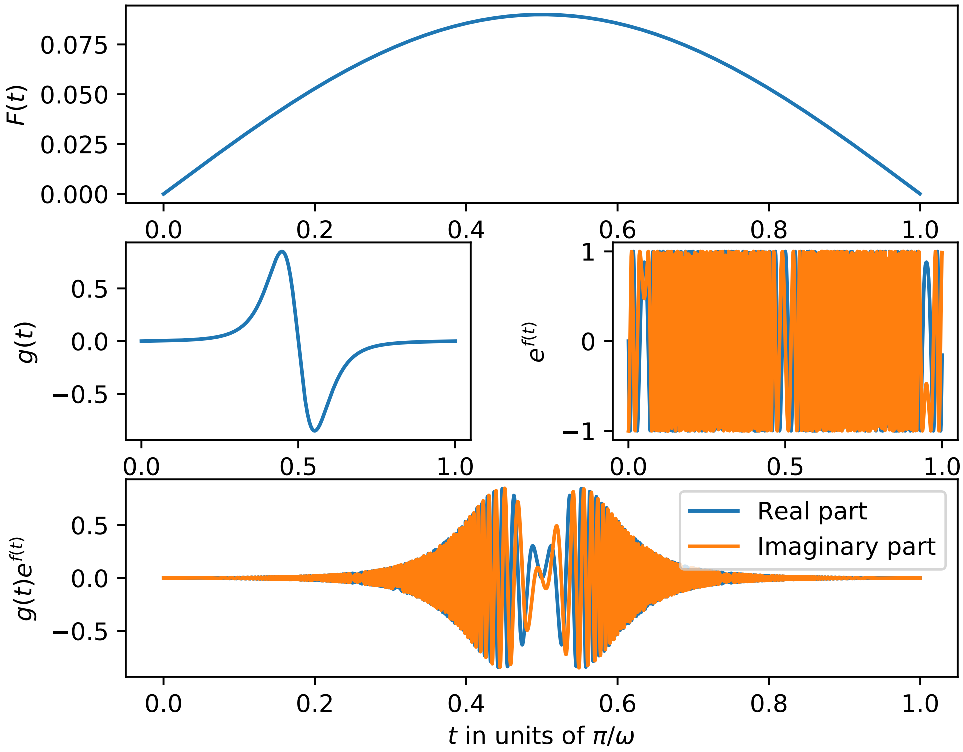

FIGURE 2.5: The real and imaginary parts of the SFA integrand $g(t)e^{f(t)}$ (at the bottom, see eqs. (2.165) and (2.166)) and its factors $g(t)$ and $e^{f(t)}$ (in the middle) are shown as a function of time, alongside with the time-dependent field $F(t)$ (at the top). The laser parameters are $F_0 = 0.09$ and $\omega = 0.01$, the scale of the ground state wave function is $\alpha = 0.3$, and for the final momentum, $k_z = -\frac{F_0}{\omega}$ and $k_\perp = 0$ are chosen.

Therefore, $\frac{\mathrm{d}}{\mathrm{d}t} S_{\vec{k}}(t)$ is the kinetic energy of a plane wave at time t, given that it was detected with momentum $\vec{k}$ at time t_f. Hence, $\frac{\mathrm{d}}{\mathrm{d}t}\left(S_{\vec{k}}(t) - E_0 t\right)$ is the ionization potential from the ground state into such a plane-wave state at time t. As already pointed out, the ionization amplitude $M_{\text{ion}}^{\text{SFA}}$, i.e. the integral over $g(t)e^{f(t)}$, is dominated by times t for which $e^{f(t)}$ oscillates slowly. On the other hand, the absolute value of the derivative of the imaginary exponent $f(t)$ is the smallest when $\frac{\mathrm{d}}{\mathrm{d}t} S_{\vec{k}}(t)$, i.e. the energy of the plane-wave state, is the smallest. One can conclude that the ionization amplitude into a plane-wave state that is measured at the detector with momentum $\vec{k}$ at t_f is predominantly determined by the minimum ionization potential that existed between the back-propagated state and the ground state during the pulse, i.e. the ionization potential at a time t_r.

This “almost stationary” point in time can be calculated as

$$\left| \frac{\mathrm{d}^2}{\mathrm{d}t^2} f(t) \bigg|_{t=t_r} \right| \overset{!}{=} 0 \iff \left(\vec{k} + \int_{t_r}^{t_f} \mathrm{d}t' \vec{F}(t') \right) \cdot \vec{F}(t_r) \qquad = 0 \quad , \tag{2.173}$$

which means that t_r, i.e. the dominant contribution to the total ionization, is the point in time at which the momentum component parallel to the field of the state later detected as $\vec{k}$ vanished. In the present example of a linearly polarized field in z direction (see eq. (2.149)), this yields the explicit expression

$$\cos(\omega t_r) = -1 - \frac{\omega k_z}{F_0} \quad . \tag{2.174}$$

Notice that $-\frac{2F_0}{\omega} \leq k_z \leq 0$, as the linearly polarized field always points in the positive z direction. For example, the integrand in fig. 2.5 is plotted for the final longitudinal momentum $k_z = -\frac{F_0}{\omega}$, corresponding to $t_r = \frac{1}{2}\frac{\pi}{\omega}$, which is exactly at the peak of the time-dependent field $F(t)$.

Because the exponent $f(t)$ itself is an oscillatory function in t with an amplitude proportional to F_0, the dominance of t_r is more pronounced if the field is stronger. This can also be understood intuitively. For stronger fields the wave packet is accelerated much more after ionization, and therefore a wave packet component being detected with momentum $\vec{k}$ that did not escape in the vicinity of t_r had to have a very strong longitudinal momentum after ionization, in order to make up for this acceleration. This large momentum adds to its ionization potential, which is reflected in a faster oscillation of $e^{f(t)}$ and hence in less contribution to the final amplitude.

So far, it has been established that for sufficiently strong fields the ionization amplitude $M_{\text{ion}}^{\text{SFA}}$ depends mainly on the slowly-varying part of the integrand $g(t)e^{f(t)}$ centered around t_r, assuming negligible oscillation of $g(t)$. Furthermore, the physical meaning of this was discussed. However, from this qualitative analysis it is not possible to calculate a numeric value for $M_{\text{ion}}^{\text{SFA}}$. Nevertheless, this can be done by analytically continuing the integrand to the complex plane and applying the saddle-point approximation according to eq. (2.143). Fig. (2.6) shows the absolute value of the complex integrand analytically continued to the complex plane. When moving from the real axis towards the positive imaginary direction, the integrand decreases exponentially. The faster the oscillation on the real axis is, the faster the integrand decreases. This leads to a very pronounced saddle in imaginary direction, centered at t_r. It is possible to find an integration path (gray dashed line in fig. 2.6) that crosses this saddle at its lowest point, i.e. at the saddle point. Notice that fig. 2.6 shows the SFA integrand for $k_z = -\frac{F_0}{\omega}$, which means that t_r is right at the maximum value of the field. Other k_z correspond to other t_r before or after the peak, which would result in a non-symmetric heat map.

2.3.5.3 Limit of slowly varying prefactor $g(t)$

In order for eq. (2.143) to hold, it is, as discussed, necessary that the prefactor $g(t)$ oscillates much more slowly than the exponential part $e^{f(t)}$ in the vicinity

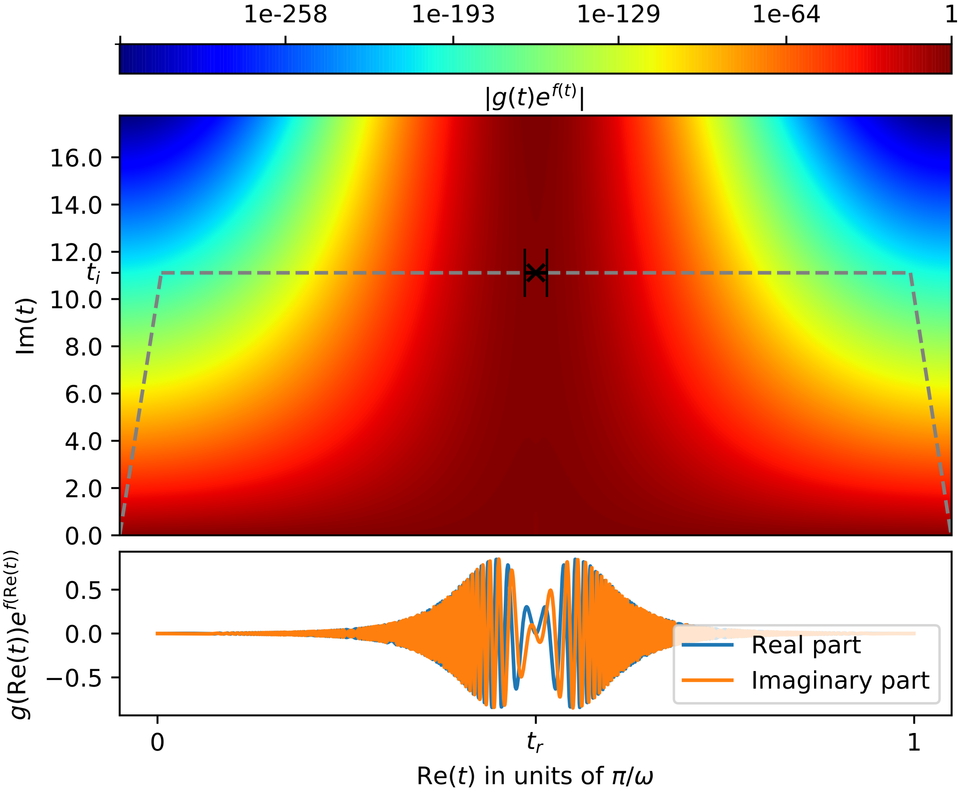

FIGURE 2.6: The absolute value of the SFA integrand $g(t)e^{f(t)}$ (see eqs. (2.165) and (2.166)) in the complex plane (upper plot) is shown together with its real and imaginary part on the real axis (lower plot). Where the oscillation along the real axis is slow, the exponential decay in the positive imaginary direction is comparatively slow. This leads to a pronounced saddle point at real time t_r and imaginary time t_i. When choosing the gray dashed integration path, the integral can be approximated using the value of the integrand at the saddle point and the width of the saddle point indicated by the black bar. The laser parameters are $F_0 = 0.09$ and $\omega = 0.01$, the scale of the ground state wave function is $\alpha = 0.3$, and for the final momentum, $k_z = -\frac{F_0}{\omega}$ and $k_\perp = 0$ are chosen.

of the saddle point t_0. A lower limit for the oscillation of $e^{f(t)}$ is given by $|E_0|$, as can be seen from eq. (2.170). It is however more complicated to quantify the oscillation frequency of $g(t)$ around t_0. As can be seen from Fig 2.7, the prefactor $g(t)$ has two peaks that are closer together the larger α becomes. The oscillation frequency in the vicinity of the saddle point, i.e. the frequency by which $g(t)$ changes from its maximum value to its minimum, can be defined in terms of the distance T_{half} between the maximum and the minimum,

$$\omega_g = \frac{2\pi}{2T_{\text{half}}}. \tag{2.175}$$

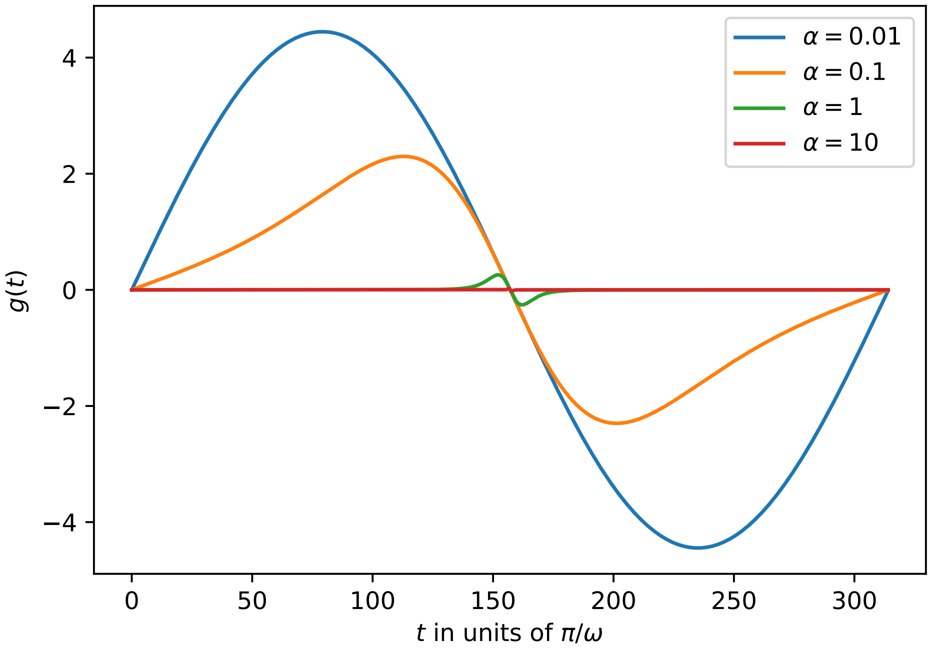

FIGURE 2.7: Dependency of the prefactor $g(t)$ (see eq. (2.165)) on the scale of the ground state α. The laser parameters are $F_0 = 0.09$ and $\omega = 0.01$, and for the final momentum, $k_z = -\frac{F_0}{\omega}$ and $k_\perp = 0$ are chosen.

The oscillation of the prefactor defined in this sense becomes faster the larger the ground state is. For very small α and for the choice of final momenta $k_z = -\frac{F_0}{\omega}$ and $k_\perp = 0$ like in fig. 2.7,

$$g(t) \approx \frac{F_0}{2\omega} \sin(2\omega t) \quad , \tag{2.176}$$

and therefore $\omega_g \approx 2\omega$. For larger α, the analytical expression for T_{half} can be obtained by calculating the distance between the maximum and the minimum explicitly, and for the special case $k_z = -\frac{F_0}{\omega}$ and $k_\perp = 0$ it reads

$$T_{\text{half}} = \frac{1}{\omega} \left(\arccos(C) - \arccos(-C) \right) \quad , \tag{2.177}$$

where

$$C = -\frac{\sqrt{\frac{2\omega^2 - \omega\sqrt{\frac{25\alpha^4 F_0^4}{\omega^2} + 4\alpha^2 F_0^2 + 4\omega^2}}{\alpha^2 F_0^2} + 5}}{2\sqrt{2}} \quad . \tag{2.178}$$

This formula can be used for an estimate of the order of magnitude of ω_g. To conclude, eq. (2.143) holds if the oscillation frequency of the exponential, i.e.

$|E_0|$, is much larger than ω_g, i.e.

$$\frac{\hbar\omega_g}{|E_0|} \ll 1 \quad . \tag{2.179}$$

Fig. 2.8 shows the value of $\frac{\hbar\omega_g}{|E_0|}$ for different values of α, ω, and F_0. The present choice of $F_0 = 0.09$, $\omega = 0.01$, and $\alpha = 0.3$ fulfills the requirement in eq. (2.179).

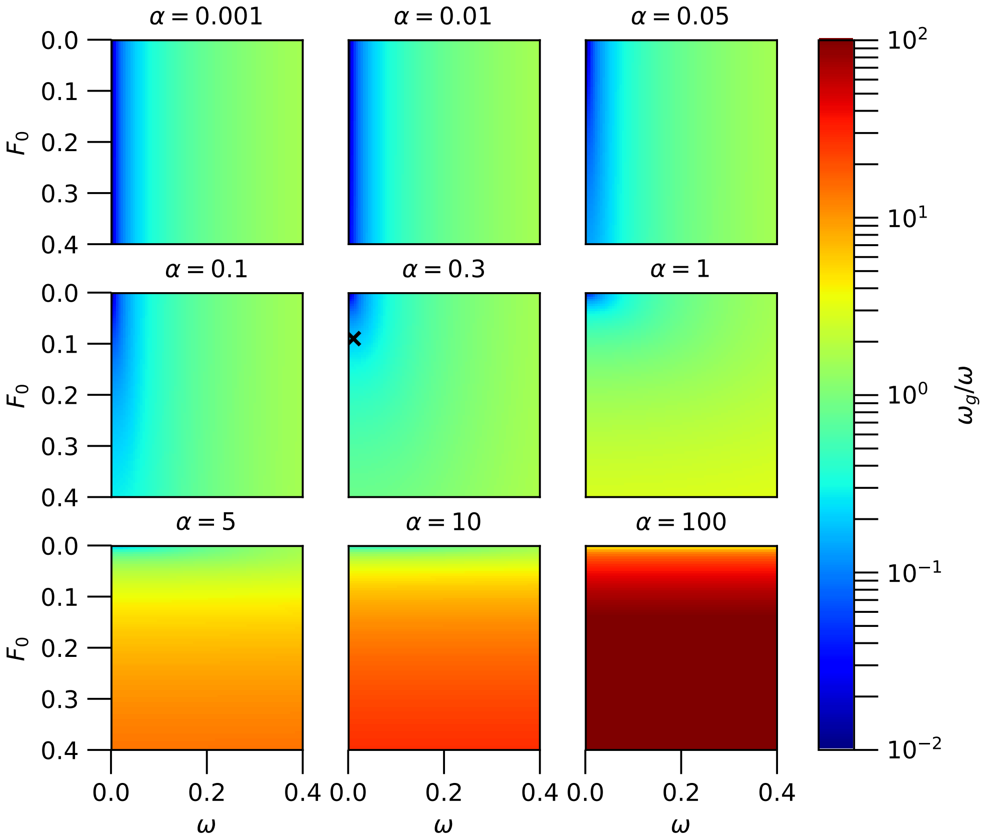

FIGURE 2.8: Parameter regime (shown for different ground state scales α as a function of the peak field strength F_0 and the frequency ω) in which the approximation of a slowly varying prefactor $g(t)$ (see eq. (2.165)) is fulfilled, i.e. $\frac{\hbar\omega_g}{|E_0|} \ll 1$. The numerical values are plotted for the final momenta $k_z = -\frac{F_0}{\omega}$ and $k_\perp = 0$, but also hold as an order-of-magnitude estimate for other momenta. For the present example, $F_0 = 0.09$, $\omega = 0.01$, and $\alpha = 0.3$ have been chosen, for which the approximation is fulfilled (black cross).

2.3.5.4 Quasi-static approximation

Because the prefactor $g(t)$ is slowly oscillating in the sense of eq. (2.179), the saddle point t_0 of the expression $g(t)e^{f(t)}$ can be approximately determined as the saddle point of the exponent $e^{f(t)}$ alone, i.e. at t_0 the *complex* derivative

$$\left.\frac{\mathrm{d}f(t)}{\mathrm{d}t}\right|_{t=t_0} = 0 \tag{2.180}$$

vanishes. This is fulfilled for

$$\frac{1}{2m_e}\left(\vec{k} + \int_{t_0}^{t_f} \mathrm{d}t' \vec{F}(t')\right)^2 - E_0 = 0 \quad , \tag{2.181}$$

where the integral symbol now denotes a complex path integral from t_0 to t_f, which is independent of the specific form of the path due to the analyticity of the function. It can be decomposed into

$$\int_{t_0}^{t_f} \mathrm{d}t' \vec{F}(t') = \int_{t_0}^{t_r} \mathrm{d}t' \vec{F}(t') + \int_{t_r}^{t_f} \mathrm{d}t' \vec{F}(t') \quad , \tag{2.182}$$

and, using eq. (2.173) and the fact that the field $\vec{F}(t)$ always points in z direction according to eq. (2.149), this can be rewritten as

$$\left(\int_{t_r}^{t_0} \mathrm{d}t' F(t')\right)^2 = -2m_e(-E_0 + \frac{k_\perp^2}{2m_e}) \quad . \tag{2.183}$$

Because E_0 is negative, the left part of the equation has to be purely imaginary. To solve for t_0, it is assumed that

$$\omega |t_0 - t_r| \ll 1 \quad , \tag{2.184}$$

which physically means that the Keldysh parameter for the ionization process is small, as is shown later. This approximation justifies the substitution $F(t') \approx F(t_r)$ in the integral, and one obtains

$$|t_0 - t_r| = \pm i \frac{\sqrt{2m_e I_P(k_\perp)}}{F(t_r)} \quad , \tag{2.185}$$

where $I_P(k_\perp)$ is the ionization potential from the ground state into a plane-wave state with the perpendicular momentum $k_\perp$ and vanishing longitudinal momentum $k_z = 0$.

$$I_P(k_\perp) = -E_0 + \frac{k_\perp^2}{2m_e} \quad . \tag{2.186}$$

In conclusion,

$$\omega |t_0 - t_r| = \omega \frac{\sqrt{2m_e I_P(k_\perp)}}{F(t_r)} = \gamma_{\mathrm{Kel}}(k_\perp) \ll 1 \tag{2.187}$$

is the Keldysh parameter of the described ionization process. Hence, the approximation $\omega|t_0 - t_r| \ll 1$ used to obtain this expression is fulfilled in the quasi-static limit in which $\gamma_{\mathrm{Kel}}(k_\perp) \ll 1$ (see section 2.3.1). Fig. 2.9 provides an overview of the possible combinations of α, ω, and F_0 for which both the approximation of a slowly varying prefactor (see eq. (2.179)) and the quasi-static approximation as defined in eq. (2.187) are fulfilled. As can be seen from the figure, the parameter choice $F_0 = 0.09$, $\omega = 0.01$, and $\alpha = 0.3$ lies within the regime in which both approximations are fulfilled, in fact, the values are

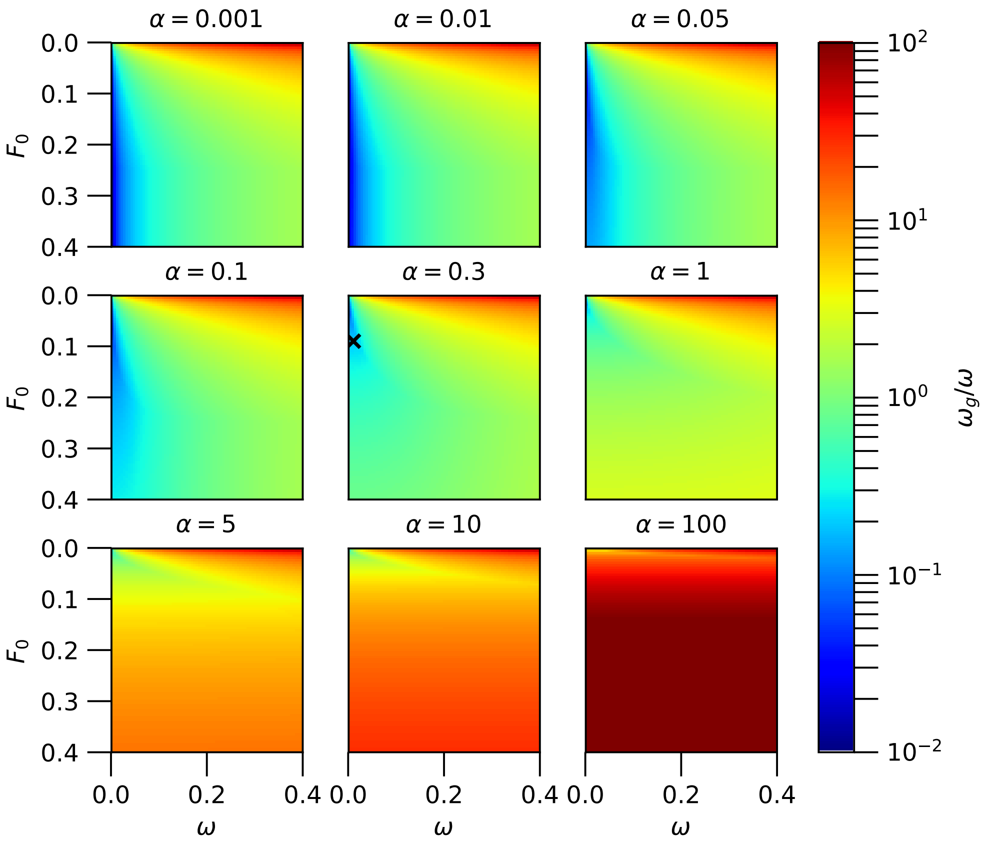

FIGURE 2.9: Parameter regime (shown for different ground state scales α as a function of the peak field strength F_0 and the frequency ω) in which both the approximation of a slowly varying prefactor $g(t)$ (see eq. (2.165)), i.e. $\frac{\hbar\omega_g}{|E_0|} \ll 1$, and the quasi-static approximation, i.e. $\gamma_{\text{Kel}}(k_\perp = 0) \ll 1$, are fulfilled. The numerical values are plotted for the final momenta $k_z = -\frac{F_0}{\omega}$ and $k_\perp = 0$, but also hold as an order-of-magnitude estimate for other momenta. For the present example, $F_0 = 0.09$, $\omega = 0.01$, and $\alpha = 0.3$ have been chosen, for which the approximations are fulfilled (black cross).

$$\frac{\hbar\omega_g}{|E_0|} = 0.11 \quad \text{and} \quad \gamma_{\text{Kel}}(k_\perp = 0) = 0.19 \quad . \tag{2.188}$$

When moving to larger ground state sizes α, e.g. to the real size of the hydrogen atom $\alpha = 1$, the approximations used require smaller frequencies ω, resulting in a rapidly oscillating integrand $g(t)e^{f(t)}$. Such an integrand is numerically demanding to evaluate when calculating the SFA amplitude (eq. (2.162)) directly without using the saddle point approximation. In section 2.3.5.5 however, the amplitude in SFA without the saddle point approximation is compared to the one with saddle point approximation, therefore values of ω that are not too small have to be used. Therefore, $\alpha = 1$ can not be used for the comparison.

The result for the saddle points in the quasi-static approximation is

$$\omega t_0 = \omega t_r \pm i\gamma_{\mathrm{Kel}}(k_\perp) \quad . \tag{2.189}$$

The result with positive sign is plotted as the black cross in fig. 2.6. Now the saddle point approximation formula in eq. (2.143) can be used. To stay consistent with the quasi-static approximation (see eq. (2.187)), $F(t_0)$ is expanded to linear order in $\omega|t_0 - t_r|$, i.e.

$$F(t_0) \approx F(t_r) \pm i \left.\frac{\mathrm{d}F(t)}{\mathrm{d}t}\right|_{t=t_r} \frac{\gamma_{\mathrm{Kel}}(k_\perp)}{\omega} \quad . \tag{2.190}$$

Because of

$$\max_t \left|\frac{\mathrm{d}F(t)}{\mathrm{d}t}\frac{\gamma_{\mathrm{Kel}}(k_\perp)}{\omega}\right| = F_0\gamma_{\mathrm{Kel}}(k_\perp) \ll F_0 \quad , \tag{2.191}$$

this first-order correction term is small in the quasi-static limit. In order to calculate the ionization matrix element defined in eq. (2.162), the saddle point approximation according to eq. (2.143) is applied, with $g(t')$ and $f(t')$ as defined in eqs. (2.165) and (2.166). $f(t_0)$ can be expressed as

$$\begin{aligned} f(t_0) &= i\left(S_{\vec{k}}(t_0) - E_0 t_0\right) && (2.192)\\ &= f(t_r) + i\left(\frac{1}{2m_e}\int_{t_r}^{t_0}\mathrm{d}t'\left(\vec{k} - \int_{t_f}^{t'}\mathrm{d}t''\vec{F}(t'')\right)^2 - E_0(t_0 - t_r)\right) && (2.193)\\ &= f(t_r) + i\left(\frac{1}{2m_e}\int_{t_r}^{t_0}\mathrm{d}t'\left(\int_{t_r}^{t'}\mathrm{d}t''\vec{F}(t'')\right)^2 + I_P(k_\perp)(t_0 - t_r)\right) \quad , && (2.194)\end{aligned}$$

and, using that $|t'' - t_r| \leq |t' - t_r| \leq |t_0 - t_r|$ in the integrand, the integrand can be approximated to leading order in $\omega|t'' - t_r|$, i.e.

$$\begin{aligned} f(t_0) &\approx f(t_r) + i\left(\frac{1}{2m_e}\int_{t_r}^{t_0}\mathrm{d}t' F^2(t_r)\,(t' - t_r)^2 + I_P(k_\perp)(t_0 - t_r)\right) && (2.195)\\ &= f(t_r) + i\left(\frac{1}{2m_e}\frac{F^2(t_r)}{3}(t_0 - t_r)^3 + I_P(k_\perp)(t_0 - t_r)\right) && (2.196)\\ &= f(t_r) \mp \frac{2}{3}\frac{\sqrt{2m_e}I_P^{3/2}(k_\perp)}{F(t_r)} \quad , && (2.197)\end{aligned}$$

where the negative sign corresponds to the positive sign in eq. (2.189) and vice versa. Because the final result for the ionization amplitude in saddle point approximation has the form

$$M_{\text{ion}}^{\text{SFA-SPA}} = -\frac{8\sqrt{2}F_0\alpha^{7/2}}{\pi}\sqrt{\frac{2\pi}{-\eta^2 \left.\frac{\mathrm{d}^2 f(t)}{\mathrm{d}t^2}\right|_{t=t_0}}}\eta g(t_0)e^{f(t_0)} \tag{2.198}$$

$$= -\frac{8\sqrt{2}F_0\alpha^{7/2}}{\pi}\sqrt{\frac{2\pi}{-\eta^2 \left.\frac{\mathrm{d}^2 f(t)}{\mathrm{d}t^2}\right|_{t=t_0}}}\eta g(t_0)e^{f(t_r)} \exp\left(\mp\frac{2}{3}\frac{\sqrt{2m_e}I_P^{3/2}(k_\perp)}{F(t_r)}\right) \quad , \tag{2.199}$$

one can now understand why the negative sign has to be chosen here, i.e., correspondingly, the positive sign in eq. (2.189). The inverse sign corresponds to a saddle point in the lower half of the complex plane. In the negative imaginary direction, the integrand $g(t)e^{f(t)}$ grows exponentially for all $\mathrm{Re}(t)$. This means that while it is correct to calculate the integral over t along a path in the lower half-plane, it is not possible to find a single saddle point that dominates the integral. However, as can be seen from fig. 2.6, the saddle point in the upper half-plane fulfills this requirement. Therefore, when using an integration path leading over the saddle point in the upper half-plane, the saddle point approximation can be applied.

Furthermore, one obtains

$$\left.\frac{\mathrm{d}^2 f(t)}{\mathrm{d}t^2}\right|_{t=t_0} = -\frac{i}{m_e}\left(\vec{k} - \int_{t_f}^{t_0}\mathrm{d}t'\ \vec{F}(t')\right)\vec{F}(t_0) \tag{2.200}$$

$$\approx -\frac{i}{m_e}\left(\vec{k} - \int_{t_f}^{t_0}\mathrm{d}t'\ \vec{F}(t')\right)\vec{F}(t_r) \tag{2.201}$$

$$= \frac{i}{m_e}\left(\int_{t_r}^{t_0}\mathrm{d}t'\ \vec{F}(t')\right)\vec{F}(t_r) \tag{2.202}$$

$$\approx -\frac{F^2(t_r)}{m_e}\frac{\gamma_{\text{Kel}}(k_\perp)}{\omega} \quad , \tag{2.203}$$

and because — as discussed in section 2.3.4 — the phase factor η has to be chosen such that

$$\mathrm{Re}\left(-\eta^2 \left.\frac{\mathrm{d}^2 f(t)}{\mathrm{d}t^2}\right|_{t=t_0}\right) > 0 \tag{2.204}$$

$$\mathrm{Im}\left(-\eta^2 \left.\frac{\mathrm{d}^2 f(t)}{\mathrm{d}t^2}\right|_{t=t_0}\right) = 0 \quad , \tag{2.205}$$

it follows that

$$\eta = 1 \quad , \tag{2.206}$$

meaning that the saddle point has to be crossed in positive real direction, as can also be seen from fig. 2.6. For the prefactor accounting for the width of the peak centered at the saddle point one obtains

$$\sqrt{\frac{2\pi}{-\eta^2 \left.\frac{\mathrm{d}^2 f(t)}{\mathrm{d}t^2}\right|_{t=t_0}}} = \frac{1}{|F(t_r)|}\sqrt{\frac{2\pi m_e \omega}{\gamma_{\mathrm{Kel}}(k_\perp)}} \quad . \tag{2.207}$$

The width of the saddle point is indicated by the black bar in fig. 2.6. As the analytical formula of $g(t)$ is known, $g(t_0)$ can be calculated without using the quasi-static approximation here.

The final result for the ionization amplitude in SFA and saddle point approximation reads

$$M_{\mathrm{ion}}^{\mathrm{SFA\text{-}SPA}} = -i\ e^{f(t_r)}\frac{8\sqrt{2}F_0\alpha^{7/2}}{\pi}\frac{1}{|F(t_r)|}\sqrt{\frac{2\pi m_e \omega}{\gamma_{\mathrm{Kel}}(k_\perp)}}g(t_0)\exp\left(-\frac{2}{3}\frac{\sqrt{2m_e}I_P^{3/2}(k_\perp)}{F(t_r)}\right) \quad . \tag{2.208}$$

Because $f(t_r)$ is a purely imaginary number, the term $e^{f(t_r)}$ is a phase describing the propagation of the free wave packet due to its own kinetic energy.

2.3.5.5 Validation of the Saddle Point Approximation

One can assess the applicability of the saddle point approximation in this specific case by comparing the analytical result in eq. (2.208) to the expression without saddle point approximation in eq. (2.162). While it is not feasible to calculate the time integral in the latter equation for a wide range of laser parameters and final momenta $\vec{k}$ numerically, it is easily possible to do so for a small set of parameters. The integration is done using the composite trapezoidal rule implemented in the `trapz` function contained in the `numpy` library [31] for `python`. Different step sizes are used to assess the convergence of the numerical integration. Fig. 2.10 compares the results for varying ω, while $F_0 = 0.09$ and $\alpha = 0.3$ are kept as in the examples before. The value $\omega = 0.01$, that was also used there, is indicated by the vertical black dashed line. As can be expected from fig. 2.9, the result for $M_{\mathrm{ion}}^{SFA-SPA}$ is the most accurate for lower values of ω, where the quasi-static approximation is better. In this regime, the deviation from M_{ion}^{SFA} is between 10% and 20%. The numerical evaluation of M_{ion}^{SFA} becomes demanding for the smallest ω shown here due to the fast oscillation of the integrand. This leads to numerical rounding errors, reflected by the fact that results for different step sizes don't agree anymore.

In this section, it was discussed using the example of hydrogen how and under which conditions the saddle point approximation can be applied to approximately calculate the SFA amplitude in length gauge and $\Lambda = (0, 0)$-partitioning. In particular, it has been shown that the assumption of a slowly varying transition dipole moment "prefactor" $g(t)$ only holds if the initial state is sufficiently compact, while its maximum size quantitatively depends on the laser parameters and the ionization potential of the state. This is of course a restriction that does not necessarily hold for all problems, specifically, it doesn't for the problem of the ionization of large molecules like C_{60} in typical laser fields, as can be seen from fig. 2.9 for large ground state sizes α. In the following chapter,

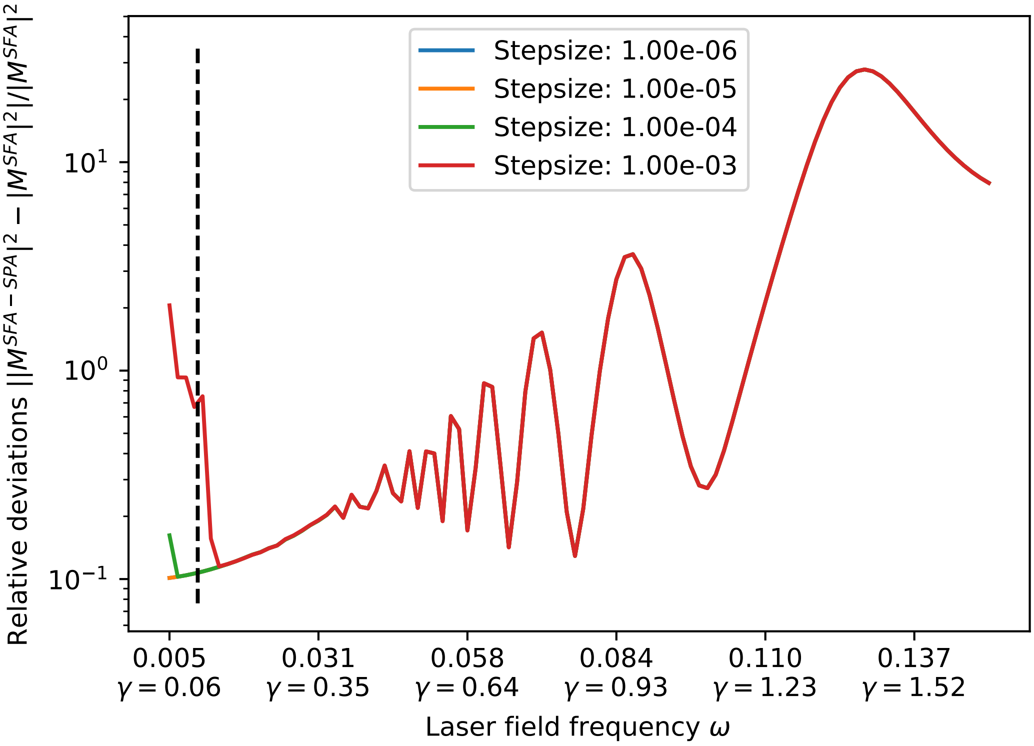

FIGURE 2.10: Relative deviations $\frac{\left||M_{\text{ion}}^{SFA-SPA}|^2 - |M_{\text{ion}}^{SFA}|^2\right|}{|M_{\text{ion}}^{SFA}|^2}$ of the differential ionization probabilities as a function of the frequency ω. The values of M_{ion}^{SFA} are obtained by integrating expression (2.162) numerically with different step sizes given in the legend. The values of $M_{\text{ion}}^{SFA-SPA}$ are obtained using the saddle point approximation according to eq. (2.208). The parameters $F_0 = 0.09$ and $\alpha = 0.3$ are kept as in the examples before, while the value $\omega = 0.01$, that was also used there, is indicated by the vertical black dashed line. Please refer to section 2.3.5.5 for a discussion of the results.

a new formalism is presented that circumvents this restriction, using a different splitting of the integrand into "slowly oscillating" and "rapidly oscillating" parts. This formalism is applied to the objective of this work, i.e. to the description of the ionization of the C_{60} fullerene in intense half-cycle pulses.

Chapter 3

Single Ionization of C_{60}

Consider a C_{60} molecule exposed to a time-dependent electric field in dipole approximation. As in the hydrogen example (see eq. (2.149)), the field is assumed to be of the form

$$\vec{F}(t) = \begin{cases} 0 & t < t_i = 0 \\ \vec{e}_z F_0 \sin(\omega t) & 0 \leq t \leq \frac{\pi}{\omega} \\ 0 & t > t_f = \frac{\pi}{\omega} \end{cases} \quad , \tag{3.1}$$

corresponding to a half-cycle pulse with a rectangular envelope. In this chapter, it is assumed that the removal of an electron originally bound in the C_{60} molecule can be described assuming only one single active electronic wave packet moving in the mean field created by the rest of the electronic distribution. This is known as the single-active-electron approximation (SAE) [32], and has been applied in various contexts before, e.g. to the ionization of molecular hydrogen [33, 34].

3.1 Analytical approach

As discussed in section 2.3.3, the saddle point approximation for the strong-field approximation in length gauge and $\Lambda = (0,0)$-partitioning breaks down for ground states that are large in the sense discussed there. As C_{60} has a radius of approximately $3.5\,\text{Å}$, this limit is already reached for relatively low field strengths, as is shown in this section. Based on the SFA in length gauge and $\Lambda = (0,0)$-partitioning (see eq. (2.140)), an extension of the saddle point approximation (SPA) is introduced to apply it to larger molecules, specifically to the C_{60} fullerene.

3.1.1 Approximate Ground-State of the Single Active Electron

For the analytical approach presented in the following, the ground state of the single active electron before being exposed to the laser field is described in the rigid-rotor approximation, i.e. it reads

$$|g\rangle = |l, u\rangle \quad , \tag{3.2}$$

where $|l, u\rangle$ was already defined in the introduction of the rigid-rotor model in section 2.1.1.2, more precisely in eq. (2.34).

3.1.2 Transition Matrix Element in Strong-Field Approximation

The strong-field approximation (SFA) in length gauge and $\Lambda = (0,0)$-partitioning introduced and discussed in section 2.3.3 can be directly applied to the transition of the single active electron originally found in $|g\rangle = |l,m\rangle$ into a free plane-wave state $|\vec{k}\rangle$. The implication of the SFA is, as already discussed, that the interaction of the removed electron with the atomic potential is neglected completely during the ionization process itself, such that the dynamics are solely determined by the interaction of the electron with the external ionizing field described by the interaction Hamiltonian

$$\hat{\mathrm{H}}_I(t) = \hat{\vec{\mathrm{r}}} \cdot \vec{F}(t) \quad . \tag{3.3}$$

The ionization amplitude from the initial state $|g\rangle$ the system is found in at t_i into the final state $|k\rangle$ at a time t_f in length gauge and $\Lambda = (0,0)$-partitioning reads (see eq. (2.140))

$$M_{\text{ion}}^{\text{SFA}} = -i \int_{t_i}^{t_f} \mathrm{d}t' \; \langle \vec{k} - \int_{t_f}^{t'} \mathrm{d}t'' \; \vec{F}(t'') | \vec{F}(t') \hat{\vec{\mathrm{r}}} \, |g^{(I)}(t')\rangle \, e^{iS_{\vec{k}}(t')} \quad , \tag{3.4}$$

where $|g^{(I)}(t)\rangle$ is the ground state $|g\rangle$ in the interaction picture, i.e.

$$\begin{aligned} |g^{(I)}(t)\rangle &= \hat{\mathrm{U}}^{(0)}(t,t_i)\,|g\rangle & (3.5) \\ &= e^{-iE_1 t}\,|g\rangle \quad , & (3.6) \end{aligned}$$

and the ground state energy of the single active electron is given by the first ionization energy of C_{60} that was found experimentally to be 7.65 eV [7], i.e.

$$E_1 = -7.65\,\mathrm{eV} \quad , \tag{3.7}$$

as well as

$$S_{\vec{k}}(t) = \frac{1}{2m_e} \int_{t_f}^{t} \mathrm{d}t' \left(\vec{k} - \int_{t_f}^{t'} \mathrm{d}t'' \; \vec{F}(t'') \right)^2 \quad . \tag{3.8}$$

3.1.3 Solution using the Saddle Point Approximation

Based on the SFA in length gauge and $\Lambda = (0,0)$-partitioning, an extension to the saddle point approximation is introduced in the following to use it for larger ground states, like for example the rigid-rotor ground state of the single active electron of the C_{60} fullerene.

Defining the transition dipole moment $D(\vec{k})$ according to

$$D(\vec{k}) := \langle \vec{k} | \hat{\mathrm{z}} | g \rangle \tag{3.9}$$

allows one to rewrite the ionization amplitude in SFA as

$$M_{\text{ion}}^{\text{SFA}} = -i \int_{t_i}^{t_f} \mathrm{d}t' \; F(t') D \left(\vec{k} - \int_{t_f}^{t'} \mathrm{d}t'' \; \vec{F}(t'') \right) e^{i\left(S_{\vec{k}}(t') - E_1 t'\right)} \quad . \tag{3.10}$$

On the first glance, the application of the saddle point approximation (SPA) might seem straightforward from here by simply defining

$$g(t) := F(t) D \left(\vec{k} - \int_{t_f}^{t} \mathrm{d}t' \; \vec{F}(t') \right) \tag{3.11}$$

$$f(t) := i \left(S_{\vec{k}}(t') - E_1 t' \right) \tag{3.12}$$

and then applying eq. (2.143), i.e.

$$\int_{t_i}^{t_f} \mathrm{d}t' g(t') e^{f(t')} \approx \sqrt{\frac{2\pi}{-\eta^2 \left. \frac{\mathrm{d}^2 f(t)}{\mathrm{d}t^2} \right|_{t=t_0}}} \eta g(t_0) e^{f(t_0)} \quad , \tag{3.13}$$

however, as discussed in section 2.3.4, this equation only holds if the “prefactor” $g(t)$ only oscillates slowly in the vicinity of the saddle point t_0. There, the exemplary application of SFA and SPA to the ionization of hydrogen was discussed, finding that the oscillation timescale of $g(t)$ depends on the spatial scale of the ground state, such that eq. (3.13) only holds for ground states that are spatially small enough in the sense that was established there (see eq. 2.179). As the C_{60} molecule is around seven times larger in diameter than the hydrogen atom, one can already expect that the assumption of a slowly varying prefactor $g(t)$ might not hold here anymore for the same laser parameters. Of course, this argument is more subtle, as it also depends on other scales of the system as the ionization potential $|E_1|$, and it is refined quantitatively later in this chapter. In the following, a new approach is presented that circumvents the difficulties arising from the fast oscillation of the prefactor $g(t)$ when defined according to eq. (3.11).

To this end, a different splitting is introduced in which the oscillating part of the prefactor is explicitly incorporated into the exponential part. Using

$$\langle \vec{r} | \vec{k} \rangle = \frac{1}{(2\pi)^{3/2}} e^{i\vec{k}\vec{r}} \quad , \tag{3.14}$$

one can explicitly express the transition dipole moment as integral over z

$$D(\vec{k}) = \int \mathrm{d}z \; d(z, \vec{k}_\perp) e^{-ik_z z} \quad , \tag{3.15}$$

and using that $\vec{F}(t) = \vec{e}_z F(t)$ and

$$\vec{k} - \int_{t_f}^{t} \mathrm{d}t' \; \vec{F}(t') = \vec{k}_\perp - \int_{t_r}^{t} \mathrm{d}t' \; \vec{F}(t') \quad , \tag{3.16}$$

where $\vec{k}_\perp$ is the momentum vector perpendicular to the field and

$$\cos(\omega t_r) = -1 - \frac{\omega k_z}{F_0} \quad , \tag{3.17}$$

one can write

$$\begin{aligned} M_{\text{ion}}^{\text{SFA}} = -i \int \mathrm{d}z \int_{t_i}^{t_f} \mathrm{d}t' \; F(t') d(z, \vec{k}_\perp) \\ \cdot \exp\left(i \left(S_{\vec{k}}(t') - E_1 t' + \int_{t_r}^{t'} \mathrm{d}t'' \; F(t'') z \right) \right) \quad . \end{aligned} \tag{3.18}$$

Looking at the inner integral, one can define

$$g(t,z) := F(t) d(z, \vec{k}_\perp) \tag{3.19}$$

$$f(t,z) := i \left(S_{\vec{k}}(t) - E_1 t + \int_{t_r}^{t} \mathrm{d}t' \; F(t') z \right) \quad . \tag{3.20}$$

The oscillation of the prefactor is simply the field frequency ω now, and the local oscillation frequency of $e^{f(t)}$ can be defined as

$$\left| \frac{\mathrm{d}f(t)}{\mathrm{d}t} \right| = \left| \frac{1}{2m_e} \left(\vec{k} - \int_{t_f}^{t} \mathrm{d}t' \; \vec{F}(t') \right)^2 - E_1 + F(t) z \right| \quad . \tag{3.21}$$

From this expression it becomes clear that around the saddle point t_0, the condition

$$|E_1| \gg F(t) z \tag{3.22}$$

has to be fulfilled if one would like to neglect the extra term $F(t)z$ coming from the prefactor. As $d(z, \vec{k}_\perp)$ is proportional to the x-y-integral over the ground state in position representation, the largest z occurring in the time integral are on the order of the scale of the ground state, i.e. r_0. In conclusion, the simple formula in eq. (3.13) can only be used if

$$\hbar\omega \ll |E_1| \tag{3.23}$$

$$F_0 r_0 \ll |E_1| \tag{3.24}$$

are both fulfilled. While $\hbar\omega \ll |E_1|$ is usually the case for laser parameters in the quasi-static ionization regime, in the case of C_{60}, $\frac{|E_1|}{r_0}$ corresponds to a maximum field intensity of ca. $6.3 \times 10^{13}\,\mathrm{W/cm^2}$. However, in the strong-field regime, typically lasers in the $1 \times 10^{13}\,\mathrm{W/cm^2}$ intensity regime are used, and therefore $F_0 r_0 \ll |E_1|$ is not fulfilled for the laser parameters of interest here.

The fact that it can not be assumed that $g(t)$ in eq. (3.11) is slowly varying but only $g(t,z)$ in eq. (3.19) is a complication that arises from the fact that C_{60} is a molecule that is much larger and has a much smaller ionization potential than most atoms, i.e. $\frac{|E_1|}{r_0}$ is much smaller than for typical atoms. Therefore the extension of the “traditional” saddle point approximation (as introduced in the hydrogen example in section 2.3.5) that is introduced now is typically applicable to larger molecules. To solve eq. (3.18), a possible approach is to apply the saddle point approximation to the inner integral over t' using

$$\int_{t_i}^{t_f} \mathrm{d}t' g(t', z) e^{f(t',z)} \approx \sqrt{\frac{2\pi}{-\eta^2 \left.\frac{\mathrm{d}^2 f(t,z)}{\mathrm{d}t^2}\right|_{t=t_0}}} \eta g(t_0, z) e^{f(t_0,z)} \quad . \tag{3.25}$$

As already stated, $g(t, z)$ has to be slowly varying compared to $e^{f(t,z)}$ for this approximate formula to be applicable. This is the case if

$$\hbar\omega \ll |E_1| \quad . \tag{3.26}$$

For the present system, $|E_1|$ corresponds to a laser wavelength of approx. 160 nm. The condition (3.26) therefore is comfortably met by laser wavelengths in the infrared spectrum, which are used throughout this work.

The saddle point t_0 of $e^{f(t)}$ fulfills the equation

$$\left.\frac{\mathrm{d}f(t)}{\mathrm{d}t}\right|_{t=t_0} = 0 \tag{3.27}$$

and, following the steps in section 2.3.5 analogously, one obtains

$$\left(\int_{t_r}^{t_0} \mathrm{d}t' F(t')\right)^2 = -2m_e \left(-E_1 + \frac{k_\perp^2}{2m_e} + F(t_0) z\right) \quad . \tag{3.28}$$

In the limit

$$\omega |t_0 - t_r| \ll 1 \quad , \tag{3.29}$$

one obtains

$$\omega(t_0 - t_r) = i\omega \frac{\sqrt{2m_e(I_P(k_\perp) + F(t_r)z)}}{F(t_r)} = i\gamma_{\mathrm{Kel}}(k_\perp, z) \tag{3.30}$$

with

$$I_P(k_\perp) = -E_1 + \frac{k_\perp^2}{2m_e} \quad , \tag{3.31}$$

which, again analogously to the hydrogen case, shows *a posteriori* that the precondition $\omega|t_0 - t_r| \ll 1$ is fulfilled in the quasi-static limit where

$$\gamma_{\mathrm{Kel}}(k_\perp, z) \ll 1 \quad . \tag{3.32}$$

In fig. 3.1, the applicability of the quasi-static approximation $\gamma_{\mathrm{Kel}}(k_\perp = 0, z = 0) \ll 1$ is shown for a variety of laser parameters. Analogously, one obtains

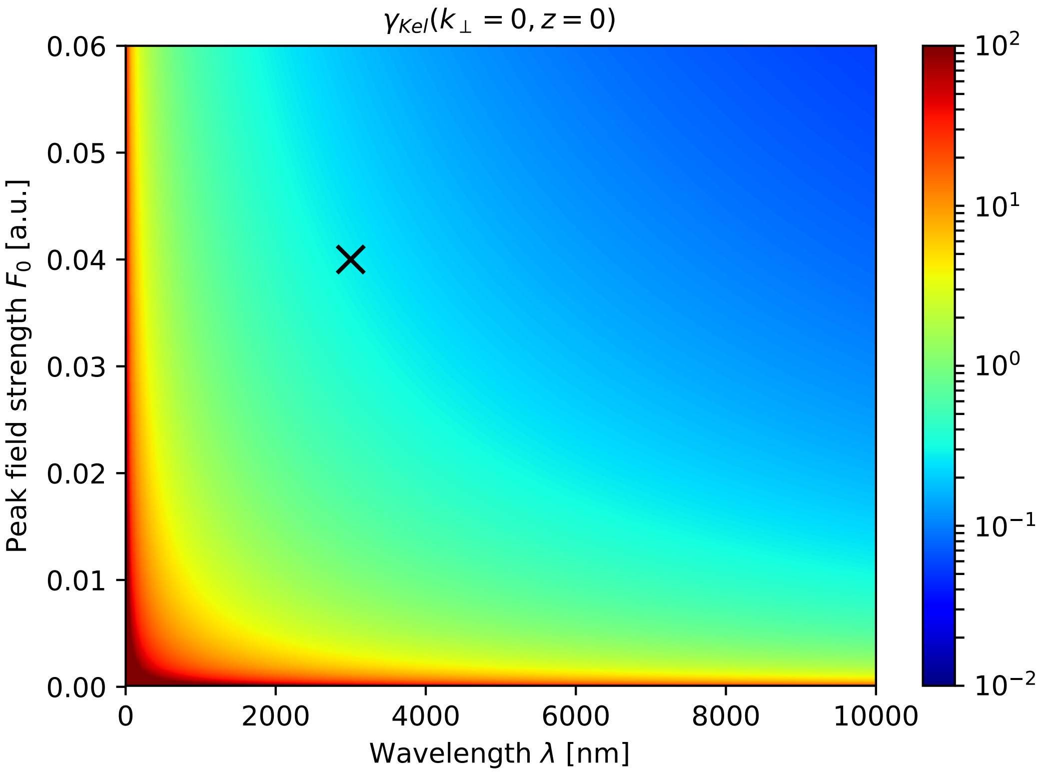

FIGURE 3.1: The laser parameter regime in which the quasi-static approximation $\gamma_{\text{Kel}}(k_\perp = 0, z = 0) \ll 1$ applies. The Keldysh parameter $\gamma_{\text{Kel}}(k_\perp = 0, z = 0)$ is shown as a function of the peak field strength F_0 and the frequency λ. The black cross indicates the laser parameters at which the momentum distribution in fig. 3.4 is calculated.

$$\begin{aligned} f(t_0, z) &= f(t_r, z) \\ &\quad + i\left(I_P(k_\perp)(t_0 - t_r) + \int_{t_r}^{t_0} \mathrm{d}t' \frac{1}{2m_e}\left(\int_{t_r}^{t'} \mathrm{d}t'' \vec{F}(t'')\right)^2 + F(t')z\right) \qquad (3.33) \\ &\approx f(t_r, z) \\ &\quad + i\left(\left(I_P(k_\perp) + F(t_r)z\right)(t_0 - t_r) + \frac{1}{3} \cdot \frac{1}{2m_e} F^2(t_r)(t_0 - t_r)^3\right) \qquad (3.34) \\ &= f(t_r, z) - \frac{2}{3}\frac{\sqrt{2m_e}}{F(t_r)}\left(I_P(k_\perp) + F(t_r)z\right)^{3/2} \quad , \qquad (3.35) \end{aligned}$$

where $f(t_r, z) = f(t_r, z = 0)$ is independent of z, and

$$\begin{aligned} g(t_0) &= F(t_0) d(z, \vec{k}_\perp) \qquad (3.36) \\ &\approx F(t_r) d(z, \vec{k}_\perp) \qquad (3.37) \end{aligned}$$

as well as

$$\left.\frac{\mathrm{d}^2 f(t,z)}{\mathrm{d}t^2}\right|_{t=t_0} \approx -\frac{F^2(t_r)}{m_e}\frac{\gamma_{\mathrm{Kel}}(k_\perp,z)}{\omega} + iz\left.\frac{\mathrm{d}F(t)}{\mathrm{d}t}\right|_{t=t_0} \tag{3.38}$$

$$\approx -\frac{F^2(t_r)}{m_e}\frac{\gamma_{\mathrm{Kel}}(k_\perp,z)}{\omega} + iz\left.\frac{\mathrm{d}F(t)}{\mathrm{d}t}\right|_{t=t_r} \quad . \tag{3.39}$$

From the requirement that $-\eta^2(z)\left.\frac{\mathrm{d}^2 f(t,z)}{\mathrm{d}t^2}\right|_{t=t_0}$ is real and positive, it follows that

$$\eta(z) = \exp\left(-\frac{i}{2}\left(\arg\left(\left.\frac{\mathrm{d}^2 f(t,z)}{\mathrm{d}t^2}\right|_{t=t_0}\right)+\pi\right)\right) \quad . \tag{3.40}$$

Using this, the inner time integral in eq. (3.18) can be evaluated:

$$M^{\mathrm{SFA}}_{\mathrm{ion}} = -\, i e^{f(t_r,z=0)} F(t_r) \tag{3.41}$$

$$\cdot \int \mathrm{d}z\ \eta(z) \sqrt{\frac{2\pi}{\left|\left.\frac{\mathrm{d}^2 f(t,z)}{\mathrm{d}t^2}\right|_{t=t_0}\right|}}\, d(z,\vec{k}_\perp) \exp\left(-\frac{2}{3}\frac{\sqrt{2m_e}}{F(t_r)}\left(I_P(k_\perp)+F(t_r)z\right)^{3/2}\right)$$

From eq. (3.15), it follows that

$$d(z,\vec{k}_\perp) = \sum_m c_{um} \int \mathrm{d}x \int \mathrm{d}y \frac{1}{(2\pi)^{3/2} r_0} e^{-i(k_x x + k_y y)}\ z\ \delta(r-r_0) Y_{lm}(\theta,\phi) \quad , \tag{3.42}$$

which, inserted into eq. (3.41), yields

$$M^{\mathrm{SFA}}_{\mathrm{ion}} = -\, i e^{f(t_r,z=0)} \frac{F(t_r)}{(2\pi)^{3/2} r_0} \tag{3.43}$$

$$\cdot \sum_m c_{um} \int \mathrm{d}^3 r\ \eta(z) \quad \sqrt{\frac{2\pi}{\left|\left.\frac{\mathrm{d}^2 f(t,z)}{\mathrm{d}t^2}\right|_{t=t_0}\right|}}\, e^{-i(k_x x + k_y y)}\ z\ \delta(r-r_0) Y_{lm}(\theta,\phi)$$

$$\cdot \exp\left(-\frac{2}{3}\frac{\sqrt{2m_e}}{F(t_r)}\left(I_P(k_\perp)+F(t_r)z\right)^{3/2}\right) \quad .$$

The exponential

$$\exp\left(-\frac{2}{3}\frac{\sqrt{2m_e}}{F(t_r)}\left(I_P(k_\perp)+F(t_r)z\right)^{3/2}\right) \tag{3.44}$$

is pronounced for $z \approx -r_0$. This can be quantified using the ratio

$$\frac{\exp\left(-\frac{2}{3}\frac{\sqrt{2m_e}}{F(t_r)}\left(I_P(k_\perp)+F(t_r)z\right)^{3/2}\right)}{\exp\left(-\frac{2}{3}\frac{\sqrt{2m_e}}{F(t_r)}\left(I_P(k_\perp)-F(t_r)r_0\right)^{3/2}\right)} \quad , \tag{3.45}$$

which is the value of the exponential part of the integrand in eq. 3.43, normalized to its value at $z = -r_0$. This ratio is shown in fig. 3.2 as a function of z for different values of $F(t_r)$. It can be seen that the exponential reaches its maximum for $z \approx -r_0$ and exponentially decreases for larger values of z. This can be used to take the only slightly z-dependent factors in eq. (3.43) out of the integral, and one obtains

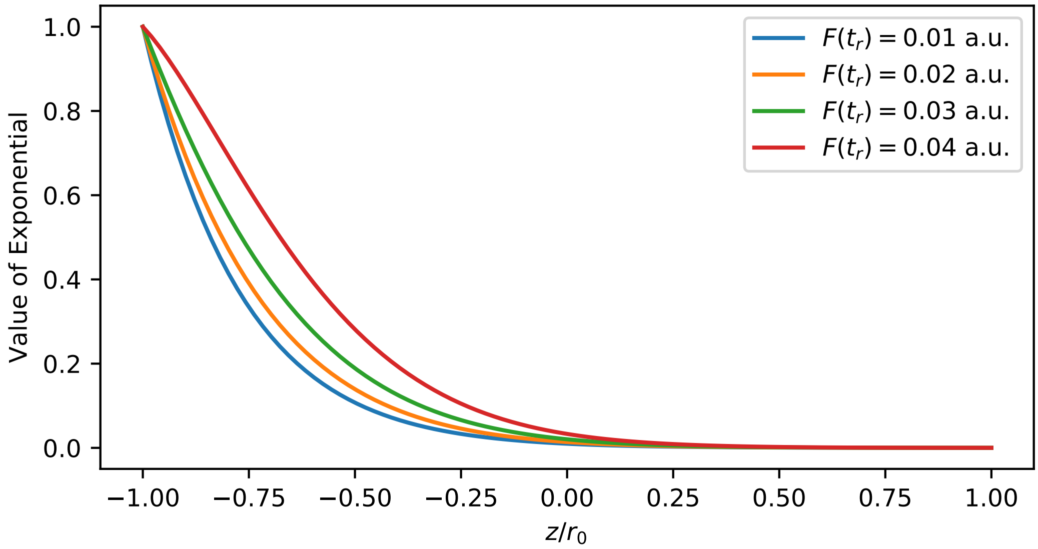

FIGURE 3.2: The ratio in eq. (3.45), i.e. the value of the exponential as a function of z, normalized to its value at $z = -r_0$, is shown for different $F(t_r)$. The final momentum is set to $k_\perp = 0$ and $k_z = -\frac{F_0}{\omega}$. Notice that for $z \approx -r_0$, the exponential reaches its maximum and exponentially decreases for larger values of z.

$$\begin{aligned} M_{\text{ion}}^{\text{SFA}} \approx & -ie^{f(t_r,z=0)}\eta(z=-r_0)\frac{F(t_r)}{(2\pi)^{3/2}r_0}\sqrt{\frac{2\pi}{\left|\frac{\mathrm{d}^2 f(t,z=-r_0)}{\mathrm{d}t^2}\Big|_{t=t_0}\right|}} \\ & \cdot \sum_m c_{um} \int \mathrm{d}^3 r\; e^{-i(k_x x + k_y y)}\; z\; \delta(r-r_0) Y_{lm}(\theta,\phi) \\ & \cdot \exp\left(-\frac{2}{3}\frac{\sqrt{2m_e}}{F(t_r)}\left(I_P(k_\perp)+F(t_r)z\right)^{3/2}\right) \quad . \end{aligned} \tag{3.46}$$

An approximation can also be used to simplify the term $e^{-i(k_x x + k_y y)}$, using the fact that nonzero k_x and k_y are suppressed exponentially because of the term $I_P(k_\perp)$ in the exponential, together with the fact that because of the $\delta(r-r_0)$-term in the integrand, $x^2+y^2+z^2=r^2$ holds. More precisely, if the product $k_\perp\sqrt{r_0^2-z^2}$ is large enough such that

$$e^{-ik_\perp\sqrt{r_0^2-z^2}} = -1, \tag{3.47}$$

the corresponding exponential is suppressed according to

$$R(z) = \frac{\exp\left(-\frac{2}{3}\frac{\sqrt{2m_e}}{F(t_r)}\left(I_P\left(k_\perp = \frac{\pi^2}{2m_e\sqrt{r_0^2-z^2}}\right) + F(t_r)z\right)^{3/2}\right)}{\exp\left(-\frac{2}{3}\frac{\sqrt{2m_e}}{F(t_r)}\left(I_P(k_\perp = 0) + F(t_r)z\right)^{3/2}\right)} \tag{3.48}$$

as a function of z. Fig. 3.3 shows the suppression $R(z)$ for different values of $F(t_r)$. The graphic shows that $R(z)$ stays well below 1 also for field strengths close to the over-the-barrier threshold, meaning that the assumption

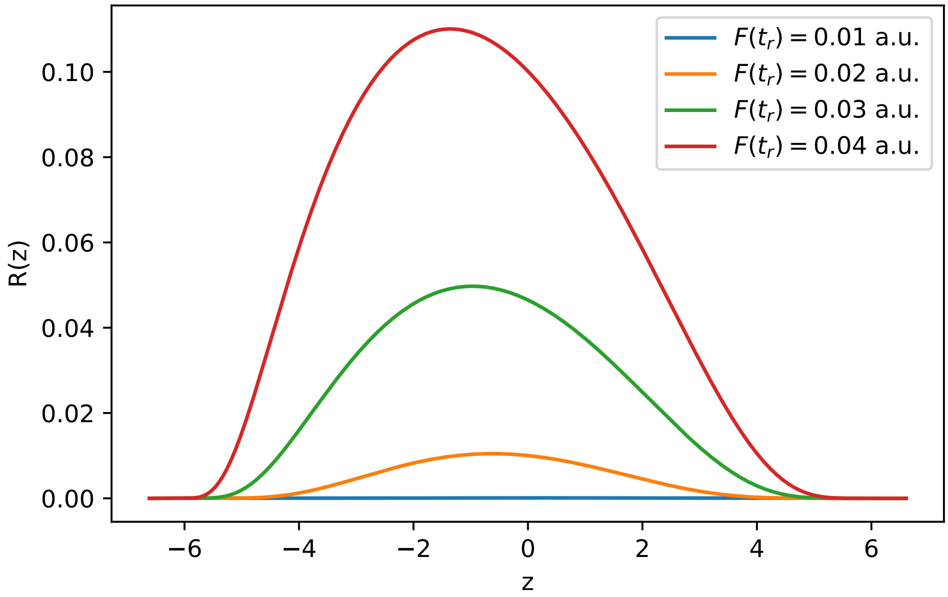

Figure 3.3: Suppression $R(z)$ (see eq. 3.48) for different values of $F(t_r)$, as specified in the legend, and as a function of z. Regardless of z, $R(z)$ stays below 0.11, indicating that the perpendicular oscillation of the plane wave can be neglected, as discussed in the text.

$$e^{-i(k_x x + k_y y)} \approx 1 \tag{3.49}$$

can be assumed for all significant contributions in the distribution of $k_\perp$. Explicit insertion of the spherical harmonics $Y_{lm}(\theta, \phi)$ according to the definition in eq. (2.29) yields

$$
\begin{aligned}
M_{\text{ion}}^{\text{SFA}} =& -i \sum_m c_{um} \delta_{m,0} e^{f(t_r, z=0)} \eta(z=-r_0) \frac{N_{lm}}{2\pi} F(t_r) r_0^2 \sqrt{\frac{2\pi}{\left| \frac{\mathrm{d}^2 f(t, z=-r_0)}{\mathrm{d}t^2} \Big|_{t=t_0} \right|}} \\
& \cdot \int \mathrm{d}x \; x \; P_{l|m|}(x) \exp\left(-\frac{2}{3} \frac{\sqrt{2m_e}}{F(t_r)} \left(I_P(k_\perp) + xF(t_r) r_0 \right)^{3/2} \right) \qquad (3.50) \\
=& -i \sum_m c_{um} \delta_{m,0} e^{f(t_r, z=0)} \eta(z=-r_0) \\
& \cdot \frac{N_{lm}}{\sqrt{2\pi}} \frac{F(t_r) r_0^2}{\sqrt{\left| -\frac{F^2(t_r)}{m_e} \frac{\gamma_{\text{Kel}}(k_\perp, z=-r_0)}{\omega} - i r_0 \, \frac{\mathrm{d}F(t)}{\mathrm{d}t} \Big|_{t=t_r} \right|}} \\
& \cdot \int \mathrm{d}x \; x \; P_{l|m|}(x) \exp\left(-\frac{2}{3} \frac{\sqrt{2m_e}}{F(t_r)} \left(I_P(k_\perp) + xF(t_r) r_0 \right)^{3/2} \right) \quad . \qquad (3.51)
\end{aligned}
$$

The remaining integral can be solved numerically using, for example, the function `integrate.quad` contained in the `scipy` library [35] for `python`.

3.1.4 Ionization yields

The ionization yield can be calculated from the ionization matrix elements $M_{\text{ion}}^{\text{SFA}}$ by integrating over all possible values of k_z and $k_\perp$,

$$
\begin{aligned}
P_{\text{ion}} &= \int \mathrm{d}^3k \; |M_{\text{ion}}^{\text{SFA}}(\vec{k})|^2 \qquad (3.52) \\
&= \int_0^\infty \mathrm{d}k_\perp \int_{-\infty}^\infty \mathrm{d}k_z \; 2\pi k_\perp |M_{\text{ion}}^{\text{SFA}}(k_\perp, k_z)|^2 \qquad (3.53) \\
&=: \int \mathrm{d}k_\perp \int \mathrm{d}k_z \; \frac{\mathrm{d}P_{\text{ion}}}{\mathrm{d}k_z \mathrm{d}k_\perp} \quad . \qquad (3.54)
\end{aligned}
$$

As discussed in paragraph 2.3.3.2.1, the SFA ionization amplitude in $\Lambda = (0,0)$-partitioning neglects saturation effects. This has to be accounted for if the ionization probabilities come close to 1. The correct ionization rate $P_{\text{ion}}^{\text{sat}}(t)$ obeys the differential equation

$$
\frac{\mathrm{d}\left(1 - P_{\text{ion}}^{\text{sat}}(t)\right)}{\mathrm{d}t} = -\Gamma(t)(1 - P_{\text{ion}}^{\text{sat}}(t)) \quad , \qquad (3.55)
$$

that takes into account the depletion of the ground state according to the term $1 - P_{\text{ion}}^{\text{sat}}(t)$. $\Gamma(t)$ is the quasi-static ionization rate at time t. The full solution of eq. (3.55) is, using the starting condition $P_{\text{ion}}^{\text{full}}(t_i) = 0$,

$$
P_{\text{ion}}^{\text{sat}}(t) = 1 - e^{-\int_{t_i}^{t} \mathrm{d}t' \; \Gamma(t')} \quad . \qquad (3.56)
$$

If the depletion of the initial state is neglected, the differential equation reads

$$\frac{\mathrm{d}\left(1 - P_{\text{ion}}(t)\right)}{\mathrm{d}t} = -\Gamma(t) \quad , \tag{3.57}$$

which is solved by

$$P_{\text{ion}}(t) = \int_{t_i}^{t} \mathrm{d}t' \; \Gamma(t') \quad , \tag{3.58}$$

taking into account the correct starting condition.

Comparing the full solution $P_{\text{ion}}^{\text{sat}}(t)$ to the approximate result $P_{\text{ion}}(t)$ yields

$$P_{\text{ion}}^{\text{sat}}(t) = 1 - e^{-P_{\text{ion}}(t)} \quad . \tag{3.59}$$

Because the ionization yield $P_{\text{ion}}(t)$ in eq. (3.52) is obtained neglecting depletion effects, more accurate results for the ionization yields are obtained when correcting it according to eq. (3.59). For small depletions, this difference is negligible, but it becomes important for ionization probabilities near 1.

3.1.5 Results

According to the rigid-rotor model discussed in section 2.1.1.2, the original state of the single active electron is the HOMO level, i.e. the $(l = 5)$-level. In the approximation discussed above, the ionization matrix elements for all m quantum numbers except for $m = 0$ vanish. Leaving aside symmetry-adapted states for now, results are calculated for $l = 5$ and $m = 0$ therefore. A laser wavelength of $\lambda = 3000\,\text{nm}$ is chosen, which corresponds to a pulse duration of the half cycle of

$$T_{\text{HC}} = \frac{T}{2} = \frac{\lambda}{2c} = 5\,\text{fs} \quad . \tag{3.60}$$

The field strength is set to 0.04 a.u., which corresponds to a peak intensity of $5.62 \cdot 10^{13}\text{W/cm}^2$. This corresponds to a Keldysh parameter of $\gamma \approx 0.33$. The laser parameters used are also indicated as a black cross in fig. 3.1.

3.2 Numerical Approach

In order to assess the applicability of the approximations presented in section 3.1, it is instructive to describe single ionization of C_{60} in a way independent of the first result and then compare the results. Obviously, as already discussed, the full numerical solution of the 60-body problem of the π-electrons is not feasible, which means that approximations have to be introduced here too.

In this chapter, an *ab initio* full numerical solution of the TDSE of a single active electron in a model potential exposed to a pulse of similar shape to the one in eq. (3.1) is presented. This means that, while it is still assumed that the ionization can be described using a single active electron and an assumption is made with respect to the electronic structure of the molecule, the SFA

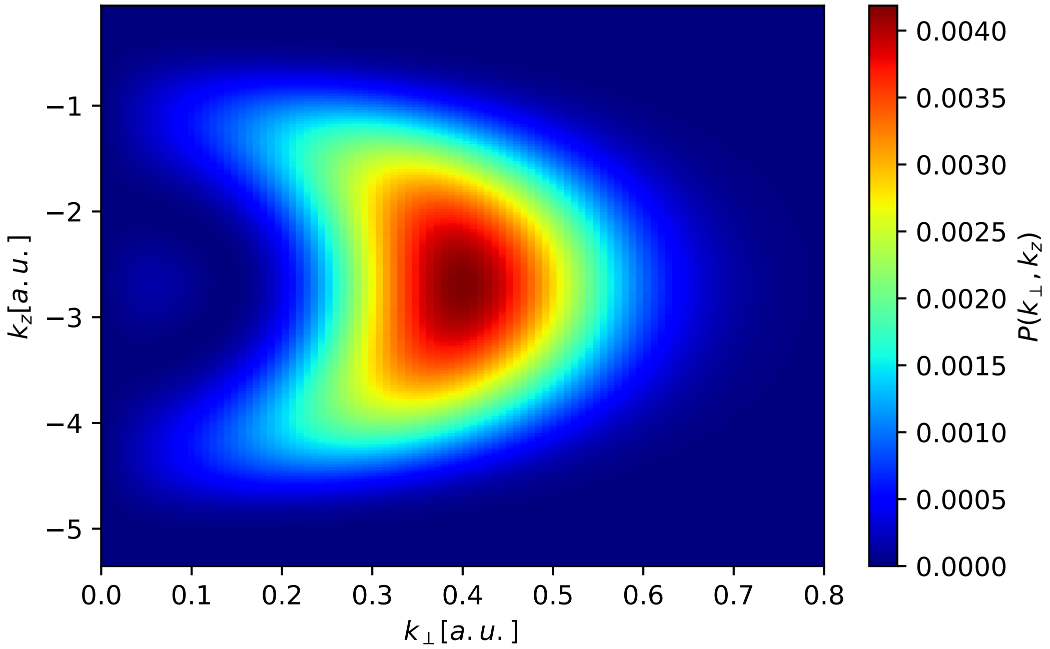

FIGURE 3.4: Momentum distribution after single ionization $P(k_\perp, k_z) := \frac{\mathrm{d}P_{\mathrm{ion}}}{\mathrm{d}k_z \mathrm{d}k_\perp} = 2\pi k_\perp |M_{\mathrm{ion}}^{\mathrm{SFA}}(k_\perp, k_z)|^2$. The results are calculated for $l = 5$ and $m = 0$, with the laser parameters $F_0 = 0.04\,\mathrm{a.u.}$ and $\lambda = 3000\,\mathrm{nm}$. The z-momenta are symmetrical around $-F_0/\omega$, corresponding to a real part of the saddle point exactly at the maximum of the laser pulse. For growing perpendicular momenta $k_\perp$, the ionization probability vanishes exponentially.

and saddle point approximations are not used. Instead, the B spline method described in 2.1.2 and 2.3.2 is used. The model potential imitates the almost spherical structure of C_{60}, and its parameters are varied such that the resulting numerically obtained ground state of the electron in the model potential has the energy $E_0 = -I_P$. Here, I_P is the ionization potential for single electron ionization of C_{60} that is known experimentally.

3.2.1 Spherical Model Potential

Similarly to the rigid-rotor model, it is advisable to exploit the almost spherical structure of C_{60} in some way when approximating the electronic ground state of the single active electron of C_{60}. For the analytical approach in section 3.1, the rigid-rotor model was used which explicitly assumes spherical harmonics as the ground state. In this chapter, the ground state is not explicitly assumed, but the model potential in which it exists.

The easiest model potential $V(\vec{r})$ for a spherical shell is a radial potential well of the form

$$V(\vec{r}) = V(r) = \begin{cases} -V_0 & \text{if } |r - r_0| \leq \frac{\Delta}{2} \\ 0 & \text{otherwise} \end{cases} . \tag{3.61}$$

The radius r_0 of C_{60} is assumed to be 3.5 Å [6], the same number was also used for the rigid-rotor model in section 2.1.1.2. The width of the potential well Δ is set to 2 a.u., which is a little bit less than the diameter of a carbon atom. The remaining free parameter V_0, i.e. the depth of the potential well, can then be tuned such that the resulting ground state energy E_1 fits the experimental value of 7.65 eV [7]. To this end, an electronic structure calculation is performed for a single electron in a model potential of the form in eq. (3.61). More precisely, the corresponding field-free Hamiltonian

$$\hat{\mathrm{H}}_0 = \hat{\mathrm{T}} + V(\hat{\mathrm{r}}) = \frac{\hat{\mathrm{p}}^2}{2m_e} + V(\hat{\mathrm{r}}) \tag{3.62}$$

is diagonalized in a finite orthonormal B spline basis $\{|i\rangle\}$, as discussed in section 2.1.2. This is done using an existent code from the AMO group at Humboldt-Universität zu Berlin that is a modified version [22] of a code from the group of P. Lambropoulos [23]. This code was slightly extended for this work to support the calculation for the model potential given in eq. (3.61). As described in section 2.1.2, one obtains the representation of the eigenstates $\{|\psi_p\rangle\}$ in the finite B spline basis $\{|i\rangle\}$, i.e. one obtains the coefficient matrix $\mathbb{C}$ that fulfills the generalized eigenvalue problem

$$\mathbb{H}_0\mathbb{C} = \mathbb{E}\mathbb{S}\mathbb{C} \quad , \tag{3.63}$$

where $\mathbb{H}_0$ is the Hamiltonian matrix with the coefficients

$$(\mathbb{H}_0)_{ij} = \langle i|\hat{\mathrm{H}}_0|j\rangle \quad , \tag{3.64}$$

$\mathbb{E}$ is a diagonal matrix with the energies on the diagonal

$$\mathbb{E}_{ij} = E_p\delta_{pi}\delta_{pj} \quad , \tag{3.65}$$

and $\mathbb{S}$ is the overlap matrix with the coefficients

$$\mathbb{S}_{ij} = \langle i|j\rangle \quad . \tag{3.66}$$

The model potential together with the ground state energy E_0 found using the B spline basis set C (see section 3.2.4) is shown in fig. 3.5. For the potential depth, $V_0 = 0.58$ a.u. is used. The convergence of the calculation of the ground state energy with respect to the corresponding basis sets is discussed in section 3.2.4.

3.2.2 Time-Dependent Field

Once the electronic structure calculation is performed, i.e. the eigenstates and their pairwise transition dipole moments are known, the initially present ground state $|\psi_0\rangle$ can be propagated in the time-dependent field in dipole approximation and length gauge as discussed in section 2.3.2. The implementation of the time propagation in the `AMO_TOOLS` does not yet support time-dependent fields $\vec{F}(t)$

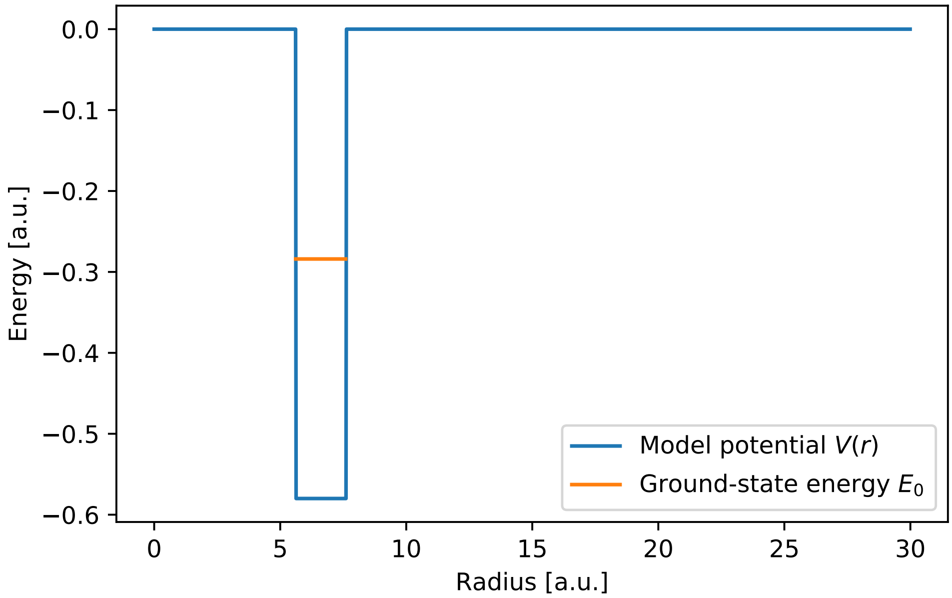

FIGURE 3.5: Model potential used for the numerical approach alongside with the resulting ground state energy found using the B spline code (basis set C). For the potential depth, $V_0 = 0.58\,\text{a.u.}$ is used.

of the functional form in eq. (3.1). However, the time-dependent field

$$\vec{F}_{\text{num}}(t) = \begin{cases} 0 & t < t_i = 0 \\ -\vec{e}_z \frac{4F_0\omega^2}{\pi^2} t(t - \frac{\pi}{\omega}) & 0 \leq t \leq \frac{\pi}{\omega} \\ 0 & t > t_f = \frac{\pi}{\omega} \end{cases} \tag{3.67}$$

is already implemented. As can be seen from fig. 3.6, $\vec{F}(t)$ and $\vec{F}_{\text{num}}(t)$ are very similar to each other, such that the results from the numerical approach remain comparable to the analytical result presented in section 3.1. Therefore, $\vec{F}_{\text{num}}(t)$ is used as the time-dependent field for the numerical approach.

3.2.3 Calculation of Ionization Yields

After the end of the pulse at $t_f = \pi/\omega$, the ground state $|\psi_0\rangle$ present at $t_i = 0$ has propagated into the state $\psi_{0,f}$. The ionization yield P_{ion} is then defined as the probability to find the system in an ionized state during a measurement, i.e. the probability to find its wave function in an eigenstate of $\hat{\text{H}}_0$ with an energy larger than or equal to 0. Hence,

$$P_{\text{ion}}^{\text{num}} = \sum_{j:\ E_j \geq 0} |\langle\psi_j|\psi_{0,f}\rangle|^2 \quad . \tag{3.68}$$

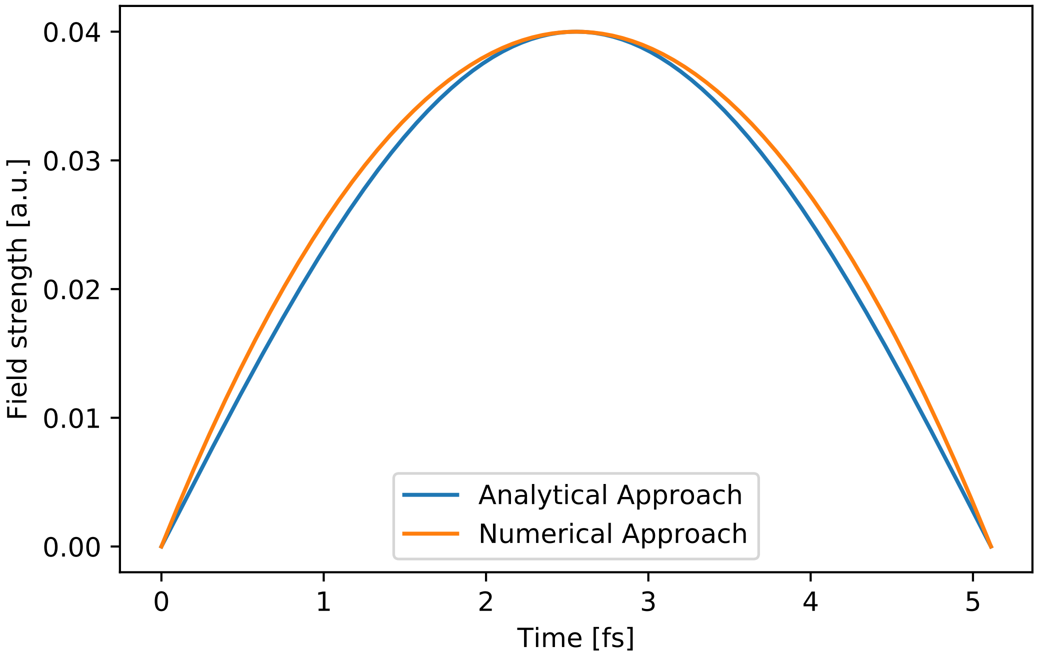

FIGURE 3.6: Comparison of the z components of the fields used in the analytical approach ($F_z(t)$) and in the numerical approach ($F_{\mathrm{num},z}(t)$). The pulse duration corresponds to $\lambda = 3000\,\mathrm{nm}$, and the peak field strength is $F_0 = 0.04\,\mathrm{a.u.}$ Both shapes are comparable.

3.2.4 Basis Sets and Convergence

The calculation of the field-free eigenstates $\{|\psi_p\rangle\}$ is done numerically in a finite B spline basis as described in section 2.1.2. Different B spline basis sets of different size are used to check for convergence. For all basis sets, the order of the B splines is set to $k = 9$ and the first nonzero knot position is set to $\Delta r = 0.05\,\mathrm{a.u.}$ For the angular part (see eq. (2.46)), the l-quantum numbers $l = 0$ through $l = l_{\max}$ are used. The parameter $l_{\max}$ is varied as well to check the convergence, as described later on. As, without loss of generality, the quantization axis of the initial state is chosen to point into the direction of the field, there is no coupling between different m quantum numbers (see eq. 2.100), such that the basis set can be restricted to only include angular parts with $m = 0$. The complete basis set files can be found in appendix B, and the most important features are summarized in table 3.1. For all calculations, the potential parameters $\Delta = 2\,\mathrm{a.u.}$ and $V_0 = -0.58\,\mathrm{a.u.}$ are used. Since for any possible state $|\psi\rangle$

$$\langle\psi|\hat{\mathrm{H}}_0|\psi\rangle \geq E_0 \quad , \tag{3.69}$$

the ability of a basis set to describe the ground state can be assessed by comparing the resulting ground state energies. As was to be expected, both increasing $R_{\max}$ and the density of B splines $R_{\max}/N$ results in a better ground state energy. However, while varying the parameters over a wide range, the ground

Basis set	$R_{\max}$ [a.u.]	#B splines N	$N/R_{\max}$ [a.u.]	E_0 [a.u.]
A	6000	1000	0.2	-0.2886
B	3000	1000	0.3	-0.2809
C	3000	2000	0.7	-0.2840
D	600	1000	1.7	-0.2797
E	600	3000	5.0	-0.2842

TABLE 3.1: Basis sets used for the electronic structure calculation of the model potential in 3.61, alongside with the resulting ground state energy E_0. For the angular part, the angular momentum quantum numbers $l = 0$ through $l = l_{\max}$ are used. The parameter $l_{\max}$ does not influence the energy of the s-symmetric ground state, therefore convergence of the results with respect to $l_{\max}$ will be discussed later on. The width of the potential well is fixed to $\Delta = 2\,\text{a.u.}$ The potential depth is tuned such that the ground state energy E_0 is close to the target $-I_P = 7.65\,\text{eV} \approx -0.281\,13\,\text{a.u.}$, and was set to $V_0 = -0.58\,\text{a.u.}$

state energies stay within a 3% window of each other and the target ground state energy $-I_P = 7.65\,\text{eV} \approx -0.28113$. In section 3.3, it can be seen that the relative deviations between the numerical and the analytical model are on a much larger scale, therefore this level of convergence is considered to be sufficient for the comparison.

The B spline basis not only has to be able to describe the ground state in sufficient accuracy, but, in order to describe ionization processes, it must also represent the excited and continuum states. In order to estimate the basis parameters needed for that, a semiclassical estimation can be done. Consider a classical electron resting with momentum $\vec{p}_0 = \vec{0}$ at the origin $\vec{r}_0 = \vec{0}$ at $t = 0$, before the onset of the electric field (see eq. (3.1)). Once the field is nonzero, the electron is accelerated by the field pointing in positive z direction until the end of the pulse at $t = \frac{\pi}{\omega}$. In dipole approximation, the magnetic field component can be neglected, and therefore the equation of motion for the classical electron reads

$$\frac{\partial \vec{r}(t)}{\partial t} = \frac{\vec{p}(t)}{m_e} \tag{3.70}$$

$$\frac{\partial \vec{p}(t)}{\partial t} = -F(t) \quad , \tag{3.71}$$

where $F(t)$ is the electric field component defined in eq. (3.1). Therefore, the trajectory of the electron for $t > 0$ reads

$$\vec{r}(t) = -\frac{1}{m_e}\int_0^t \mathrm{d}t' \int_0^{t'} \mathrm{d}t'' F(t'') \quad . \tag{3.72}$$

The maximum $|\vec{p}|_{\max} = |\vec{p}(t_f)|$ is reached by the end of the pulse at $t_f = \frac{\pi}{\omega}$, and the motion of the electron is uniform after that. The maximum $|\vec{p}|$ and $|\vec{r}|$

the basis set has to describe therefore are

$$|\vec{p}\,|_{\max} = |\vec{p}(t_f)| \quad \text{and} \quad |\vec{r}\,|_{\max} = |\vec{r}(t_f)| \quad . \tag{3.73}$$

This allows one to give an upper boundary estimate for the B spline box size

$$R_{\max} \approx |\vec{r}\,|_{\max} \quad , \tag{3.74}$$

and, because the wavelength of a plane wave with momentum $|\vec{p}|_{\max}$ is $\lambda_{\min} = \frac{2\pi}{|\vec{p}|_{\max}}$, it also allows for an order-of-magnitude estimate for the required B spline density

$$\frac{N_{\min}}{R_{\max}} \approx \frac{2}{\lambda_{\min}} = \frac{|\vec{p}\,|_{\max}}{\pi} \quad , \tag{3.75}$$

where it was assumed that 2 B spline functions are required to describe a full plane wave period. This is of course a somewhat arbitrary assumption, but it can serve as an order-of-magnitude estimate. Notice however that this estimation is a quite conservative upper limit, as the majority of the ionization does not happen at the beginning of the pulse, but around the peak of the field strength. As $|\vec{r}|_{\max}$ depends “quadratically” on the time the electron spends in the field, this leads to a significant underestimation of the capability of the basis set.

3.3 Comparison of the Analytical and the Numerical Approach

To compare the analytical approach and the numerical approach described previously, one can compare ionization yields, i.e. compare $P_{\text{ion}}^{\text{sat}}(t)$ in equation (3.59) to $P_{\text{ion}}^{\text{num}}$ in equation (3.68). The analytical result is calculated for

$$|l_{\text{ini}}, m_{\text{ini}}\rangle = |0, 0\rangle \tag{3.76}$$

as the initial rigid-rotor state (see eq. (2.28)). For the numerical calculation, the ground state of the model potential is chosen as the initial state, which has s-symmetry as well.

As discussed in section 2.3.2, the numerical results have to be checked for convergence both with respect to the B splines for the radial part and the maximum angular momentum quantum number $l_{\max}$ of the angular part. To this end, the numerical result is calculated for the different B spline basis sets summarized in table 3.1, and the value of $l_{\max}$ is varied between 10, 15, and 20. Fig. 3.7 shows the results for the highest value $l_{\max} = 20$. The plot is obtained for a fixed wavelength $\lambda = 3000\,\text{nm}$ and varying peak intensity. The numerical solutions are drawn in a straight line where the basis is sufficiently dense and the box size sufficiently large, i.e.

$$R_{\max} \leq |\vec{r}\,|_{\max} \quad \text{and} \quad \frac{N}{R_{\max}} \leq \frac{|\vec{p}\,|_{\max}}{\pi} \quad , \tag{3.77}$$

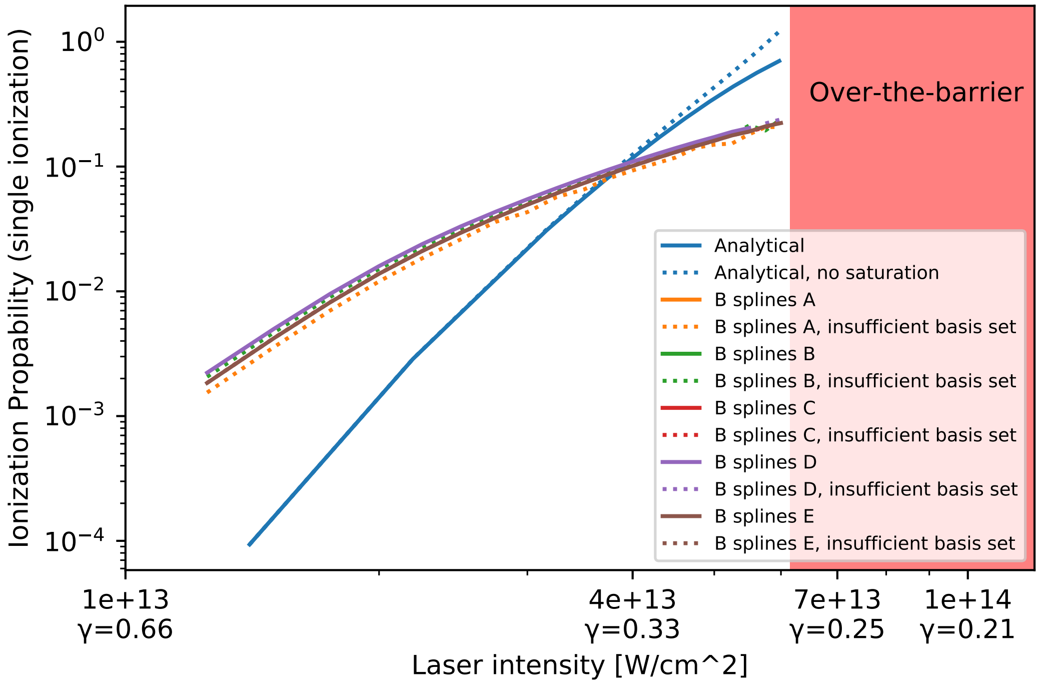

FIGURE 3.7: Comparison of the ionization yields obtained with the analytical approach described in section 3.1 to the ionization yields obtained with the numerical approach described in section 3.2, both as a function of the peak intensity. The analytical result is calculated for $|l_{\text{ini}}, m_{\text{ini}}\rangle = |0,0\rangle$ (see eq. (2.28)) as the initial state. For the numerical calculation, the ground state of the model potential in eq. (3.61) is chosen as the initial state, which has s-symmetry as well. The numerical calculation is done for different B spline basis sets as specified in the legend and summarized in table 3.1, while the value $l_{\text{max}} = 20$ is chosen for all plots in this figure. The wavelength is 3000 nm, which corresponds to a half-cycle duration of 5 fs.

and as a dotted line where this is not the case. The basis sets D and E fulfill these requirements for (almost) all intensities, and only deviate from each other by around 10%.

In fig. 3.8, the numerical results are compared with each other while varying the maximum angular momentum quantum number l_{max}. It shows the relative deviation of the results for $l_{\text{max}} = 10$ and $l_{\text{max}} = 15$ from the result for $l_{\text{max}} = 20$ for each B spline basis set. It can be seen that the results deviate from each other by 10% at most in the worst case of the smallest basis set A, while this deviation goes down to approximately 3% at most in the case of basis set E. This deviation is smaller than the relative deviation between basis sets D and E for $l_{\text{max}} = 20$, which is on the order of 10%, as already mentioned. For lower intensities, the longitudinal acceleration of the ionized wave packet in the electric field is smaller, therefore states with a larger value of l are not reached as fast and the convergence with respect to l_{max} becomes better, as can be seen from fig. 3.8 as well.

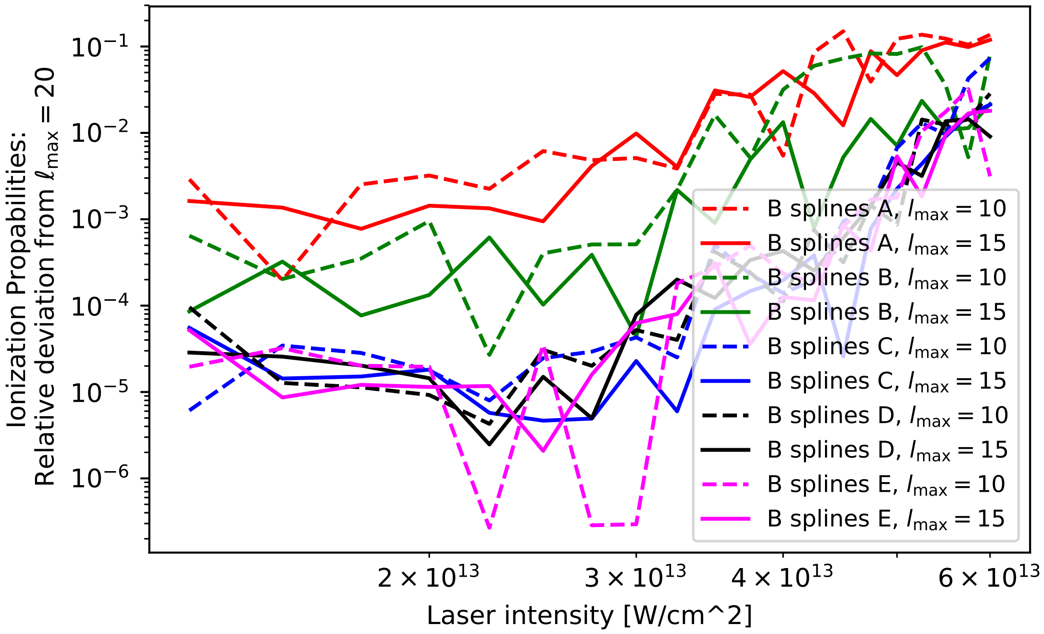

FIGURE 3.8: For the different B spline basis sets specified in the legend and summarized in table 3.1, the numerical results for different maximum angular momentum quantum numbers l_{max} are compared. This is done by showing the relative deviation of the results for $l_{max} = 10$ and $l_{max} = 15$ from the result for $l_{max} = 20$ for each B spline basis set. The ground state of the model potential in eq. (3.61) is chosen as the initial state. The wavelength is 3000 nm, which corresponds to a half-cycle duration of 5 fs.

However, fig. 3.7 clearly shows that the results of the analytical approach and the numerical approach are different in their slope in the double-logarithmic plot. Also from fig. 3.7, it can be seen that the laser regime used for the calculation is not clearly quasi-static, as the Keldysh parameter ranges from values around 0.6 to values around 0.3. This is not ideal for a comparison, as the analytical approach assumes quasi-static laser parameters while the numerical approach does not. As the field strength can not be increased without leaving the tunneling regime, an alternative is to increase the pulse duration.

Fig. 3.9 shows the comparison between analytical and numerical approach for $\lambda = 8000\,\text{nm}$. Here, all lines are dotted as none of the basis set shown satisfies the conservative conditions formulated in section 3.2.4. A “sufficient” basis set would require about 17000 basis functions, which is not feasible. Hence, the numerical results are much more noisy compared to fig. 3.7. This noise can serve as an estimate for the level of convergence of the final result.

The convergence with respect to the parameter l_{max} is shown in fig. 3.10. Again, the relative deviation of the results for $l_{max} = 10$ and $l_{max} = 15$ from the result for $l_{max} = 20$ for each B spline basis set is shown. As expected, the results are much more noisy with respect to the parameter l_{max} as well. Furthermore, the relative deviations are less consistent with respect to their dependence on the B spline basis set and the intensity than in the case of $\lambda = 3000\,\text{nm}$. In

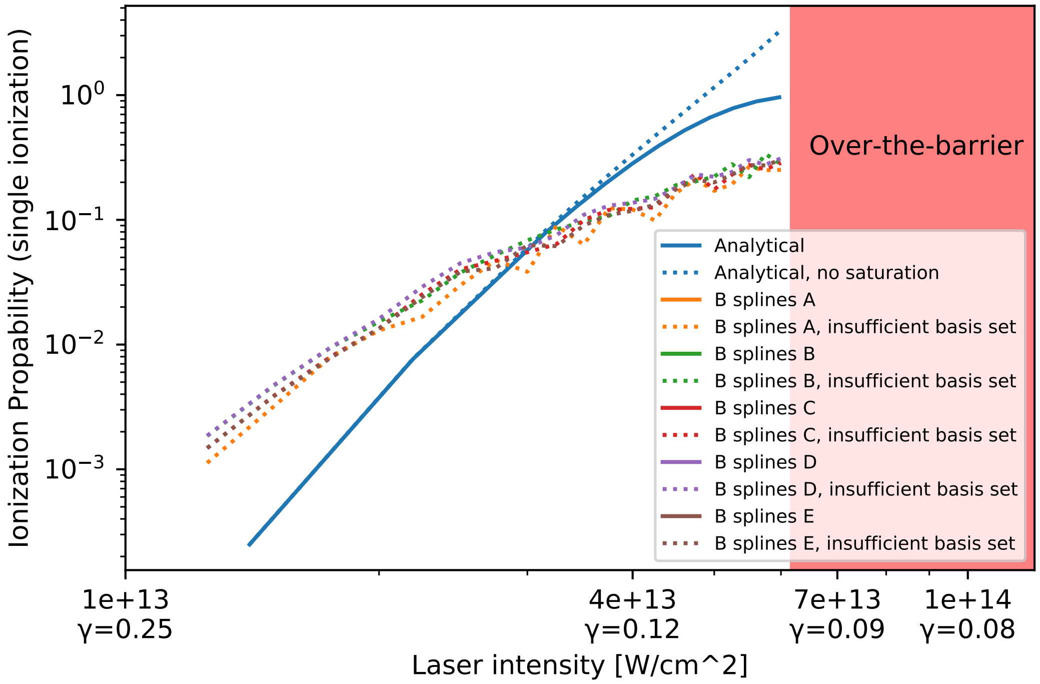

FIGURE 3.9: Comparison of the ionization yields obtained with the analytical approach described in section 3.1 to the ionization yields obtained with the numerical approach described in section 3.2, both as a function of the peak intensity. The analytical result is calculated for $|l_{\text{ini}}, m_{\text{ini}}\rangle = |0,0\rangle$ (see eq. (2.28)) as the initial state. For the numerical calculation, the ground state of the model potential in eq. (3.61) is chosen as the initial state, which has s-symmetry as well. The numerical calculation is done for different B spline basis sets as specified in the legend and summarized in table 3.1, while the value $l_{\text{max}} = 20$ is chosen for all plots in this figure. The wavelength is 8000 nm, which corresponds to a half-cycle duration of 13 fs. As all basis sets are insufficient to describe the ionization following the conservative estimate in section 3.2.4, the numerical results are all dotted.

the worst case, the relative deviations reach up to 50%. This number is on the order of magnitude of the relative deviations for different B splines shown in fig. 3.9.

While the results are more noisy for the wavelength $\lambda = 8000\,\text{nm}$, it is significant that the difference in slope between the numerical and the analytical approach in the double logarithmic plot in fig. 3.9 becomes less pronounced for $\lambda = 8000\,\text{nm}$ compared to $\lambda = 3000\,\text{nm}$. While the curves still differ in their slope, they agree on the order of magnitude. This is an indication that the approximation works better in the long-wavelength regime.

In this section, a comparison of the SFA-based (“analytical”) approach to the TDSE-based (“numerical”) approach was presented, the former assuming a rigid-rotor state as initial state, and the latter assuming the ground state of a spherical box potential as initial state. It was found that while both approaches

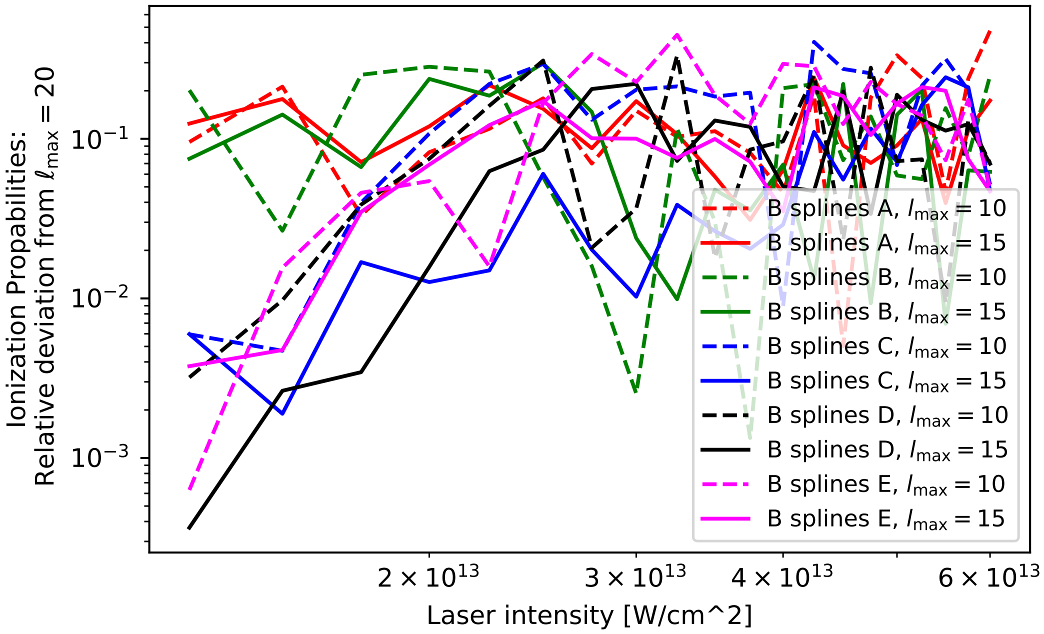

FIGURE 3.10: For the different B spline basis sets specified in the legend and summarized in table 3.1, the numerical results for different maximum angular momentum quantum numbers $l_{\max}$ are compared. This is done by showing the relative deviation of the results for $l_{\max} = 10$ and $l_{\max} = 15$ from the result for $l_{\max} = 20$ for each B spline basis set. The ground state of the model potential in eq. (3.61) is chosen as the initial state. The wavelength is 8000 nm, which corresponds to a half-cycle duration of 13 fs.

predict different ionization probabilities, they agree on the order of magnitude. A possible explanation for the remaining difference is that the wavelength regime for which the comparison was done is not clearly quasi-static, while moving to longer wavelengths is not possible due to computational limitations to the numerical method.

While the solution of a model potential TDSE for a single active electron is numerically demanding but feasible, it is very hard to describe double ionization in a 2-electron system. The doubly ionized states require a basis of size $\mathcal{O}(N^2)$, provided that for the same laser parameters a basis of size $\mathcal{O}(N)$ was sufficient to obtain convergent results in the single-active-electron case. However, the SFA calculation is so lightweight that it can be generalized to the 2-electron case. Hence, the following chapter is concerned with the description of 2-electron ionization of C_{60}, based on the model developed in this chapter.

Chapter 4

Correlated Double Ionization of C_{60}

In chapter 3, a model to describe the single ionization of C_{60} in a strong electric field was presented. In this chapter, this approach is extended to the 2-electron case. Again, as in chapter 3, a C_{60} molecule exposed to a laser field of the form

$$\vec{F}(t) = \begin{cases} 0 & t < t_i = 0 \\ \vec{e}_z F_0 \sin(\omega t) & 0 \leq t \leq \frac{\pi}{\omega} \\ 0 & t > t_f = \frac{\pi}{\omega} \end{cases} \tag{4.1}$$

is considered. However, in contrast to chapter 3, this chapter aims at describing the correlated ejection of 2 electrons during the laser pulse. Therefore, it is assumed in this chapter that the removal of the two electrons originally bound in the C_{60} molecule can be described using the 2-body wave packet of the 2 active electrons moving in the mean field created by the rest of the electronic distribution.

4.1 Sequential and Simultaneous Channels in the Strong-Field Approximation

This chapter aims at describing the transition of the 2 electrons from a fully bound state into a doubly ionized state. Within the strong-field approximation (SFA), the molecular potential is neglected, which means that no intermediate bound states are taken into account. Consequently, there are 2 different families of ionization amplitudes that have to be taken into account when describing double ionization within SFA.

Firstly, the conceptually simpler case is the direct transition of the doubly bound state into a doubly ionized state, i.e. a correlated Coulomb wave in the 2-electron continuum. This direct ionization process removing both electrons is called simultaneous ionization in the following. Secondly, double ionization in the picture provided by the strong-field approximation can also happen sequentially, through the transition of the doubly bound state into an intermediate state, where “one” electron is bound and the “other” has been ejected, followed by a transition of this singly ionized state into a doubly ionized state[1]. This 2-step process is called sequential ionization in the following. Fig. 4.1 shows a schematic representation of both processes.

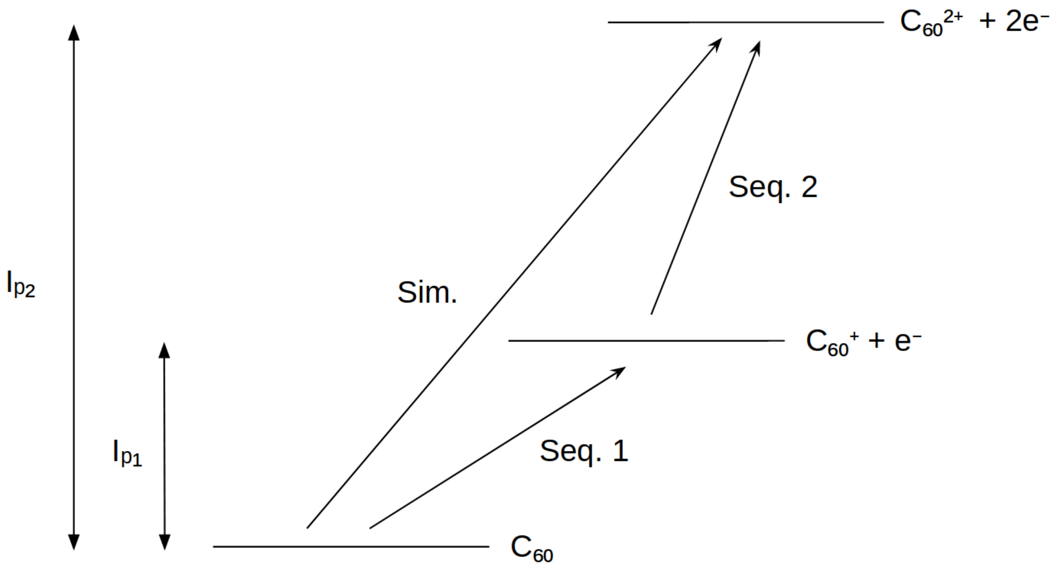

FIGURE 4.1: Transition scheme from the non-ionized state (C_{60}) into the singly ionized ($C_{60}{}^{+} + e^{-}$) and doubly ionized ($C_{60}{}^{2+} + 2\,e^{-}$) states. In this chapter, the direct channel is called simultaneous ionization and is discussed in section 4.2, while the indirect channel via the singly ionized state is called sequential and is discussed in section 4.3. Of course, there is a continuum of both singly and doubly ionized states, only the states with the lowest energy are shown here.

Fig. 4.2 gives an overview of the parameters of the final state of the system for both the case of simultaneous and sequential ionization. In the case of simultaneous ionization (fig. 4.2a), 2 electrons are removed at the same time from the C_{60} molecule, forming a 2-electron state in the continuum. The center of mass of this 2-electron state is accelerated in the field and detected with momentum $\vec{K}$ after the pulse. While the relative coordinate is not coupled to the external field in dipole approximation, the electrons are interacting with each other via Coulomb repulsion. The energy of the relative motion $E = \frac{k^2}{2\mu}$, where μ is the reduced mass, contains *both kinetic and potential* energy contributions. After some time, the electronic wave packets are pushed away from each other sufficiently far that the energy of the relative motion has become purely kinetic, therefore k is the momentum of the relative motion in the limit $t \to \infty$. Finally, the rotational state of the 2-electron system is determined by the angular momentum quantum numbers l and m.

In the case of sequential ionization (fig. 4.2b), both electrons are ejected at different points in time. After the ionization of the first electron at t_1, it is

---

[1] What is meant by "first" and "second" electron here are the degrees of freedom of the wave function associated with the first or second particle. Obviously, the 2 active electrons are interchangeable, and the 2-electron state is antisymmetric in the particle indices.

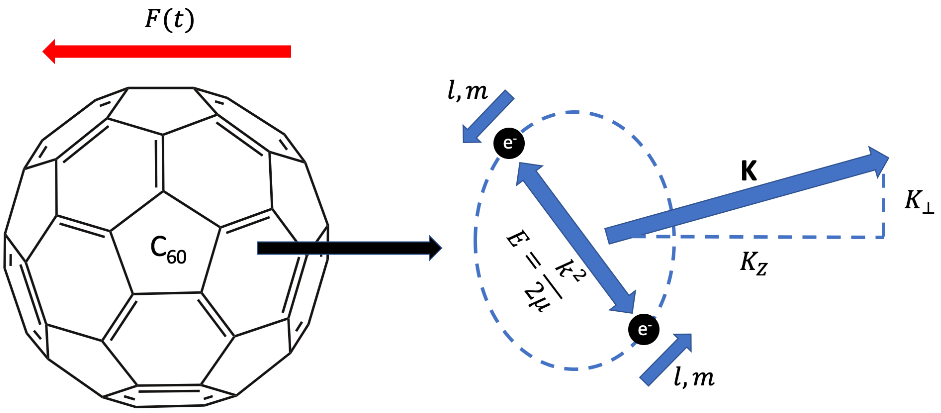

(A) Simultaneous double ionization

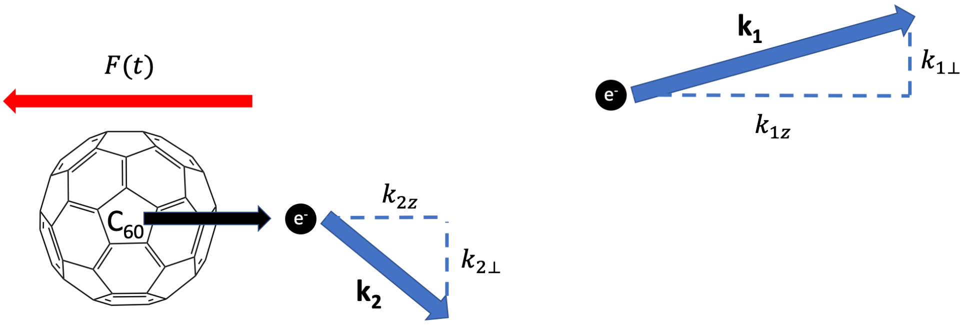

(B) Sequential double ionization

FIGURE 4.2: Schematic overview of the parameters of the final state after ionization in (A) simultaneous and (B) sequential double ionization.

accelerated in the field and detected with momentum $\vec{k}_1$ after the end of the pulse. The second electron is ejected at a later point in time $t_2 > t_1$ and detected with momentum $\vec{k}_2$ after the end of the pulse. Assuming that the repulsion of the 2 electrons after ionization is low[2], their relative momentum

$$\vec{k} = \frac{1}{2}\left(\vec{k}_2 - \vec{k}_1\right) \tag{4.2}$$

measured at the detector after the pulse is the same as their relative momentum at t_2.

The simultaneous channel is treated in section 4.2, and the sequential channel is treated in section 4.3.

4.2 Correlated Simultaneous Ionization

4.2.1 Time-Dependent Hamiltonian

The time-dependent Hamiltonian $\hat{\mathrm{H}}(t)$ of the 2 active electrons reads

$$\hat{\mathrm{H}}(t) = \hat{\mathrm{H}}_0 + \hat{\mathrm{H}}_I(t) \tag{4.3}$$

in length gauge, where $\hat{\mathrm{H}}_0$ is the time-independent part

$$\hat{\mathrm{H}}_0 = \hat{\mathrm{h}}(1) + \hat{\mathrm{h}}(2) + \hat{\mathrm{w}}(1,2) \quad , \tag{4.4}$$

where $\hat{\mathrm{h}}(i)$ are the single-electron Hamiltonians consisting of the kinetic energy operators $\hat{\mathrm{t}}(t)$ and the potential energy operators $\hat{\mathrm{v}}(i)$ describing the effective potential the electrons are moving in,

$$\hat{\mathrm{h}}(i) = \hat{\mathrm{t}}(i) + \hat{\mathrm{v}}(i) \quad , \tag{4.5}$$

and $\hat{\mathrm{w}}(1,2)$ is the interaction operator describing the Coulomb interaction of the 2 active electrons with each other. The time-dependent part $\hat{\mathrm{H}}_I(t)$ describes the interaction of the two active electrons with the time-dependent field of the laser; in dipole approximation and length gauge, it reads

$$\hat{\mathrm{H}}_I(t) = \left(\hat{\vec{\mathrm{r}}}_1 + \hat{\vec{\mathrm{r}}}_2\right)\vec{F}(t) \quad . \tag{4.6}$$

As in the one-electron case, a time-dependent field of the form

$$\vec{F}(t) = \begin{cases} 0 & t < t_i = 0 \\ \vec{e}_z F_0 \sin(\omega t) & 0 \le t \le \frac{\pi}{\omega} \\ 0 & t > t_f = \frac{\pi}{\omega} \end{cases} \quad , \tag{4.7}$$

is considered, which is the same as in eq. (3.1).

---

[2] In the sense that the kinetic energy of the relative motion is large compared to the potential energy of the interaction, please refer to section 4.3.3.4 for a discussion.

4.2.2 Approximate Ground-State of the Two Active Electrons

Similar to section 3.1.1, the two-electron ground state is described in the rigid-rotor approximation, i.e.

$$\hat{\mathrm{H}}_0 \left|g_2\right\rangle \approx E_2 \left|g_2\right\rangle \quad , \tag{4.8}$$

with

$$E_2 \approx -18.98\,\mathrm{eV} \tag{4.9}$$

being the ground state energy (of the 2-electron ground state, i.e. the opposite of the 2-electron ionization potential) according to [7], and

$$\left|g_2\right\rangle = N\left(\left|l_1, u_1\right\rangle \otimes \left|l_2, u_2\right\rangle + (-1)^{s_i} \left|l_2, u_2\right\rangle \otimes \left|l_1, u_1\right\rangle\right) \otimes \left|s_i, m_{s_i}\right\rangle \quad , \tag{4.10}$$

is a 2-particle configuration of the symmetry-adapted rigid-rotor-states $|l, u\rangle$ defined in eq. (2.34), where $|s_i, m_{s_i}\rangle$ is a coupled 2-electron spin state, and N is a normalization factor that can take the values

$$N = \begin{cases} \frac{1}{2} & l_1 = l_2 \text{ and } u_1 = u_2 \\ \frac{1}{\sqrt{2}} & \text{otherwise} \end{cases} \quad . \tag{4.11}$$

As electrons are fermions, the 2-electron state has to obey the fermionic antisymmetry under the exchange of particle labels, i.e. $s = 0$ corresponds to a symmetric spatial configuration and $s = 1$ to an antisymmetric one.

4.2.3 Two Interacting Electrons in Free Space

The solutions of two electrons in free space, i.e. the eigenfunctions and eigenvalues of the Hamiltonian

$$\hat{\mathrm{H}}_0^{\mathrm{free}} = \hat{\mathrm{t}}(1) + \hat{\mathrm{t}}(2) + \hat{\mathrm{w}}(1,2) \quad , \tag{4.12}$$

can be found e.g. in [36]. They fulfill

$$\hat{\mathrm{H}}_0^{\mathrm{free}} \left|\psi_{lm}(\vec{K}, k)\right\rangle = \left(\frac{K^2}{2M} + \frac{k^2}{2\mu}\right) \left|\psi_{lm}(\vec{K}, k)\right\rangle \quad , \tag{4.13}$$

where $M = 2m_e$ is the total mass and $\mu = \frac{m_e}{2}$ is the reduced mass of the 2-electron-system. In COM position-space representation, they read[3]

$$\langle \vec{R}, \vec{r} | \psi_{\mathrm{lm}}(\vec{K}, k)\rangle = \frac{1}{(2\pi)^{3/2}} e^{i\vec{K}\vec{R}} \mathcal{R}_{\mathrm{kl}}(r) Y_{\mathrm{lm}}(\theta, \phi) \left|s_f, m_{s_f}\right\rangle \quad , \tag{4.14}$$

---

[3] Notice that the prefactor slightly differs from the one given in [36], as a different normalization is chosen here.

where $|s_f, m_{s_f}\rangle$ is a 2-electron spin state and

$$\mathcal{R}_{\mathrm{kl}}(r) = \frac{1}{\sqrt{2\pi}} \frac{C_{\mathrm{kl}}}{(2l+1)!} (2kr)^l e^{ikr} F\left(\frac{i}{\mu k} + l + 1, 2l+2, -2ikr\right) \tag{4.15}$$

is the real-valued Coulomb wave function with the normalization factor

$$C_{\mathrm{kl}} = 2ke^{-\frac{\pi}{2}\frac{1}{\mu k}} \left|\Gamma\left(l+1+\frac{i}{\mu k}\right)\right| \quad , \tag{4.16}$$

and $F(a, b, z)$ is the confluent hypergeometric function. Due to the fermionic antisymmetry of the final state under particle exchange, $l + s_f$ has to be even. The normalization is chosen such that

$$\langle \psi_{\mathrm{l'm'}}(\vec{K}', k') | \psi_{\mathrm{lm}}(\vec{K}, k)\rangle = \delta_{ll'}\delta_{mm'}\delta^3(\vec{K} - \vec{K}')\delta(k - k') \quad . \tag{4.17}$$

Notice that although the contribution of the relative motion to the total energy of $|\psi_{\mathrm{lm}}(\vec{K}, k)\rangle$ is denoted as $\frac{k^2}{2\mu}$ here, $|\psi_{\mathrm{lm}}(\vec{K}, k)\rangle$ is not an eigenstate to the relative motion momentum operator $\hat{\vec{\mathrm{p}}} = -i\vec{\nabla}_r$, and therefore k is not a momentum.

4.2.4 Transition Matrix Element in Strong-Field Approximation

In center-of-mass (COM) coordinates, i.e.

$$\vec{R} = \frac{1}{2}(\vec{r}_1 + \vec{r}_2); \quad \vec{r} = \vec{r}_2 - \vec{r}_1, \tag{4.18}$$

the interaction operator $\hat{\mathrm{H}}_I(t)$ can be rewritten as

$$\hat{\mathrm{H}}_I(t) = 2\hat{\vec{\mathrm{R}}}\vec{F} \quad , \tag{4.19}$$

showing that in dipole approximation, the external field only couples to the COM coordinates, which means that the relative motion degrees of freedom are spectators in that sense. Notice that the free-space 2-electron state $|\psi_{\mathrm{lm}}(\vec{K}, k)\rangle$ is just a plane wave in the COM coordinate.

The simultaneous transition matrix element is the matrix element with the unitary time evolution operator

$$\hat{\mathrm{U}}(t, t_0) = \hat{\mathrm{T}} \exp\left(-i\int_{t_0}^{t} \hat{\mathrm{H}}(t')\mathrm{d}t'\right) \quad , \tag{4.20}$$

that describes the probability for the direct transition from the initial state

$$|\psi_i\rangle = |g_2\rangle \tag{4.21}$$

present at time t_i to the final state

$$|\psi_f\rangle = |\psi_{\mathrm{lm}}(\vec{K},k)\rangle \tag{4.22}$$

at time t_f, i.e. the amplitude

$$M_{i\to f} = \langle\psi_f|\hat{\mathrm{U}}(t_f,t_i)|\psi_i\rangle \quad . \tag{4.23}$$

Again using the time propagation in SFA in length gauge and $\Lambda = (0,0)$-partitioning as in eq. (2.130), i.e. neglecting the contribution of the external potential energy operators $\hat{\mathrm{v}}(1)$ and $\hat{\mathrm{v}}(2)$ to the time propagation during the laser pulse, the *ionization* amplitude (leaving out the 0-th order term containing the overlap between $|\psi_i\rangle$ and $|\psi_f\rangle$ again) of this process is

$$M_{\mathrm{ion}}^{\mathrm{SFA}} = -i\int_{t_i}^{t_f} \mathrm{d}t' \;\; \langle\psi_f|\hat{\mathrm{U}}_{\mathrm{free}}(t_f,t')\hat{\mathrm{H}}_I(t')\hat{\vec{\mathrm{r}}}\hat{\mathrm{U}}_0(t',t_i)|\psi_i\rangle \quad . \tag{4.24}$$

Here, $\hat{\mathrm{U}}_0(t,t_i)$ is the time propagation operator corresponding to $\hat{\mathrm{H}}_0$, and the time propagation operator $\hat{\mathrm{U}}_{\mathrm{free}}(t_f,t')$ corresponds to the Hamiltonian

$$\hat{\mathrm{H}}_{\mathrm{free}}(t) = \hat{\mathrm{H}}_0^{\mathrm{free}} + \hat{\mathrm{H}}_I(t) \tag{4.25}$$

$$= \hat{\mathrm{t}}(1) + \hat{\mathrm{t}}(2) + \hat{\mathrm{w}}(1,2) + 2\vec{F}\hat{\vec{\mathrm{R}}} \quad . \tag{4.26}$$

It is important to notice that the *Coulomb interaction* of the two electrons with each other described by $\hat{\mathrm{w}}(1,2)$ is *included* in $\hat{\mathrm{U}}_{\mathrm{free}}(t_f,t')$. Similarly, the final state $|\psi_f\rangle = |\psi_{\mathrm{lm}}(\vec{K},k)\rangle$ is a coupled eigenstate of the Hamiltonian of two free electrons *interacting* with each other. This means that in this formulation, the interaction of both electrons in the continuum is naturally included, which gives rise to interesting correlation effects that will be discussed later on.

As the relative coordinate of the two electrons is not coupled to the field, the interaction only adds an energy term to the propagation, and therefore

$$\langle\psi_{lm}(\vec{K},k)|\,\hat{\mathrm{U}}_{\mathrm{free}}(t_f,t') = e^{iS_{\vec{K}}(t')}\,\langle\psi_{lm}(\vec{K}-2\int_{t_f}^{t'}\mathrm{d}t''\;\vec{F}(t''),k)| \tag{4.27}$$

is a Volkov state in the center-of-mass coordinate, where

$$S_{\vec{K}}(t) = \int_{t_f}^{t}\mathrm{d}t'\;\left[\frac{1}{2M}\left(\vec{K}-2\int_{t_f}^{t'}\mathrm{d}t''\;\vec{F}(t'')\right)^2 + \frac{k^2}{2\mu}\right] \tag{4.28}$$

contains an extra energy term $\frac{k^2}{2\mu}$ for the relative coordinate. On the other hand,

$$\hat{\mathrm{U}}_0(t,t_i)\,|\psi_i\rangle = \hat{\mathrm{U}}_0(t,t_i)\,|g_2\rangle = |g_2^{(I)}(t)\rangle = e^{-iE_2t}\,|g_2\rangle \quad , \tag{4.29}$$

assuming that $|g_2\rangle$ is present at $t_i = 0$, right before the onset of the laser pulse (see eq. (4.1)). This yields

$$M_{\text{ion}}^{\text{SFA}} = -i \int_{t_i}^{t_f} \mathrm{d}t' \;\langle \psi_{lm}(\vec{K} - 2 \int_{t_f}^{t'} \mathrm{d}t''\; \vec{F}(t''), k) | \hat{\mathrm{H}}_I(t') | g_2^{(I)}(t') \rangle \, e^{iS_{\vec{K}}(t')} \tag{4.30}$$

for the simultaneous ionization amplitude in strong-field approximation, length gauge, and $\Lambda = (0,0)$-partitioning.

4.2.5 Solution using the Saddle Point Approximation

The definition

$$D_{lm}(\vec{K}, k) := \langle \psi_{lm}(\vec{K}, k) | \hat{\mathrm{Z}} | g_2 \rangle \tag{4.31}$$

yields

$$M_{\text{ion}}^{\text{SFA}} = -2i \int_{t_i}^{t_f} \mathrm{d}t' \; F(t') D_{lm} \left(\vec{K} - 2 \int_{t_f}^{t'} \mathrm{d}t'' \; \vec{F}(t''), k \right) e^{i\left(S_{\vec{K}}(t') - E_2 t'\right)} \quad . \tag{4.32}$$

As already discussed in section 3.1.3, due to the size of the ground state wave function, the integrand has to be split into slices along the laser direction, i.e. in the simultaneous case along the COM coordinate Z. Again, in complete analogy to section 3.1.3, the decomposition

$$D_{lm}(\vec{K}, k) = \int \mathrm{d}Z \; d_{lm}(Z, \vec{K}_\perp, k) e^{-iK_Z Z} \tag{4.33}$$

is introduced, and defining

$$t_r : \quad 0 = K_Z - 2 \int_{t_f}^{t_r} \mathrm{d}t' F(t') \quad \Longleftrightarrow \quad \cos(\omega t_r) = -1 - \frac{K_Z}{2F_0} \tag{4.34}$$

allows one to write

$$\begin{aligned} M_{\text{ion}}^{\text{SFA}} = -2i \int \mathrm{d}Z \int_{t_i}^{t_f} \mathrm{d}t' \; F(t') d_{lm}(Z, \vec{K}_\perp, k) \\ \cdot \exp\left(i \left(S_{\vec{K}}(t') - E_2 t' + 2 \int_{t_r}^{t'} \mathrm{d}t'' \; F(t'') Z \right) \right) \quad . \end{aligned} \tag{4.35}$$

The inner time integral can then be solved with the saddle point approximation. To this end,

$$g(t, Z) := F(t) d_{lm}(Z, \vec{K}_\perp, k) \tag{4.36}$$

$$f(t, Z) := i \left(S_{\vec{K}}(t) - E_2 t + 2 \int_{t_r}^{t} \mathrm{d}t' \; F(t') Z \right) \tag{4.37}$$

are defined. In the limit

$$\hbar\omega \ll |E_2| \quad , \tag{4.38}$$

which is again met by near infrared lasers already, the prefactor $g(t,Z)$ oscillates slowly in time compared to the exponential part $e^{f(t,Z)}$, such that the saddle point approximation, i.e. the approximate formula

$$\int_{t_i}^{t_f} \mathrm{d}t' g(t',Z) e^{f(t',Z)} \approx \sqrt{\frac{2\pi}{-\eta^2 \left.\frac{\mathrm{d}^2 f(t,Z)}{\mathrm{d}t^2}\right|_{t=t_0}}} \eta(Z) g(t_0,Z) e^{f(t_0,Z)} \tag{4.39}$$

is applicable. Again, $\eta(Z)$ reads

$$\eta(Z) = \exp\left(-\frac{i}{2}\left(\arg\left(\left.\frac{\mathrm{d}^2 f(t,Z)}{\mathrm{d}t^2}\right|_{t=t_0}\right) + \pi\right)\right) \quad , \tag{4.40}$$

and t_0 is the complex position of the saddle point, i.e. it fulfills

$$\left.\frac{\mathrm{d}f(t,Z)}{\mathrm{d}t}\right|_{t=t_0} = 0 \quad . \tag{4.41}$$

The resulting equation for t_0 reads

$$\left(2\int_{t_r}^{t_0} \mathrm{d}t' \; F(t')\right)^2 = -2M\left(-E_2 + \frac{K_\perp^2}{2M} + \frac{k^2}{2\mu} + 2F(t_0)Z\right) \quad , \tag{4.42}$$

which, in the limit

$$\omega|t_0 - t_r| \ll 1 \quad , \tag{4.43}$$

is solved by

$$\omega\left(t_0 - t_r\right) \approx i\omega\frac{\sqrt{2M\left(I_P(K_\perp,k) + 2F(t_r)Z\right)}}{2F(t_r)} = i\gamma_{\mathrm{Kel}}(K_\perp,k,Z) \quad , \tag{4.44}$$

where

$$I_P(K_\perp,k) = -E_2 + \frac{K_\perp^2}{2M} + \frac{k^2}{2\mu} \tag{4.45}$$

is the ionization potential that now not only contains the energy term for the perpendicular kinetic energy in the center-of-mass coordinate, $\frac{K_\perp^2}{2M}$, but also a term for the total energy of the relative motion, $\frac{k^2}{2\mu}$. From, eq. (4.44), it is obvious that the requirement $\omega|t_0 - t_r| \ll 1$ is met in the quasi-static limit, where

$$\gamma_{\mathrm{Kel}}(K_\perp,k,Z) \ll 1 \quad . \tag{4.46}$$

In this limit, one obtains

$$f(t_0, Z) \approx f(t_r, Z = 0) - \frac{2}{3}\frac{\sqrt{2M}}{2F(t_r)}\left(I_P(K_\perp, k) + 2F(t_r)Z\right)^{3/2} \tag{4.47}$$

and

$$\left.\frac{\mathrm{d}^2 f(t, Z)}{\mathrm{d}t^2}\right|_{t=t_0} \approx -\frac{(2F(t_r))^2}{M}\frac{\gamma_{\mathrm{Kel}}(K_\perp, k, Z)}{\omega} + 2iZ\left.\frac{\mathrm{d}F(t)}{\mathrm{d}t}\right|_{t=t_r} \quad , \tag{4.48}$$

as well as

$$g(t_0, Z) \approx F(t_r) d_{lm}(Z, \vec{K}_\perp, k) \quad . \tag{4.49}$$

These solutions are used for the evaluation of the inner time integral in eq. (4.35), using the saddle point approximation as formulated in eq. (4.39):

$$\begin{aligned} M_{\mathrm{ion}}^{\mathrm{SFA}} \approx & -2ie^{f(t_r, Z=0)} F(t_r) \int \mathrm{d}Z\, \eta(Z) \sqrt{\frac{2\pi}{\left|\left.\frac{\mathrm{d}^2 f(t,Z)}{\mathrm{d}t^2}\right|_{t=t_0}\right|}}\, d_{lm}(Z, \vec{K}_\perp, k) \\ & \cdot \exp\left(-\frac{2}{3}\frac{\sqrt{2M}}{2F(t_r)}\left(I_P(K_\perp, k) + 2F(t_r)Z\right)^{3/2}\right) \end{aligned} \tag{4.50}$$

This equation is in complete analogy to eq. (3.18), the corresponding equation for the 1-electron case, with the replacements

$$F(t) \to 2F(t) \tag{4.51}$$

$$m_e \to M \tag{4.52}$$

$$\vec{k} \to \vec{K} \quad . \tag{4.53}$$

This is due to the fact that the simultaneous 2-electron channel can be seen as the transition of a doubly charged 2-electron superparticle with mass M into a plane-wave state in the COM coordinates. The relative motion does not take part in the interaction with the field itself. This however doesn't mean that the relative motion doesn't have a significant influence on the physics of the process, in fact it modifies both the transition dipole moment $d_{lm}(Z, \vec{K}_\perp, k)$ and the ionization potential $I_P(K_\perp, k)$, and the interplay of those two modifications leads to a specific signature in the photoelectron spectrum, as shown later in this chapter in section 4.2.8.2.

The explicit form of the Z-dependent transition dipole moment is

$$\begin{aligned}
d_{lm}(Z,\vec{K}_\perp,k) = {} & \delta_{s_i,s_f}\delta_{m_{s_i},m_{s_f}}\sum_{m_1,m_2} c_{u_1m_1}c_{u_2m_2}\int \mathrm{d}X\int\mathrm{d}Y\int\mathrm{d}^3r & (4.54)\\
& \cdot\frac{1}{(2\pi)^{3/2}}e^{-i(K_XX+K_YY)}\mathcal{R}_{\mathrm{kl}}(r)Y^*_{\mathrm{lm}}(\theta,\phi)\ Z\ \frac{N}{r_0^2}\delta(r_1-r_0)\delta(r_2-r_0)\\
& \cdot\left(Y_{l_1m_1}(\theta_1,\phi_1)Y_{l_2m_2}(\theta_2,\phi_2)+(-1)^{s_i}Y_{l_2m_2}(\theta_1,\phi_1)Y_{l_1m_1}(\theta_2,\phi_2)\right)\\
= {} & \delta_{s_i,s_f}\delta_{m_{s_i},m_{s_f}}N\frac{1+(-1)^{s_i+l}}{(2\pi)^{3/2}r_0^2}\sum_{m_1,m_2}c_{u_1m_1}c_{u_2m_2} & (4.55)\\
& \cdot\int\mathrm{d}X\int\mathrm{d}Y\int\mathrm{d}^3r\ e^{-i(K_XX+K_YY)}\mathcal{R}_{\mathrm{kl}}(r)Y^*_{\mathrm{lm}}(\theta,\phi)\ Z\\
& \cdot\delta(r_1-r_0)\delta(r_2-r_0)Y_{l_1m_1}(\theta_1,\phi_1)Y_{l_2m_2}(\theta_2,\phi_2)\quad ,
\end{aligned}$$

where it was used in the second step that under the exchange of particle labels, the COM coordinates transform according to

$$\vec{R}\rightarrow\vec{R} \tag{4.56}$$

$$\vec{r}\rightarrow-\vec{r}\quad , \tag{4.57}$$

together with the parity relation of the spherical harmonics

$$Y_{lm}\left(-\frac{\vec{r}}{r}\right)=(-1)^l\ Y_{lm}\left(\frac{\vec{r}}{r}\right)\quad . \tag{4.58}$$

This also means that, due to the fermionic antisymmetry of the final state, s_f+l has to be even. Therefore, $(-1)^{s_i+l}=1$, and one can write

$$\begin{aligned}
d_{lm}(Z,\vec{K}_\perp,k) = {} & \delta_{s_i,s_f}\delta_{m_{s_i},m_{s_f}}\frac{2N}{(2\pi)^{3/2}r_0^2}\sum_{m_1,m_2}c_{u_1m_1}c_{u_2m_2} & (4.59)\\
& \cdot\int\mathrm{d}X\int\mathrm{d}Y\int\mathrm{d}^3r\ e^{-i(K_XX+K_YY)}\mathcal{R}_{\mathrm{kl}}(r)Y^*_{\mathrm{lm}}(\theta,\phi)\ Z\\
& \cdot\delta(r_1-r_0)\delta(r_2-r_0)Y_{l_1m_1}(\theta_1,\phi_1)Y_{l_2m_2}(\theta_2,\phi_2)\quad .
\end{aligned}$$

This can be inserted into eq. (4.50) to obtain

$$\begin{aligned}
M^{\mathrm{SFA}}_{\mathrm{ion}} = {} & -2ie^{f(t_r,Z=0)}\delta_{s_i,s_f}\delta_{m_{s_i},m_{s_f}}\frac{2NF(t_r)}{(2\pi)^{3/2}r_0^2}\sum_{m_1,m_2}c_{u_1m_1}c_{u_2m_2}\int\mathrm{d}^3R\int\mathrm{d}^3r\\
& \cdot\delta(r_1-r_0)\ \delta(r_2-r_0)\ \eta(Z)\sqrt{\frac{2\pi}{\left|\left.\frac{\mathrm{d}^2f(t,Z)}{\mathrm{d}t^2}\right|_{t=t_0}\right|}}e^{-i(K_XX+K_YY)}\mathcal{R}_{\mathrm{kl}}(r)\ Z\\
& \cdot Y^*_{\mathrm{lm}}(\theta,\phi)Y_{l_1m_1}(\theta_1,\phi_1)Y_{l_2m_2}(\theta_2,\phi_2)\\
& \cdot\exp\left(-\frac{2}{3}\frac{\sqrt{2M}}{2F(t_r)}\left(I_P(K_\perp,k)+2F(t_r)Z\right)^{3/2}\right)\quad . & (4.60)
\end{aligned}$$

In order to proceed, the spherical harmonics $Y^*_{\mathrm{lm}}(\theta,\phi)$ have to be shifted from the COM frame to the absolute frame. This can be done using the decomposition [37]

$$Y_{lm}\left(\frac{\vec{r_2}-\vec{r_1}}{|\vec{r_2}-\vec{r_1}|}\right) = \sum_{l'=0}^{l} \sum_{m'=\mu_{\min}(l,m,l')}^{\mu_{\max}(l,m,l')} P(l,m,l',m') \frac{r_1^{l'} r_2^{l-l'}}{r^l} \cdot Y_{l'm'}\left(\frac{\vec{r_1}}{r_1}\right) Y_{l-l',\ m-m'}\left(\frac{\vec{r_2}}{r_2}\right) \tag{4.61}$$

with

$$P(l,m,l',m') = (-1)^{l'} \sqrt{\frac{4\pi(2l+1)}{(2l-2l'+1)(2l'+1)}} \cdot \frac{1}{\sqrt{(l-l'-m+m')!(l-l'+m-m')!}} \sqrt{\frac{(l-m)!(l+m)!}{(l'-m')!(l'+m')!}} \tag{4.62}$$

and the summation boundaries

$$\mu_{\min}(l,m,l') = \max(-l', -(l-l')+m) \tag{4.63}$$
$$\mu_{\max}(l,m,l') = \min(l', (l-l')+m) \quad , \tag{4.64}$$

that are explicitly given in [38]. Then, the radial coordinates in the absolute frame can easily be integrated over, which leads to

$$\begin{aligned} M^{\mathrm{SFA}}_{\mathrm{ion}} = & -2ie^{f(t_r,Z=0)} \delta_{s_i,s_f} \delta_{m_{s_i},m_{s_f}} \frac{2NF(t_r)r_0^2}{(2\pi)^{3/2}} \sum_{m_1,m_2,l',m'} c_{u_1m_1} c_{u_2m_2} P(l,m,l',m') \\ & \cdot \int \mathrm{d}\Omega_1 \int \mathrm{d}\Omega_2\ \eta(Z) \sqrt{\frac{2\pi}{\left|\left.\frac{\mathrm{d}^2 f(t,Z)}{\mathrm{d}t^2}\right|_{t=t_0}\right|}} e^{-i(K_X X + K_Y Y)} \left(\frac{r_0}{r}\right)^l \mathcal{R}_{\mathrm{kl}}(r)\ Z \\ & \cdot Y^*_{l'm'}(\theta_1,\phi_1)\, Y^*_{l-l',\ m-m'}(\theta_2,\phi_2)\, Y_{l_1m_1}(\theta_1,\phi_1) Y_{l_2m_2}(\theta_2,\phi_2) \\ & \cdot \exp\left.\left(-\frac{2}{3}\frac{\sqrt{2M}}{2F(t_r)} \left(I_P(K_\perp,k) + 2F(t_r)Z\right)^{3/2}\right)\right|_{r_1=r_2=r_0} \quad , \end{aligned} \tag{4.65}$$

where all remaining coordinates have to be understood as being confined to $r_1 = r_2 = r_0$ in this expression, e.g. the exponential takes the form

$$\exp\left(-\frac{2}{3}\frac{\sqrt{2M}}{2F(t_r)} \left[I_P(K_\perp,k) + F(t_r) r_0 \left(\cos\theta_1 + \cos\theta_2\right)\right]^{3/2}\right) \quad . \tag{4.66}$$

Analogously to the single electron case in section 3.1.3, it can be assumed that due to the dominance of $Z \approx -r_0$ in the integrand, the pre-exponential but Z-dependent expressions can be evaluated for $Z = -r_0$. Similarly, together with the confinement of $\vec{r_1}$ and $\vec{r_2}$ to spheres of radius r_0 and the exponential suppression for $\vec{K}_\perp \neq 0$, it can be assumed that

$$e^{-i(K_X X + K_Y Y)} \approx 1 \tag{4.67}$$

for all significant contributions in the distribution of $K_\perp$, resulting in

$$\begin{aligned} M_{\text{ion}}^{\text{SFA}} \approx & -2ie^{f(t_r,Z=0)}\delta_{s_i,s_f}\delta_{m_{s_i},m_{s_f}}\frac{2NF(t_r)r_0^2}{(2\pi)^{3/2}}\eta(Z=-r_0)\sqrt{\frac{2\pi}{\left|\left.\frac{\mathrm{d}^2 f(t,Z=-r_0)}{\mathrm{d}t^2}\right|_{t=t_0}\right|}} \\ & \cdot \sum_{m_1,m_2,l',m'} c_{u_1m_1}c_{u_2m_2}P(l,m,l',m')\int \mathrm{d}\Omega_1 \int \mathrm{d}\Omega_2 \ \left(\frac{r_0}{r}\right)^l \mathcal{R}_{\text{kl}}(r)\ Z \\ & \quad \cdot Y^*_{l'm'}\left(\theta_1,\phi_1\right) Y^*_{l-l',\ m-m'}\left(\theta_2,\phi_2\right) Y_{l_1m_1}(\theta_1,\phi_1) Y_{l_2m_2}(\theta_2,\phi_2) \\ & \quad \cdot \exp\left(-\frac{2}{3}\frac{\sqrt{2M}}{2F(t_r)}\left(I_P(K_\perp,k)+2F(t_r)Z\right)^{3/2}\right)\Bigg|_{r_1=r_2=r_0} \quad . \end{aligned} \tag{4.68}$$

To allow for efficient computation, it is helpful to introduce an approximation of the radial Coulomb wave function $\mathcal{R}_{\text{kl}}(r)$ as well. It will be seen and discussed later on in this chapter that due to the interplay of the term $e^{-\frac{\pi}{2}\frac{1}{\mu k}}$ in C_{kl} on the one side and the energy term in the exponential on the other side, the distributions in k created in this work are sharply peaked, while this peak is around $k_{\text{peak}} \approx 0.55$ for the field strengths used (see e.g. fig. 4.7). For simplicity, this value is assumed in the following derivation of an effective separation $\bar{r}$.

While for larger separations r, the radial Coulomb wave function is larger (see also fig. 4.4), a large separation r corresponds to $Z \approx 0$. Small values of r, on the other hand, can correspond to $Z \approx -1$, and therefore they are favored by the exponential term, which means that there is a competition between both effects. To get an estimate for the most significant contributions of r in the integrand, one can calculate the "effective value" of r neglecting the spherical harmonics and the prefactor Z, i.e.

$$\bar{r} = \frac{\int \mathrm{d}\Omega_1 \int \mathrm{d}\Omega_2 \ r \ \ w(r,Z)|_{r_1=r_2=r_0}}{\int \mathrm{d}\Omega_1 \int \mathrm{d}\Omega_2 \ \ w(r,Z)|_{r_1=r_2=r_0}} \quad , \tag{4.69}$$

where

$$w(r,Z) = \frac{\left|\mathcal{R}_{k_{\text{peak}},l}(r)\right|}{r^l}\exp\left(-\frac{2}{3}\frac{\sqrt{2M}}{2F(t_r)}\left[I_P(K_\perp=0,k_{\text{peak}})+2F(t_r)Z\right]^{3/2}\right) \quad . \tag{4.70}$$

The coordinates r and Z are again confined to the spheres $r_1 = r_2 = r_0$, such that e.g.

$$r = r_0 \sqrt{\begin{aligned}(c_2 - c_1)^2 + \left(\sqrt{1-c_2^2}\cos(\phi_2) - \sqrt{1-c_1^2}\cos(\phi_1)\right)^2 \\ + \left(\sqrt{1-c_2^2}\sin(\phi_2) - \sqrt{1-c_1^2}\sin(\phi_1)\right)^2\end{aligned}}\,, \tag{4.71}$$

where $c_i = \cos(\theta_i)$. Fig. 4.3 shows the value of $\bar{r}$ as a function of the field strength at the saddle point $F(t_r)$ for different l. On the other hand, it can be seen from fig. 4.4 that the value of the *strictly real-valued* term[4]

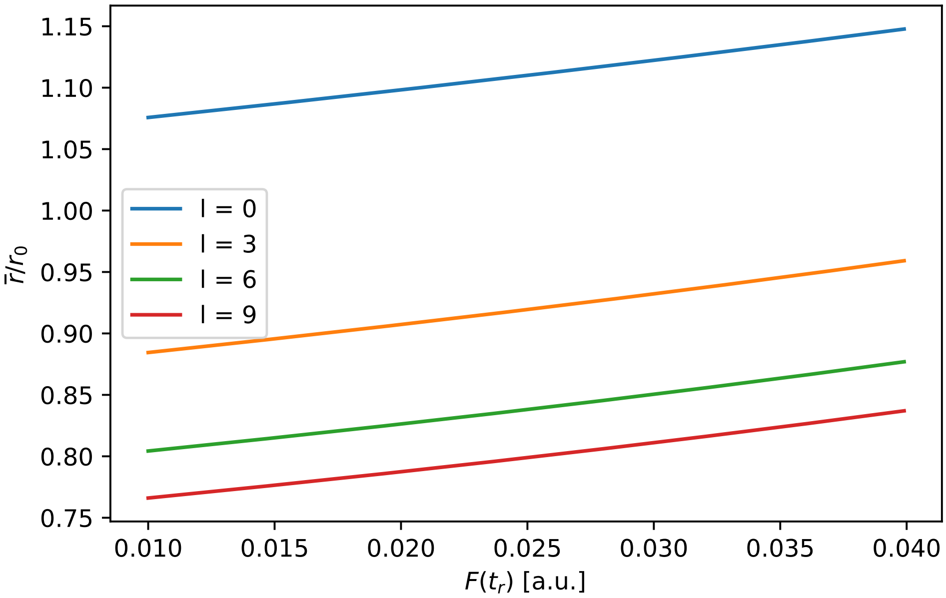

FIGURE 4.3: The effective separation $\bar{r}$ (see eq. 4.69) for different final angular momentum quantum numbers l between 0 and 9 as specified in the legend, and as a function of the field strength at the saddle point $F(t_r)$ (see eq. (4.34)).

$$h(k_{\text{peak}}, l, r) = e^{ik_{\text{perp}}r} F\left(\frac{i}{\mu k_{\text{peak}}} + l + 1, 2l + 2, -2ik_{\text{peak}}r\right) \tag{4.72}$$

is only slightly dependent on r around the values of $\bar{r}$ shown in fig. 4.3. It can also be seen that for the present parameters, there is no oscillation visible for $0 < r < 2r_0$. To simplify the calculation, an effective $\bar{r}$ is therefore used to

---

[4] The implementation of the confluent hypergeometric function for complex arguments is taken from [39].

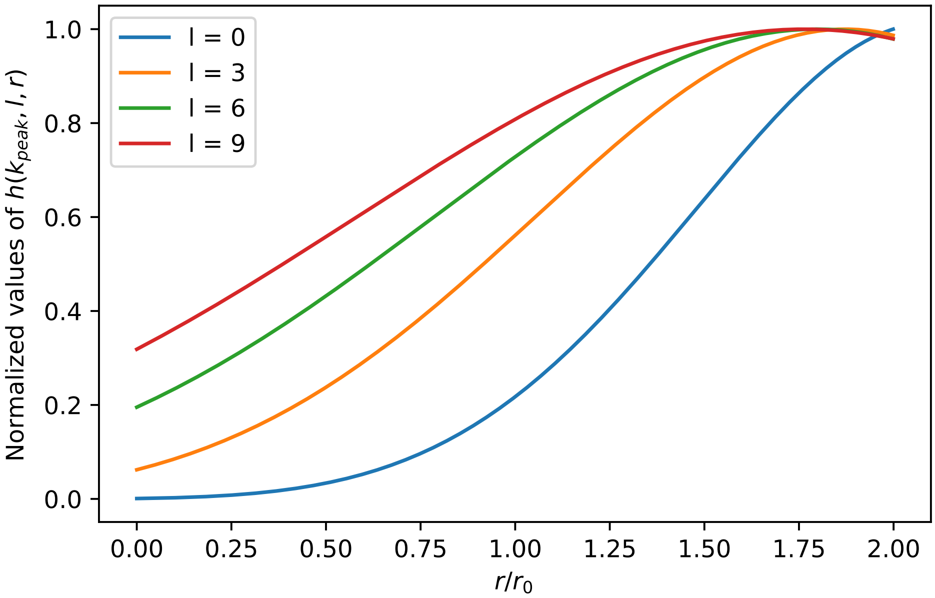

FIGURE 4.4: Values of $h(k_{\text{peak}}, l, r)$ (see eq. (4.72)) shown for the entire interval $0 < r < 2r_0$, normalized to the respective maximum in this interval. The function is shown for different final angular momentum quantum numbers l ranging from 0 to 9 as specified in the legend. These are the same values as used in fig. 4.3.

proceed. More precisely, the approximation

$$e^{ikr} F\left(\frac{i}{\mu k} + l + 1, 2l + 2, -2ikr\right) \approx \\ e^{ikr_0} F\left(\frac{i}{\mu k} + l + 1, 2l + 2, -2ikr_0\right) := C_{kl}^{(F)} \tag{4.73}$$

is used. The value $\bar{r} \approx r_0$ is a little bit too large for larger final angular momentum quantum numbers l, but on the other hand the difference of $h(k_{\text{peak}}, l, \bar{r})$ and $h(k_{\text{peak}}, l, r_0)$ is much smaller in this case. To keep things simple, a variable value of $\bar{r}$ that depends on l and $F(t_r)$ is not used here.

This "effective distance approximation" is rather bold, and it can only serve as an estimate for the order of magnitude of the result. Future work might improve on this step; suggestions for possible starting points are given in the discussion in section 5.2.5.

By inserting the approximation in eq. (4.73) into eq. (4.68), one obtains

$$\begin{aligned} M_{\text{ion}}^{\text{SFA}} \approx & -2ie^{f(t_r,Z=0)}\delta_{s_i,s_f}\delta_{m_{s_i},m_{s_f}}\frac{2NF(t_r)r_0^2}{(2\pi)^2}\frac{C_{kl}C_{kl}^{(F)}(2kr_0)^l}{(2l+1)!}\eta(Z=-r_0) \\ & \cdot\sqrt{\frac{2\pi}{\left|\left.\frac{\mathrm{d}^2 f(t,Z=-r_0)}{\mathrm{d}t^2}\right|_{t=t_0}\right|}}\sum_{m_1,m_2,l',m'} c_{u_1m_1}c_{u_2m_2}P(l,m,l',m')\int\mathrm{d}\Omega_1\int\mathrm{d}\Omega_2 \\ & \cdot Z\;Y_{l'm'}^{*}(\theta_1,\phi_1)\,Y_{l-l',\;m-m'}^{*}(\theta_2,\phi_2)\,Y_{l_1m_1}(\theta_1,\phi_1)Y_{l_1m_1}(\theta_1,\phi_1) \\ & \cdot\exp\left.\left(-\frac{2}{3}\frac{\sqrt{2M}}{2F(t_r)}\left(I_P(K_\perp,k)+2F(t_r)Z\right)^{3/2}\right)\right|_{r_1=r_2=r_0} \quad . \end{aligned} \tag{4.74}$$

Small values of k in the final distribution correspond to a low interaction energy of both electrons in the continuum, and therefore to electrons that are far apart from each other. Such a state has a small overlap with the initial state that is confined in size, which is reflected by the term

$$C_{kl}C_{kl}^{(F)}(2kr_0)^l \quad . \tag{4.75}$$

Larger values of k are favored from this point of view. However, large values of k increase the ionization potential, which in turn leads to an exponential suppression. There is a sweet spot value of k between both effects, that shows up as a sharp peak in the differential ionization probability. This is discussed in more detail in section 4.2.8.2.

Now, the spherical harmonics are the only part of the integrand that is still dependent on the angles ϕ_1 and ϕ_2. Therefore, they can be integrated over, which leads to the selection rule $m = m_1 + m_2$:

$$\begin{aligned} M_{\text{ion}}^{\text{SFA}} \approx & -ie^{f(t_r,Z=0)}\delta_{s_i,s_f}\delta_{m_{s_i},m_{s_f}}\frac{2NF(t_r)r_0^3}{(2\pi)^2}\frac{C_{kl}C_{kl}^{(F)}(2kr_0)^l}{(2l+1)!}\eta(Z=-r_0) \qquad (4.76) \\ & \cdot\sqrt{\frac{2\pi}{\left|\left.\frac{\mathrm{d}^2 f(t,Z=-r_0)}{\mathrm{d}t^2}\right|_{t=t_0}\right|}}\sum_{m_1,m_2,l'}\delta_{m_1+m_2,m}\;c_{u_1m_1}c_{u_2m_2}\;P(l,m_1+m_2,l',m_1) \\ & \qquad\qquad\qquad\qquad \cdot N_{l'm_1}N_{l-l',m_2}N_{l_1m_1}N_{l_2m_2} \\ & \cdot\int_{-1}^{1}\mathrm{d}x_1\int_{-1}^{1}\mathrm{d}x_2\;(x_1+x_2)\;P_{l',|m_1|}(x_1)P_{l-l',|m_2|}(x_2)P_{l_1,|m_1|}(x_1)P_{l_2,|m_2|}(x_2) \\ & \qquad\qquad \cdot\exp\left(-\frac{2}{3}\frac{\sqrt{2M}}{2F(t_r)}\left(I_P(K_\perp,k)+(x_1+x_2)F(t_r)r_0\right)^{3/2}\right) \end{aligned}$$

Here, P_{lm} are the associated Legendre polynomials as defined in eq. (2.30) and N_{lm} are the normalization factors of the spherical harmonics in the convention defined in eq. (2.31).

4.2.6 Numerical Implementation

To sum it up, the ionization matrix element from a symmetry-adapted state described by the quantum numbers u_1 and u_2 is a linear combination

$$M_{\text{ion}}^{\text{SFA}} = \delta_{s_i,s_f}\delta_{m_{s_i},m_{s_f}} \sum_{m_1,\ m_2} c_{u_1 m_1} c_{u_2 m_2}\ M_{\text{ion}}^{\text{SFA}}(m_1, m_2) \tag{4.77}$$

of the ionization matrix elements $M_{\text{ion}}^{\text{SFA}}(m_1, m_2)$ of the non-adapted rigid-rotor configuration described by (m_1, m_2), that read

$$\begin{aligned} M_{\text{ion}}^{\text{SFA}}(m_1, m_2) =& \delta_{m_1+m_2,m}\ (-i) e^{f(t_r, Z=0)} \eta(-r_0) \\ & \cdot \frac{2NF(t_r) r_0^3}{(2\pi)^2} \frac{C_{kl} C_{kl}^{(F)} (2kr_0)^l}{(2l+1)!} \sqrt{\frac{2\pi}{\left| \left. \frac{\mathrm{d}^2 f(t, Z=-r_0)}{\mathrm{d}t^2} \right|_{t=t_0} \right|}} \\ & \cdot \sum_{l'} \quad P(l, m_1+m_2, l', m_1) N_{l'm_1} N_{l-l',m_2} N_{l_1 m_1} N_{l_2 m_2} \\ \cdot \int_{-1}^{1} \mathrm{d}x_1 \int_{-1}^{1} & \mathrm{d}x_2\ (x_1+x_2)\ P_{l',|m_1|}(x_1) P_{l-l',|m_2|}(x_2) P_{l_1,|m_1|}(x_1) P_{l_2,|m_2|}(x_2) \\ & \cdot \exp\left(-\frac{2}{3} \frac{\sqrt{2M}}{2F(t_r)} \left(I_P(K_\perp, k) + (x_1+x_2) F(t_r) r_0\right)^{3/2} \right) \quad . \end{aligned} \tag{4.78}$$

The inner part of the expression, i.e.

$$\begin{aligned} \sum_{l'} \quad & P(l, m_1+m_2, l', m_1) N_{l'm_1} N_{l-l',m_2} N_{l_1 m_1} N_{l_2 m_2} \\ & \cdot \int_{-1}^{1} \mathrm{d}x_1 \int_{-1}^{1} \mathrm{d}x_2\ (x_1+x_2)\ P_{l',|m_1|}(x_1) P_{l-l',|m_2|}(x_2) P_{l_1,|m_1|}(x_1) P_{l_2,|m_2|}(x_2) \\ & \qquad \cdot \exp\left(-\frac{2}{3} \frac{\sqrt{2M}}{2F(t_r)} \left(I_P(K_\perp, k) + (x_1+x_2) F(t_r) r_0\right)^{3/2} \right) \end{aligned} \tag{4.79}$$

has to be evaluated numerically. This can be done using a standard integration routine like the `integrate.quad` function contained in the `scipy` library [35] for `python`, which was used in this thesis.

4.2.6.1 Parallelization and Buffering

For a specific set of laser parameters specified by ω and F_0, the integral in eq. (4.79) has to be calculated for all possible combinations of l, m_1, m_2, I_P, and K_Z, which directly corresponds to t_r according to eq. (4.34). Hence, the integral has to be calculated for a 5-dimensional parameter space, of which 2 dimensions are continuous and 3 are discrete. This means that there is both the possibility and the need to parallelize the evaluation.

To this end, the calculation is done with a set of `python` workers running in parallel on a cluster. Each worker calculates eq. (4.79) for all combinations of l', m_1, m_2, and $I_P(K_\perp, k)$, but only for a single K_Z. After the calculation, the results are stored as a binary file on a common disk all workers have access to. Each worker loops over all K_Z, and, before starting a calculation, it checks if the file for the current K_Z already exists on the disk. If it does, it jumps to the next K_Z, and so on. As soon as a worker starts a calculation, it saves a dummy file on the disk so that other workers won't redo the same calculation. This setup ensures that an arbitrary number of workers can be deployed independently and asynchronously on different machines, increasing the parallelization with increasing number of workers. For example, if the number of workers is equal to the number of different K_Z, the entire calculation takes only as long as a single process. The organizational overhead is limited to checking the file existence prior to starting the calculation, which is negligible.

For example, consider a single worker running a calculation for fixed K_Z, for 200 values of $I_P(K_\perp, k)$, combined with all l up to a maximum l of $l_{\text{max}} = 12$ and all m_1 and m_2 that fulfill $-l_i \leq m_i \leq l_i$, where $l_1 = l_2 = 5$. Notice that many of the combinations are zero, as

$$|m1 + m2| = |m| \leq l \leq l_{\text{max}} \tag{4.80}$$

has to be fulfilled. In the implementation used, this calculation takes around 8 h on a single kernel of an Intel® Xeon® ES-2670 (2.6 GHz) processor. The RAM requirements are on the order of 100MB, which is negligible for a typical computer architecture, where one can expect around 2GB of RAM per kernel. In the maximally parallelized version, the entire calculation can therefore be done in around 8 h as well. The number of workers required in this case is equal to the number of K_Z the final distribution should be evaluated for. For the calculations presented in this work, around 50 workers have been used in parallel to sample the final distribution in around 8 hours.

The results for the inner integral in eq. (4.79) are saved on a hard drive, as described. For the described example, the results for the entire momentum space take around 2 GB of disk space. When performing analyses, the multiplication with the prefactor in eq. (4.78) can be done in real time, as well as the summation over m_1 and m_2 when calculating the symmetry-adapted ionization matrix elements according to eq. (4.77).

4.2.7 Differential Ionization Probability

In an attempt to make the notation more readable, the dependency of $M_{\text{ion}}^{\text{SFA}}$ on the quantum numbers of both the initial state and the final state was not stated explicitly during its derivation. In the following however, the convention

$$M_{\text{ion}}^{\text{SFA}}(\vec{K}, k, l, m) \approx \langle \psi_{\text{lm}}(\vec{K}, k) | \hat{\mathrm{U}}(t_f = \pi/\omega, t_i = 0) | g_2 \rangle \tag{4.81}$$

is used. With this, the ionized part of the wave function after the pulse can be written as

$$|\psi_{\text{ion}}^{\text{Sim}}\rangle = \sum_{lm} \int \mathrm{d}^3K \int \mathrm{d}k \; M_{\text{ion}}^{\text{SFA}}(\vec{K}, k, l, m) \, |\psi_{\text{lm}}(\vec{K}, k)\rangle \quad , \tag{4.82}$$

and the total ionization is

$$P_{\text{ion}}^{\text{Sim}} = \langle \psi_{\text{ion}} | \psi_{\text{ion}} \rangle \tag{4.83}$$

$$= \sum_{lm} \int \mathrm{d}^3K \int \mathrm{d}k \, \left| M_{\text{ion}}^{\text{SFA}}(\vec{K}, k, l, m) \right|^2 \quad , \tag{4.84}$$

using the normalization relation in eq. (4.17). Notice that due to the fermionic antisymmetry of the final state, the sum over l only runs over those l that fulfill the requirement that $l + s_f$ is even.

Because the problem formulation and therefore the result $M_{\text{ion}}^{\text{SFA}}(\vec{K}, k, l, m)$ is cylindrically symmetric in the K_X-K_Y-plane, this can be reformulated as

$$P_{\text{ion}}^{\text{Sim}} = \int \mathrm{d}K_Z \int \mathrm{d}K_\perp \int \mathrm{d}k \, \frac{\mathrm{d}^3 P_{\text{ion}}^{\text{Sim}}}{\mathrm{d}K_Z \mathrm{d}K_\perp \mathrm{d}k} \quad , \tag{4.85}$$

with the differential ionization probability (momentum distribution)

$$\frac{\mathrm{d}^3 P_{\text{ion}}^{\text{Sim}}}{\mathrm{d}K_Z \mathrm{d}K_\perp \mathrm{d}k} = 2\pi K_\perp \sum_{lm} \left| M_{\text{ion}}^{\text{SFA}}(\vec{K}, k, l, m) \right|^2 \quad . \tag{4.86}$$

4.2.8 Results

Using eq. (4.86), momentum distributions can be plotted in the 3 dimensions K_Z, $K_\perp$ and k. As pointed out in section 2.1.1.2.1, within the rigid-rotor model, the HOMO level is filled with 10 electrons in the state $|l, u\rangle$, where $l = 5$ and u can be one of the 5 degenerate symmetry-adapted states θ, ϵ, ξ, η, and ζ. As already mentioned, the ionization potential for double ionization of C_{60} is assumed to be $E_2 \approx 18.98\,\text{eV}$ [7]. This is now used to calculate the differential ionization probabilities using eq. (4.86), where the ionization matrix elements are calculated according to eqs. (4.77) and (4.78).

4.2.8.1 COM coordinates

For a laser wavelength of $\lambda = 8000\,\text{nm}$, which corresponds to a pulse duration (duration of the half-cycle) of 13 fs, and a maximum field of 0.04 a.u., the differential distribution in K_Z and $K_\perp$

$$\frac{\mathrm{d}^2 P_{\text{ion}}^{\text{Sim}}}{\mathrm{d}K_Z \mathrm{d}K_\perp} = \int \mathrm{d}k \frac{\mathrm{d}^3 P_{\text{ion}}^{\text{Sim}}}{\mathrm{d}K_Z \mathrm{d}K_\perp \mathrm{d}k} \tag{4.87}$$

is shown in fig. 4.5. Here, $u_1 = u_2 = \zeta$ is chosen as the initial state, therefore, the spin symmetry has to be singlet ($s_i = 0$). All l-contributions up to $l_{\text{max}} = 12$ have been considered. The distribution is similar to the on in fig. 3.4, which is not surprising considering that the ionization process can be seen as the ejection of a doubly-charged quasi particle at the COM, however, the 2-electron character can be clearly seen in the absolute value of the distribution, which is much smaller here. This is due to an increased ionization potential in the exponent in eq. (3.44) compared to eq. (4.66), and additionally due to Coulomb blockade effects, as shown in the following section.

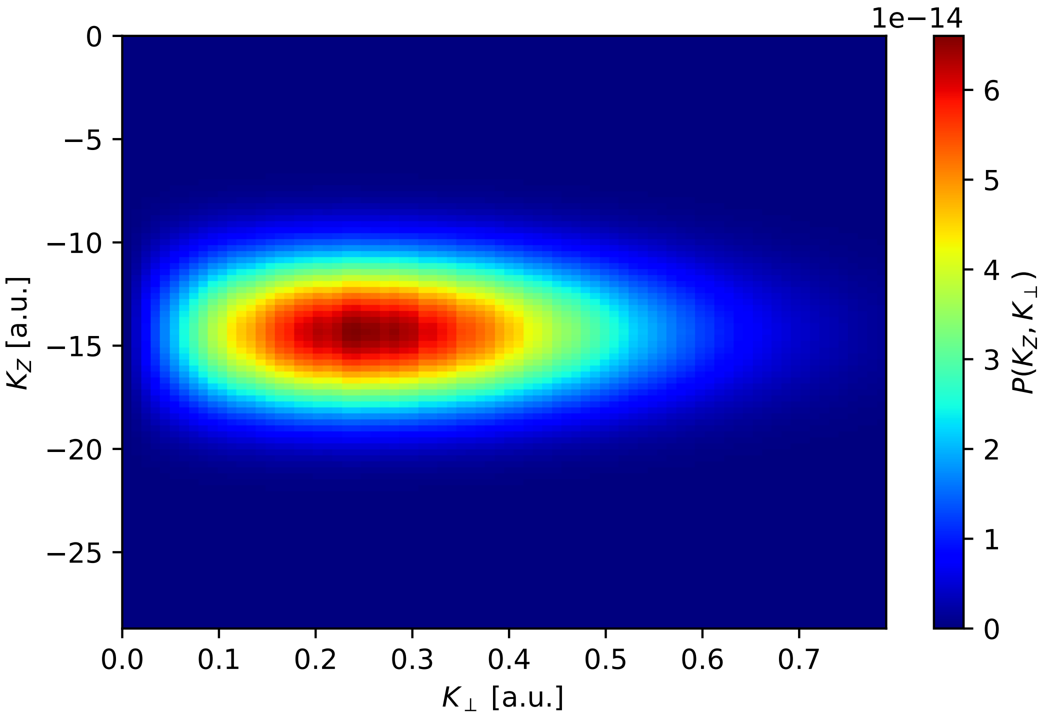

FIGURE 4.5: Momentum distribution $P(K_Z, K_\perp) := \frac{\mathrm{d}^2 P_{\text{ion}}^{\text{Sim}}}{\mathrm{d}K_Z \mathrm{d}K_\perp}$ after simultaneous double ionization. The results are calculated for the initial configuration $l_1 = l_2 = 5$, $u_1 = u_2 = \zeta$, and $s_i = 0$, with the laser parameters $F_0 = 0.04\,\text{a.u.}$ and $\lambda = 8000\,\text{nm}$. The Z-momenta are symmetrical around $-2F_0/\omega$, corresponding to the real part of the saddle point being exactly at the maximum of the laser pulse. For the final state, all symmetry-allowed l-contributions up to $l_{\max} = 12$ have been considered.

4.2.8.2 Relative Coordinates

For the same initial state and laser parameters as in section 4.2.8.1, the momentum distribution

$$\frac{\mathrm{d}^2 P_{\text{ion}}^{\text{Sim}}}{\mathrm{d}K_\perp \mathrm{d}k} = \int \mathrm{d}K_Z \frac{\mathrm{d}^3 P_{\text{ion}}^{\text{Sim}}}{\mathrm{d}K_Z \mathrm{d}K_\perp \mathrm{d}k} \tag{4.88}$$

is plotted for the relative coordinate in fig. 4.6.

The exponential term

$$\exp\left(-\frac{2}{3}\frac{\sqrt{2M}}{2F(t_r)}\left(I_P(K_\perp, k) + (x_1 + x_2)F(t_r)r_0\right)^{3/2}\right) \tag{4.89}$$

in the final result (see eq. (4.76)) is much larger for smaller ionization potentials corresponding to smaller values of k. This can be seen from fig. 4.7, where

$$f_{\text{energy}}(k) := \exp\left(-\frac{2}{3}\frac{\sqrt{2M}}{2F_0}\left(I_P(K_\perp = 0, k) - 2F(t_r)r_0\right)^{3/2}\right) \tag{4.90}$$

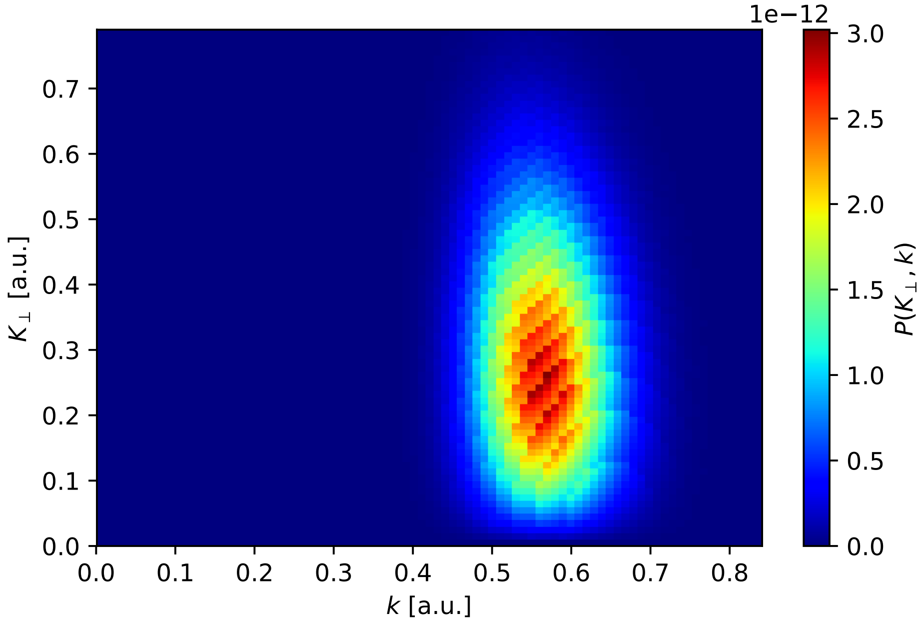

FIGURE 4.6: Momentum distribution $P(K_\perp, k) := \frac{\mathrm{d}^2 P_{\mathrm{ion}}^{\mathrm{Sim}}}{\mathrm{d}K_\perp \mathrm{d}k}$ after simultaneous double ionization. The results are calculated for the initial configuration $l_1 = l_2 = 5$, $u_1 = u_2 = \zeta$, and $s_i = 0$, with the laser parameters $F_0 = 0.04\,\mathrm{a.u.}$ and $\lambda = 8000\,\mathrm{nm}$. In k direction, the distribution is determined by an interplay between the transition dipole moment suppressing low momenta and the tunneling exponential suppressing large momenta. For the final state, all symmetry-allowed l-contributions up to $l_{\max} = 12$ have been considered.

is shown for $F_0 = 0.04\,\mathrm{a.u.}$, i.e. for the peak field strength used for fig. 4.6. The physical meaning of $f_{\mathrm{energy}}(k)$ is that larger values of k are exponentially suppressed because final states with larger values of k have larger energy. Naively, one might assume that therefore the peak of the distribution should be at $k \approx 0$, slightly shifted from 0 due to a polynomial prefactor accounting for the phase space volume.

However, this assumption only holds if no Coulomb interaction in the final state is included. Such a model is discussed later in this chapter as a simple man's model for sequential ionization (see fig. 4.9a). In the present model however, the interaction in the final state is included by using the fully correlated Coulomb wave function as the final state. The remainder of the Coulomb wave function in the final result in eq. (4.76) is the term

$$\begin{aligned} f_{\mathrm{overlap}}(k) &:= C_{kl} C_{kl}^{(F)} (2kr_0)^l \qquad (4.91) \\ &= 2ke^{-\frac{\pi}{2}\frac{1}{\mu k}} \left| \Gamma\left(l + 1 + \frac{i}{\mu k}\right)\right| (2kr_0)^l \\ &\quad \cdot e^{ikr_0} F\left(\frac{i}{\mu k} + l + 1, 2l + 2, -2ikr_0\right) \quad . \end{aligned}$$

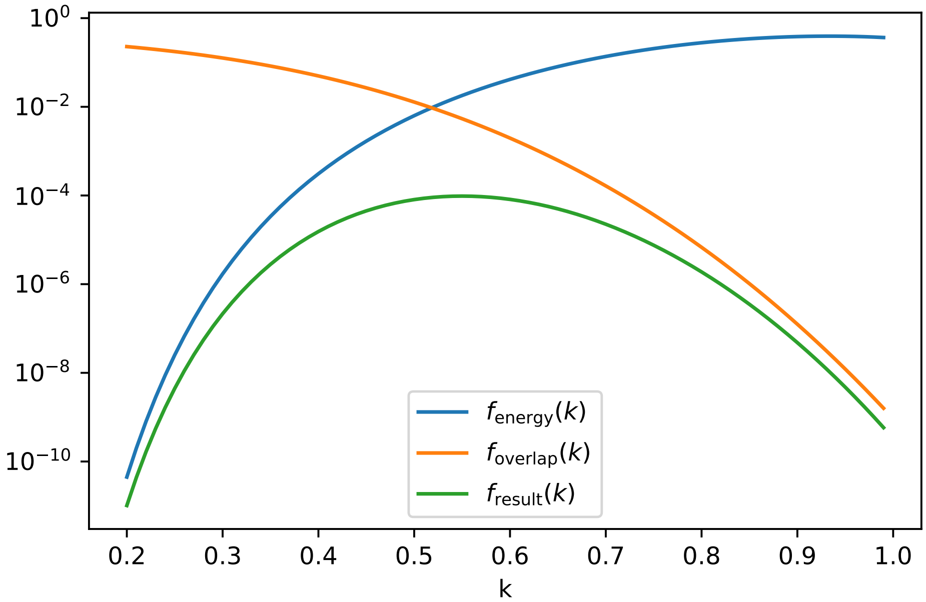

FIGURE 4.7: The terms $f_{\text{energy}}(k)$ (eq. (4.90)), $f_{\text{overlap}}(k)$ (eq. (4.91)), and their product $f_{\text{result}}(k)$ as a function of k for $F_0 = 0.04\,\text{a.u.}$ and $l = 0$. The product has its peak at $k \approx 0.55$, which is in approximate agreement with the peak of the full distribution shown in fig. 4.6.

This term exponentially decreases for $k \to 0$, as can also be seen from fig. 4.7, where it is shown for $l = 0$. The physical meaning of $f_{\text{overlap}}(k)$ is the following: Small k correspond to a low energy E_{rel} of the relative motion according to the formula

$$k = \sqrt{2\mu E_{\text{rel}}} \quad , \tag{4.92}$$

which directly follows from eq. (4.13). Because E_{rel} contains the sum of the kinetic energy of the relative motion of both electrons and their interaction energy, it is always positive and only approaches 0 if the electrons are separated infinitely far from each other. Hence, $k \to 0$ corresponds to both electrons being separated infinitely far immediately after ionization. On the other hand, the initial ground state is of finite size, which is reflected by the effective separation $\bar{r} \approx r_0$ of both electrons during ionization. In the limit $k \to 0$, the overlap between initial and final state therefore approaches 0. Hence, ionization is suppressed in this limit as well.

The competition between low energy of the final state ($f_{\text{energy}}(k)$) and large overlap with the initial state ($f_{\text{overlap}}(k)$) has a sweet spot where the ionization reaches its maximum. This can be seen as the peak in k in fig. 4.6. The position of this maximum can be estimated as the maximum of the product

$$f_{\text{result}}(k) := f_{\text{energy}}(k) f_{\text{overlap}}(k) \tag{4.93}$$

that is also shown in fig. 4.7. The position of the maximum of $f_{\text{result}}(k)$ coincides approximately with the one in fig. 4.6, smaller deviations are due to different contributions in the parameters Z, l, or K_Z to the final distribution.

The fact that this maximum's position is shifted towards larger values of k and that its value is lower compared to the uncorrelated case (fig. 4.9a to be discussed later in this work), is a consequence of the Coulomb blockade. The final momentum distribution for simultaneous double ionization therefore exhibits clear signatures of the Coulomb blockade effect. The strength of this effect decreases with increasing effective size of the molecule. For a larger molecule of the same geometry, the effective separation $\bar{r}$ would be larger, and therefore the overlap ($f_{\text{overlap}}(k)$) would increase for fixed values of k. This would shift the position of the maximum towards lower k and would increase the value of the maximum, indicating a weaker Coulomb blockade effect.

4.2.8.3 Convergence in l_{max}

As the differential ionization probabilities presented in this section are infinite sums of the contributions for different angular momentum quantum numbers l, they have been truncated to $l \leq l_{\text{max}}$. The parameter l_{max} has to be checked numerically for convergence. In fig. 4.8, the quantity

$$\frac{\Delta P(K_\perp, k)}{P(K_\perp, k)} := \left| \frac{\frac{\mathrm{d}^2 P_{\text{ion}}^{\text{Sim}}(l_{\text{max}}=10)}{\mathrm{d}K_\perp \mathrm{d}k} - \frac{\mathrm{d}^2 P_{\text{ion}}^{\text{Sim}}(l_{\text{max}}=12)}{\mathrm{d}K_\perp \mathrm{d}k}}{\frac{\mathrm{d}^2 P_{\text{ion}}^{\text{Sim}}(l_{\text{max}}=12)}{\mathrm{d}K_\perp \mathrm{d}k}} \right| \quad , \tag{4.94}$$

i.e. the relative difference of the momentum distributions calculated using $l_{\text{max}} = 12$ and $l_{\text{max}} = 10$, is shown as a function of the parameters $K_\perp$ and k. As before, all results are calculated for the initial configuration $l_1 = l_2 = 5$, $u_1 = u_2 = \zeta$, and $s_i = 0$, with the laser parameters $F_0 = 0.04\,\text{a.u.}$ and $\lambda = 8000\,\text{nm}$. From the figure, it can be seen that the deviation is on the order of 10^{-12} for the momenta shown there. The choice of $l_{\text{max}} = 12$ used throughout this work is therefore assumed to be sufficient.

Notice that due to the singlet symmetry of the initial state that was chosen here, only even quantum numbers l contribute to the final state due to the fermionic antisymmetry. For the parameters used in fig. 4.8, the deviation of the distribution obtained for $l_{\text{max}} = 0$ from the one obtained for $l_{\text{max}} = 12$ is around 85% for typical values of the final momenta, while the deviation of the distribution obtained for $l_{\text{max}} = 2$ from the one obtained for $l_{\text{max}} = 12$ is only around 25%. Hence, the dominant contribution to the final state is $l = 2$ in this case.

4.3 Correlated Sequential Ionization

As discussed in section 4.1, the sequential ionization channel consists of the consecutive ejection of two single electrons.

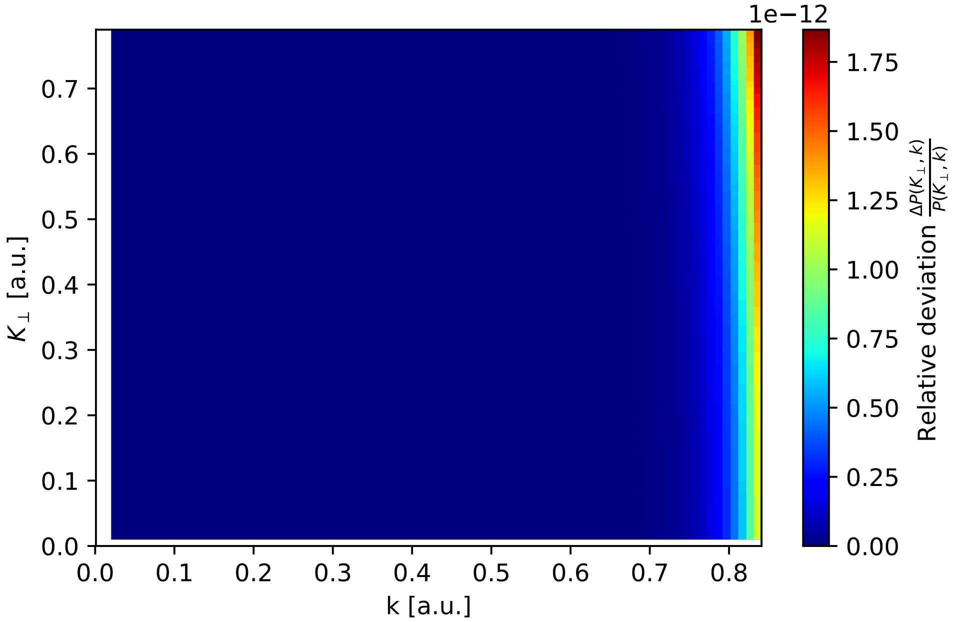

FIGURE 4.8: Relative deviation $\frac{\Delta P(K_\perp,k)}{P(K_\perp,k)}$ (see eq. (4.94)) of the momentum distributions $\frac{\mathrm{d}^2 P_{\mathrm{ion}}^{\mathrm{Sim}}}{\mathrm{d}K_\perp \mathrm{d}k}$ obtained for $l_{\max} = 10$ and $l_{\max} = 12$, plotted as a function of the final state parameters $K_\perp$ and k. For the parameter range displayed, the maximum deviation is around 10^{-12}, and this maximum value is only reached for high values of k. For these values, the absolute value of the momentum distribution is already very small, as can be seen from fig. 4.6. All results are calculated for the initial configuration $l_1 = l_2 = 5$, $u_1 = u_2 = \zeta$, and $s_i = 0$, with the laser parameters $F_0 = 0.04\,\mathrm{a.u.}$ and $\lambda = 8000\,\mathrm{nm}$.

Before the laser pulse, the active electrons can be found in the 2-electron ground state which, as already discussed in section 4.2.2, reads

$$|g_2\rangle = N\left(|l_1, u_1\rangle \otimes |l_2, u_2\rangle + (-1)^{s_i} |l_2, u_2\rangle \otimes |l_1, u_1\rangle\right) \otimes |s_i, m_{s_i}\rangle \tag{4.95}$$

in the rigid-rotor model.

4.3.1 First Step

The ionization matrix element of the “first”[5] electron is the ionization matrix element of single ionization. This has been calculated in chapter 3 and, under

---

[5] The notion of “first” and “second” electrons is of course incorrect for interchangeable particles, it is used here to refer to the transition in the first/second 3 spatial degrees of freedom of the wave function into their ionized state as described in eqs. (4.99) and (4.100) respectively.

the assumptions made in chapter 3, can be read directly from eq. (3.51):

$$
\begin{aligned}
M^{\text{Single}}_{l_1,u_1}(\vec{k}_1) = & -i\sum_{m_1} c_{u_1 m_1}\delta_{m_1,0}e^{f(t_{r,1},z=0)}\eta(z=-r_0) \\
& \cdot \frac{N_{l_1 m_1}}{\sqrt{2\pi}} \frac{F(t_{r,1})r_0^2}{\sqrt{\left| -\frac{F^2(t_{r,1})}{m_e}\frac{\gamma_{\text{Kel}}(k_{\perp,1},z=-r_0)}{\omega} - ir_0 \left.\frac{\mathrm{d}F(t)}{\mathrm{d}t}\right|_{t=t_{r,1}} \right|}} \\
& \cdot \int \mathrm{d}x\; x\; P_{l_1|m_1|}(x) \exp\left(-\frac{2}{3}\frac{\sqrt{2m_e}}{F(t_{r,1})}\left(I_{P,1}(k_{\perp,1}) + xF(t_{r,1})r_0\right)^{3/2} \right) \quad .
\end{aligned}
\tag{4.96}
$$

This formula holds for an electron initially bound in the rigid-rotor state $|l_1, u_1\rangle$, with the ionization potential

$$
I_{P,1}(k_{\perp,1}) = |E_1| + \frac{k^2_{\perp,1}}{2m_e} \quad , \tag{4.97}
$$

where $|E_1| = 7.65\,\text{eV}$ according to [7], and the real part $t_{r,1}$ of the saddle point fulfills

$$
\cos(\omega t_{r,1}) = -1 - \frac{\omega k_{z,1}}{F_0} \quad . \tag{4.98}
$$

After this first step, the *ionized part* of the 2-electron state reads

$$
\begin{aligned}
|\psi\rangle_{0\to 1} = N \int \mathrm{d}^3k_1 \Big(& M^{\text{Single}}_{l_1,u_1}(\vec{k}_1)\,|k_1\rangle \otimes |l_2, u_2\rangle \\
& + (-1)^{s_i} M^{\text{Single}}_{l_2,u_2}(\vec{k}_1)\,|k_1\rangle \otimes |l_1, u_1\rangle \Big) \otimes |s_i, m_{s_i}\rangle \quad .
\end{aligned}
\tag{4.99}
$$

4.3.2 Uncorrelated Second Step

After the removal of the first electron, the 2-electron state has changed, and therefore the ionization of the second electron can not be described independently of the first electron's state. Formally speaking, the ionization matrix element for the entire process $M^{\text{Seq}}_{l_1,u_1,l_2,u_2}(\vec{k}_1,\vec{k}_2)$ describing the *doubly ionized part* of the final state after the sequential ionization according to

$$
|\psi^{\text{Seq}}_{\text{ion}}\rangle = N \int \mathrm{d}^3k_1 \int \mathrm{d}^3k_2 \Big(M^{\text{Seq}}_{l_1,u_1,l_2,u_2}(\vec{k}_1,\vec{k}_2) \tag{4.100}
$$

$$
+ (-1)^{s_i} M^{\text{Seq}}_{l_2,u_2,l_1,u_1}(\vec{k}_1,\vec{k}_2)\,|\vec{k}_1,\vec{k}_2\rangle \Big) \otimes |s_i, m_{s_i}\rangle \tag{4.101}
$$

can not be written as a product

$$
M^{\text{Seq}}_{l_1,u_1,l_2,u_2}(\vec{k}_1,\vec{k}_2) \neq M^{\text{Single}}_{l_1,u_1}(\vec{k}_1) M^{\text{Single}}_{l_2,u_2}(\vec{k}_2) \quad . \tag{4.102}
$$

Instead, the interaction of the second electron with the first one has to be taken into account. The most obvious consequence of the first electron being removed is that the ionization potential of the second electron, $I_{P,2}(k_{\perp,2})$, is different from the ionization potential of the first electron, $I_{P,1}(k_{\perp,1})$. Assuming that the ion is able to quasi-statically relax to its ground state before the ionization of the second electron (see section 5.2.3 for a discussion of this assumption), the resulting ionization potential for the second electron is the difference

$$I_{P,2}(k_{\perp,2}) = |E_1 - E_2| + \frac{k_{\perp,2}^2}{2m_e} \quad , \tag{4.103}$$

where $|E_2| = 18.98\,\mathrm{eV}$ is the minimum energy to remove 2 electrons from C_{60}, and $|E_1| = 7.65\,\mathrm{eV}$ is the minimum energy to remove a single electron (both values from [7]). The difference's value is

$$|E_1 - E_2| \approx 11.33\,\mathrm{eV} \quad . \tag{4.104}$$

In the picture provided by the saddle point approximation, the overwhelmingly dominant part of the entire ionization process happens, for each electron, at an instant in time $t_{r,i}$ that is connected to the final $k_{z,i}$-momentum via the relation

$$\cos(\omega t_{r,i}) = -1 - \frac{\omega k_{z,i}}{F_0} \quad . \tag{4.105}$$

Per definition, the ejection of the first electron has to "happen" before the ejection of the second electron. Within the saddle point approximation, this can be formulated by

$$t_{r,2} > t_{r,1} \iff k_{z,2} > k_{z,1} \quad . \tag{4.106}$$

Using this, the sequential ionization matrix element can be written according to

$$M^{\text{Seq, SM}}_{l_1,u_1,l_2,u_2}(\vec{k}_1,\vec{k}_2) = \begin{cases} M^{\text{Single}}_{l_1,u_1}(k_{\perp,1},k_{z,1}) M^{\text{Single}}_{l_2,u_2}(k_{\perp,2},k_{z,2}) & k_{z,2} > k_{z,1} \\ 0 & \text{otherwise} \end{cases} \quad . \tag{4.107}$$

This model assumes that there are no interaction effects between the 2 electrons once the first electron is removed, and therefore the Coulomb blockade is not included. As the Coulomb blockade is an interesting feature and the central focus of this work, this is improved on in the following section. For now, the presented model is referred to as a first simple man's (SM) approximation for sequential ionization in the following.

4.3.3 Coulomb Interaction Effects

The model description for simultaneous ionization developed in section 4.2 naturally incorporates Coulomb interaction effects, because the ionization amplitude into the correlated 2-electron state is calculated. The sequential simple man's description formulated in eq. (4.107) however does not contain Coulomb interaction effects, as during the calculation of the ionization amplitude for the second electron, an uncorrelated final state was assumed. The explicit incorporation of the Coulomb interaction in the second step, i.e. the direct transition from the singly ionized state to the doubly ionized state that was used in the model for simultaneous ionization, is not easy to calculate because of the different symmetries of the singly ionized state and the doubly ionized Coulomb wave state. Instead, a proposal to describe Coulomb interaction in sequential ionization in a 3-step model is introduced in the following. This model assumes an uncorrelated final state, but reintroduces correlation via a time-dependent ionization potential. This assumption becomes accurate for large relative momenta, as is discussed later on.

4.3.3.1 Step 1: Removal of the "first" electron

The removal of the "first" electron happens as described in section 4.3.1.

4.3.3.2 Step 2: Quasiclassical Trajectory of the First Electron

The z-momenta of the ionized part of the wave function are peaked at $-\frac{F_0}{\omega}$, and the perpendicular momentum is peaked at 0. The width of the momentum distribution in $k_\perp$ direction is determined by the ionization potential, and for sufficiently large values of $-\frac{F_0}{\omega}$, it is much smaller than the latter. In the saddle point approximation, an ionized electronic wave packet detected with momentum $k_{z,1}$ after the pulse is predominantly created at $t_{r,1}$ (see again eq. (4.105)), initially with $k_z = 0$. If the width of this wave packet in z- and in perpendicular direction is neglected[6], it can be seen as a classical particle. It is accelerated according to Newton's equation of motion

$$p_z(t, t_{r,1}) = -\int_{t_{r,1}}^{t} \mathrm{d}t' F(t') \tag{4.108}$$

$$z(t, t_{r,1}) = \frac{1}{m_e} \int_{t_{r,1}}^{t} \mathrm{d}t' p_z(t') \quad . \tag{4.109}$$

At the origin, i.e. the location of the molecule that is small compared to the length scale $\frac{F_0}{m_e \omega^2}$ provided by the field, the resulting time-dependent Coulomb interaction energy reads

$$V(t, t_{r,1}) = \frac{1}{|z(t, t_{r,1})|} \quad . \tag{4.110}$$

---

[6] Notice that the neglect of the width in perpendicular direction leads to an underestimation of the sequential ionization yield, as is discussed in section 5.2.4.

4.3.3.3 Step 3: Modified Ionization Potential for the Second Electron

In this picture, the second electron tunneling at $t_{r,2}$ (in the sense of the saddle point approximation) "sees" an increased ionization potential

$$I_{P,2}(k_{\perp,2}, t_{r,2}, t_{r,1}) = |E_1 - E_2| + \frac{k_{\perp,2}^2}{2m_e} + V(t_{r,2}, t_{r,1}) \tag{4.111}$$

due to the Coulomb interaction with the electron that already escaped. Because the $t_{r,i}$ can be mapped directly to the momenta at the detector $k_{z,i}$, one can write the ionization potential the second electron experiences when escaping as a function of $k_{\perp,2}$, $k_{z,2}$, and $k_{z,1}$ as well:

$$I_{P,2}(k_{\perp,2}, k_{z,2}, k_{z,1}) = I_{P,2}(k_{\perp,2}, t_{r,2}(k_{z,2}), t_{r,1}(k_{z,1})) \tag{4.112}$$

This can be used to correct the ionization amplitude of the second electron for Coulomb interaction effects by replacing the "bare" ionization potential $I_{P,2}(k_{\perp,2})$ with $I_{P,2}(\vec{k}_2, k_{z,1})$ in $M^{\text{Single}}_{l_2,u_2}(k_{\perp,2}, k_{z,2})$. The resulting amplitude is denoted as

$$M^{\text{Second}}_{l_2,u_2}(k_{\perp,2}, k_{z,2}|k_{z,1}) \tag{4.113}$$

in the following to emphasize that it is conditionally dependent on $k_{z,1}$ as well. This leads to a formulation of the correlated sequential ionization amplitude corrected for Coulomb interaction (CI)

$$M^{\text{Seq, CI}}_{l_1,u_1,l_2,u_2}(\vec{k}_1, \vec{k}_2) = \begin{cases} M^{\text{Single}}_{l_1,u_1}(k_{\perp,1}, k_{z,1}) M^{\text{Second}}_{l_2,u_2}(k_{\perp,2}, k_{z,2}|k_{z,1}) & k_{z,2} > k_{z,1} \\ 0 & \text{otherwise} \end{cases} . \tag{4.114}$$

4.3.3.4 Justification for the Uncorrelated Final State

In the simultaneous case (section 4.2), the transition dipole moment from the 2-electron bound state into the doubly ionized and fully correlated 2-electron Coulomb wave function was used. In the proposed 3-step model however, the final state is assumed to be an uncorrelated plane wave of 2 electrons, with an "artificially" introduced correlation via the increased ionization potential. This is justified as long as the final state distribution is such that both particles are separated sufficiently far, and therefore their Coulomb interaction energy is much lower than their kinetic energy. To obtain a lower estimate for this separation, assume that — in a semiclassical picture — the first electron is, after being ejected with initial momentum 0, accelerated along the z axis in a constant field of field strength F_0, until after Δt, the second electron is ejected with momentum 0. In the meantime, the first electron has accelerated to the momentum

$$k_1 = F_0 \Delta t \quad , \tag{4.115}$$

and its separation from the first electron is at least

$$\Delta z = F_0 \frac{(\Delta t)^2}{2} = \frac{k_1^2}{2F_0} \quad , \tag{4.116}$$

and even more if the first or the second electron had a nonzero lateral momentum. After ionization, the relative momentum does not change anymore, such that

$$k = \frac{1}{2}(k_2 - k_1) = -\frac{k_1}{2} \tag{4.117}$$

is the relative momentum measured at the detector. The resulting Coulomb interaction energy is

$$E_{\text{pot}} = \frac{1}{|\Delta z|} = \frac{F_0}{2k^2} \quad , \tag{4.118}$$

while the kinetic energy of the relative motion is

$$E_{\text{kin}} = \frac{k^2}{2\mu} \quad . \tag{4.119}$$

Hence, for relative momenta k for which the ratio

$$\frac{E_{\text{pot}}}{E_{\text{kin}}} = \frac{\mu F_0}{k^4} \tag{4.120}$$

is small, the assumption that the final state is uncorrelated is well justified. The distributions shown later in this chapter peak at around $k \approx 0.8$, while the maximum F_0 used is 0.04 a.u. This results in an estimated ratio of kinetic and potential energy of ca. 5%, indicating that the assumption of an uncorrelated final state works well here. Notice that the peak field strength is not present during the entire pulse, which also acts in favor of the assumption of an uncorrelated final state (smaller effective F_0). Remember that the electric field is linearly polarized and only lasts for half a cycle, i.e. it is always points along the positive z direction and only changes its amplitude.

4.3.4 Differential Ionization Probability

4.3.4.1 Absolute Coordinates

Once $M^{\text{Seq, CI}}_{l_1,u_1,l_2,u_2}(\vec{k}_1, \vec{k}_2)$ has been calculated, the total ionization probability can be calculated from eq. (4.100).

$$P^{\text{Seq}}_{\text{ion}} = \langle \psi^{\text{Seq}}_{\text{ion}} | \psi^{\text{Seq}}_{\text{ion}} \rangle \tag{4.121}$$

$$= |N|^2 \int \mathrm{d}^3 k_1 \int \mathrm{d}^3 k_2 \left| M^{\text{Seq}}_{l_1,u_1,l_2,u_2}(\vec{k}_1, \vec{k}_2) + (-1)^{s_i} M^{\text{Seq}}_{l_2,u_2,l_1,u_1}(\vec{k}_1, \vec{k}_2) \right|^2 \tag{4.122}$$

Using that $M^{\mathrm{Seq}}_{l_1,u_1,l_2,u_2}(\vec{k}_1,\vec{k}_2)$ is cylindrically symmetric in both the $k_{x,1}$-$k_{y,1}$ and the $k_{x,2}$-$k_{y,2}$-plane, this can be simplified to

$$\begin{aligned} P^{\mathrm{Seq}}_{\mathrm{ion}} =& |2\pi N|^2 \int \mathrm{d}k_{z,1} \int \mathrm{d}k_{\perp,1} \int \mathrm{d}k_{z,2} \int \mathrm{d}k_{\perp,2} \\ & \cdot k_{\perp,1}k_{\perp,2} \Big| M^{\mathrm{Seq}}_{l_1,u_1,l_2,u_2}(k_{z,1},k_{\perp,1},k_{z,2},k_{\perp,2}) \\ & + (-1)^{s_i} M^{\mathrm{Seq}}_{l_2,u_2,l_1,u_1}(k_{z,1},k_{\perp,1},k_{z,2},k_{\perp,2}) \Big|^2 \quad , \end{aligned} \tag{4.123}$$

and therefore the differential ionization probability reads

$$\begin{aligned} \frac{\mathrm{d}^4 P^{\mathrm{Seq}}_{\mathrm{ion}}}{\mathrm{d}k_{z,1}\mathrm{d}k_{\perp,1}\mathrm{d}k_{z,2}\mathrm{d}k_{\perp,2}} =& |2\pi N|^2 k_{\perp,1}k_{\perp,2} \\ & \cdot \Big| M^{\mathrm{Seq}}_{l_1,u_1,l_2,u_2}(k_{z,1},k_{\perp,1},k_{z,2},k_{\perp,2}) \\ & + (-1)^{s_i} M^{\mathrm{Seq}}_{l_2,u_2,l_1,u_1}(k_{z,1},k_{\perp,1},k_{z,2},k_{\perp,2}) \Big|^2 \quad . \end{aligned} \tag{4.124}$$

4.3.4.2 COM Coordinates

In COM and relative momenta, i.e. using

$$\vec{K} = \vec{k}_1 + \vec{k}_2 \tag{4.125}$$

$$\vec{k} = \frac{1}{2}\left(\vec{k}_2 - \vec{k}_1\right) \quad , \tag{4.126}$$

$P^{\mathrm{Seq}}_{\mathrm{ion}}$ reads

$$P^{\mathrm{Seq}}_{\mathrm{ion}} = |N|^2 \int \mathrm{d}^3K \int \mathrm{d}^3k \left| M^{\mathrm{Seq}}_{l_1,u_1,l_2,u_2}(\vec{K},\vec{k}) + (-1)^{s_i} M^{\mathrm{Seq}}_{l_2,u_2,l_1,u_1}(\vec{K},\vec{k}) \right|^2 \quad , \tag{4.127}$$

where the Jacobian of this coordinate transformation is 1 and

$$M^{\mathrm{Seq}}_{l_1,u_1,l_2,u_2}(\vec{K},\vec{k}) := M^{\mathrm{Seq}}_{l_1,u_1,l_2,u_2}\left(\vec{k}_1 = \frac{\vec{K}}{2} - \vec{k}, \vec{k}_2 = \frac{\vec{K}}{2} + \vec{k}\right) \quad , \tag{4.128}$$

which is neither rotationally symmetric in the K_X-K_Y-plane nor in the k_x-k_y-plane. The corresponding differential ionization probability then reads

$$\frac{\mathrm{d}^6 P^{\mathrm{Seq}}_{\mathrm{ion}}}{\mathrm{d}^3K\mathrm{d}^3k} = |N|^2 \left| M^{\mathrm{Seq}}_{l_1,u_1,l_2,u_2}(\vec{K},\vec{k}) + (-1)^{s_i} M^{\mathrm{Seq}}_{l_2,u_2,l_1,u_1}(\vec{K},\vec{k}) \right|^2 \quad . \tag{4.129}$$

4.3.4.2.1 Distribution in K_Z and k The sequential differential ionization probability in eq. (4.129) depends on six momentum components. To plot it, one has to calculate marginal or sliced distributions from it that depend on two variables at most. For numerical simplicity, $\frac{\mathrm{d}^6 P^{\mathrm{Seq}}_{\mathrm{ion}}}{\mathrm{d}^3K\mathrm{d}^3k}$ is evaluated for $K_X = K_Y =$

0 , i.e. $\vec{K}_\perp = \vec{0}$, in the following, and then the integration is performed over only two of the remaining variables. As for $\vec{K}_\perp \neq \vec{0}$, the ionization is simply suppressed exponentially both for sequential and simultaneous ionization, this case is not of great interest anyway.

For $\vec{K}_\perp = \vec{0}$, the norms of the perpendicular components fulfill

$$|\vec{k}_{\perp,1}| = |\vec{k}_{\perp,2}| = |\vec{k}_\perp| \quad . \tag{4.130}$$

As $M^{\mathrm{Seq}}_{l_1,u_1,l_2,u_2}(k_{z,1}, k_{\perp,1}, k_{z,2}, k_{\perp,2})$ is rotationally symmetric in both the $k_{x,1}$-$k_{y,1}$ and the $k_{x,2}$-$k_{y,2}$-plane, this means that $M^{\mathrm{Seq}}_{l_1,u_1,l_2,u_2}(K_Z, \vec{K}_\perp = \vec{0}, \vec{k})$ is rotationally symmetric in the k_x-k_y-plane, such that one can integrate over the planar angle, i.e.

$$\left.\frac{\mathrm{d}^5 P^{\mathrm{Seq}}_{\mathrm{ion}}}{\mathrm{d}^3 K \mathrm{d}k_z \mathrm{d}k_\perp}\right|_{\vec{K}_\perp=\vec{0}} = 2\pi k_\perp |N|^2 \Big| M^{\mathrm{Seq}}_{l_1,u_1,l_2,u_2}(K_Z, \vec{K}_\perp = \vec{0}, k_z, k_\perp) \tag{4.131}$$

$$+ (-1)^{s_i} M^{\mathrm{Seq}}_{l_2,u_2,l_1,u_1}(K_Z, \vec{K}_\perp = \vec{0}, k_z, k_\perp)\Big|^2 \quad .$$

Using $k^2 = k_z^2 + k_\perp^2$, the integration

$$\left.\frac{\mathrm{d}^4 P^{\mathrm{Seq}}_{\mathrm{ion}}}{\mathrm{d}^3 K \mathrm{d}k}\right|_{\vec{K}_\perp=\vec{0}} = \int_{-k}^{k} \mathrm{d}k_z \frac{\mathrm{d}k_\perp}{\mathrm{d}k} \left.\frac{\mathrm{d}^5 P^{\mathrm{Seq}}_{\mathrm{ion}}}{\mathrm{d}^3 K \mathrm{d}k_z \mathrm{d}k_\perp}\right|_{\vec{K}_\perp=\vec{0}} \tag{4.132}$$

$$= \int_{-k}^{k} \mathrm{d}k_z \frac{k}{k_\perp} \left.\frac{\mathrm{d}^5 P^{\mathrm{Seq}}_{\mathrm{ion}}}{\mathrm{d}^3 K \mathrm{d}k_z \mathrm{d}k_\perp}\right|_{\vec{K}_\perp=\vec{0}} \tag{4.133}$$

can then be performed numerically to obtain a 2-dimensional distribution in K_Z and k, for the slice $\vec{K}_\perp = \vec{0}$:

$$\left.\frac{\mathrm{d}^4 P^{\mathrm{Seq}}_{\mathrm{ion}}}{\mathrm{d}^3 K \mathrm{d}k}\right|_{\vec{K}_\perp=\vec{0}} = 2\pi k^2 |N|^2 \int_{-1}^{1} \mathrm{d}x \, \Big| M^{\mathrm{Seq}}_{l_1,u_1,l_2,u_2}(K_Z, \vec{K}_\perp = \vec{0}, kx, k\sqrt{1-x^2}) \tag{4.134}$$

$$+ (-1)^{s_i} M^{\mathrm{Seq}}_{l_2,u_2,l_1,u_1}(K_Z, \vec{K}_\perp = \vec{0}, kx, k\sqrt{1-x^2})\Big|^2$$

4.3.5 Results

According to the rigid-rotor model, the initial state of both active electrons in the HOMO is $l_1 = l_2 = 5$. Because with the approximations used, $m_i = 0$ is the only nonzero contribution to the model for single ionization as discussed in section 3.1.2, $u_1 = u_2 = 0$ is used as the initial state here. In this case, $s_i = 0$ to comply with fermionic antisymmetry, and $N = \frac{1}{2}$ according to eq. (4.11). In this case, the differential ionization probability in eq. (4.134) can be simplified to

$$\left.\frac{\mathrm{d}^4 P_{\mathrm{ion}}^{\mathrm{Seq}}}{\mathrm{d}^3 K \mathrm{d}k}\right|_{\vec{K}_\perp=\vec{0}} = 2\pi k^2 \int_{-1}^{1} \mathrm{d}x \, \left| M_{l_1,u_1,l_1,u_1}^{\mathrm{Seq}}(K_Z, \vec{K}_\perp = \vec{0}, kx, k\sqrt{1-x^2}) \right|^2 \quad . \tag{4.135}$$

Fig. 4.9 shows a comparison of the distributions $\left.\frac{\mathrm{d}^4 P_{\mathrm{ion}}^{\mathrm{Seq}}}{\mathrm{d}^3 K \mathrm{d}k}\right|_{\vec{K}_\perp=\vec{0}}$, once using the simple man's sequential ionization amplitude defined in eq. (4.107), and once using the sequential ionization amplitude defined in eq. (4.114), considering Coulomb interaction effects in the 3-step model. The laser parameters are $\lambda = 3000\,\mathrm{nm}$ and $F_0 = 0.04\,\mathrm{a.u.}$ Notice that the peak in k of the Coulomb-corrected distribution is around $k \approx 0.8$, for which the assumption of an uncorrelated final state should be justified according to the estimate discussed in section 4.3.3.4.

Unlike the distribution for simultaneous ionization in fig. 4.5, both distributions are not symmetrical around $K_Z = -\frac{2F_0}{\omega}$, but biased towards lower values (higher negative values) of K_Z. This is due to the fact that the ionization potential of the second electron is higher, therefore it is more likely to tunnel near to the field maximum, while this tendency is not as sharp for the first electron. This means that the most likely configuration is the first electron tunneling some time before the peak field strength, while the second electron follows close to the peak. This results in a bias towards lower values in the distribution of the COM Z-momentum K_Z.

In the correlated case, the electron escaping in the first step increases the ionization potential for the second electron by its Coulomb field before being pulled away sufficiently far by the laser field. Hence, there exists an effective "dead time" essentially preventing the second electron from escaping right after the first one. In the WKB picture, this dead time can be defined in a more explicit way, which has been done in an alternative approach to correlated sequential double ionization that is presented in section 5.1.

Since the laser pulse only lasts for half a cycle and the majority of the wave function ionizes around the peak of the intensity, the effective dead time is visible in the momentum distribution as a shift of the peak along k, i.e. along the relative momentum of the 2 electrons, towards larger values compared to the simple man's model. This is due to the second electron spending significantly less time in the remaining laser field accelerating than the first one if the first one is preventing it from escaping immediately after it. The first electron is blocking the second one due to their Coulomb interaction, and this Coulomb blockade is reflected in the shift of the peak in k direction. The simple man's model neglects the Coulomb blockade effect, and therefore the peak in k is shifted to significantly smaller k.

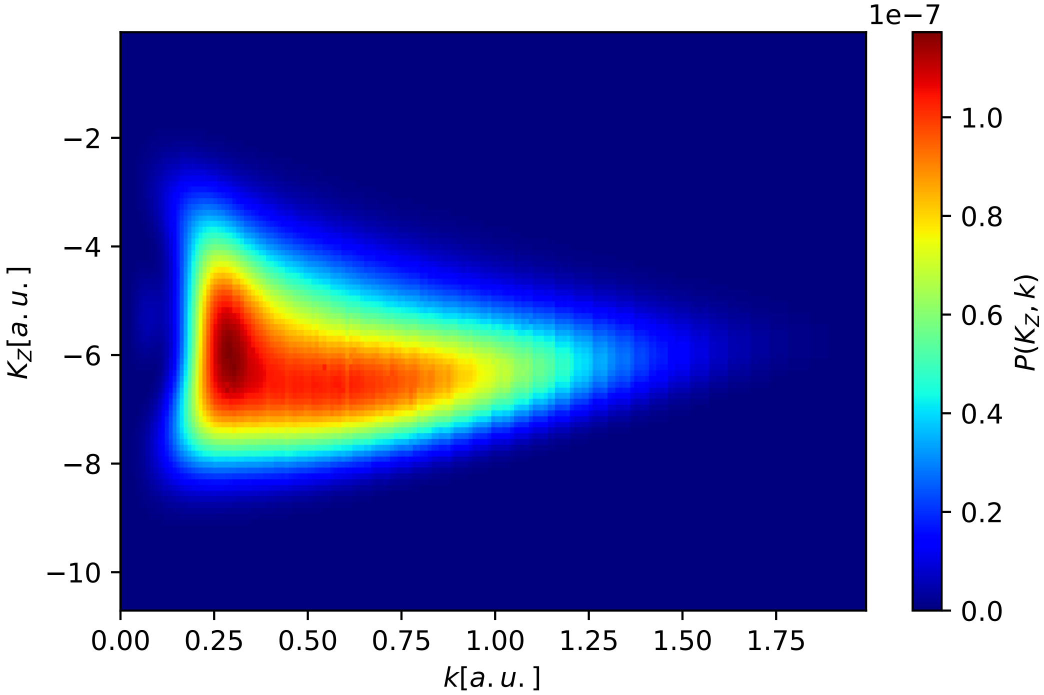

(A) Simple man's model without Coulomb interaction (see eq. (4.107))

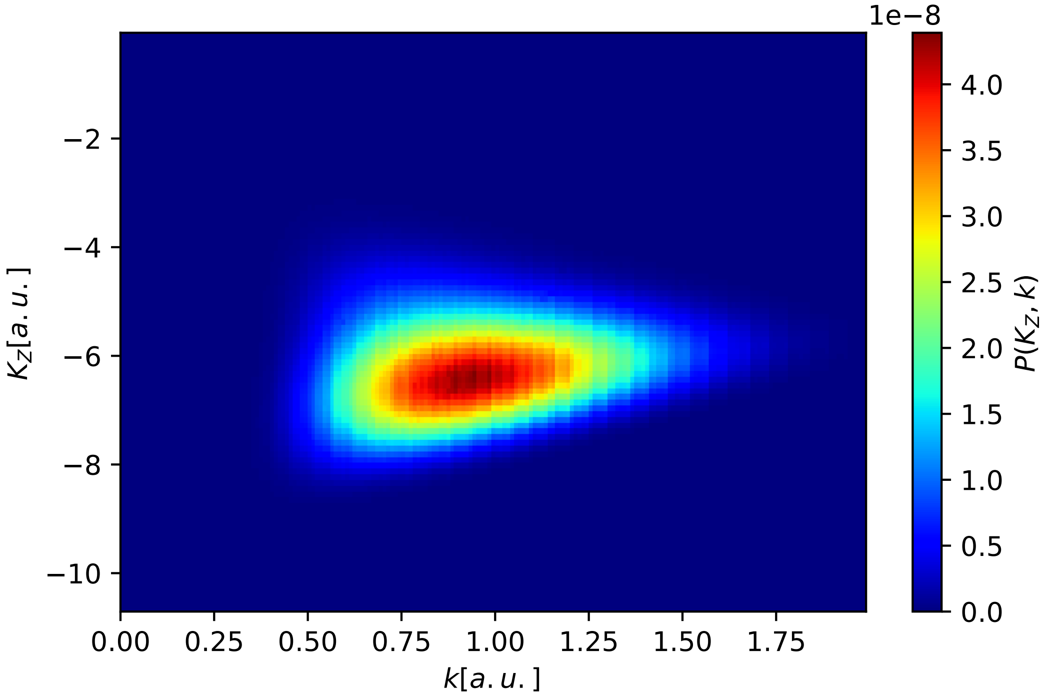

(B) Correction for Coulomb interaction (see eq. (4.114))

FIGURE 4.9: Differential ionization probability $P(K_Z,k) := \left.\frac{\mathrm{d}^4 P^{\mathrm{Seq}}_{\mathrm{ion}}}{\mathrm{d}^3 K \mathrm{d}k}\right|_{\vec{K}_\perp=\vec{0}}$ for sequential ionization, (A) neglecting Coulomb interaction effects and (B) incorporating them in the sense discussed in section 4.3.3. With Coulomb interaction considered, the first electron blocks the second electron and prevents it from escaping right after the first, leading to a k-distribution peaked at larger relative momenta k. The results are calculated for the initial configuration $l_1 = l_2 = 5$, $u_1 = u_2 = \zeta$, and $s_i = 0$. The laser parameters are $\lambda = 3000\,\mathrm{nm}$ and $F_0 = 0.04\,\mathrm{a.u.}$

4.4 Comparison of Simultaneous and Sequential Ionization

One can also ask how the Coulomb blockade effect during sequential ionization discussed in section 4.3.5 compares to the one found for simultaneous ionization (see section 4.2.8.2). To answer this, the differential ionization probability for simultaneous ionization (see eq. (4.83)) is evaluated for the same initial state ($l_1 = l_2 = 5$, $u_1 = u_2 = 0$, and $s_i = 0$) and laser parameters, i.e. $\lambda = 3000\,\mathrm{nm}$ and $F_0 = 0.04\,\mathrm{a.u.}$ As in the sequential case, the slice at $\vec{K}_\perp = 0$ is calculated, i.e. the quantity

$$\left.\frac{\mathrm{d}^4 P_{\mathrm{ion}}^{\mathrm{Sim}}}{\mathrm{d}^3 K \mathrm{d}k}\right|_{\vec{K}_\perp = 0} = \sum_{lm} \left| M_{\mathrm{ion}}^{\mathrm{SFA}}(K_Z, \vec{K}_\perp = \vec{0}, k, l, m) \right|^2 \quad . \tag{4.136}$$

Fig. 4.10 compares the distributions for both cases. One can see that for the present laser parameters, the probability of ionization via the simultaneous channel is much smaller than via the sequential channel. While the k-value of the peak for both distributions is shifted to larger values of k compared to the sequential and uncorrelated case in fig. 4.9a, the distribution in the sequential case stretches to larger values of k than in the simultaneous case. In the simultaneous case, k denotes the (kinetic and potential) energy of the relative motion of both electrons right after they escaped simultaneously. This additional energy increases the ionization potential for simultaneous ionization and therefore exponentially lowers the simultaneous ionization probability. In the sequential case however, k corresponds to the (kinetic) energy of the first electron right after the second electron has been ejected. This relative velocity of both electrons does not add to the ionization potential of the second electron. Therefore ionization is not suppressed towards larger values of k, and it is only limited by the duration and field strength of the laser pulse.

Consider an electron that has tunneled around the peak of the field. The time it takes to move the electron depends on the field strength of the external field, and if the pulse duration is rather short, the field and therefore the ionization probability might be much smaller once the second electron is able to escape. This means that shorter pulse lengths decrease the margin by which the sequential channel dominates the ionization dynamics over the simultaneous channel.

This effect can be seen by comparing fig. 4.10 to fig. 4.11, showing the same distributions for 3000 nm and 1800 nm, respectively. While the peak value of the simultaneous ionization remains mostly unchanged between both pulses, the peak of the sequential channel is around 3 times smaller for the shorter wavelength. Furthermore, the peak in k of the sequential channel is sharper for the shorter wavelength (watch out for different axis scaling), which is due to the effect of a shorter time window for ionization that was explained before. However, for the laser parameter regime treated in this work, the sequential channel remains clearly dominant. Notice that the Keldysh parameter for 1800 nm and $F_0 = 0.04\,\mathrm{a.u.}$ is around 0.5, therefore these parameters are at the border of the quasi-static regime.

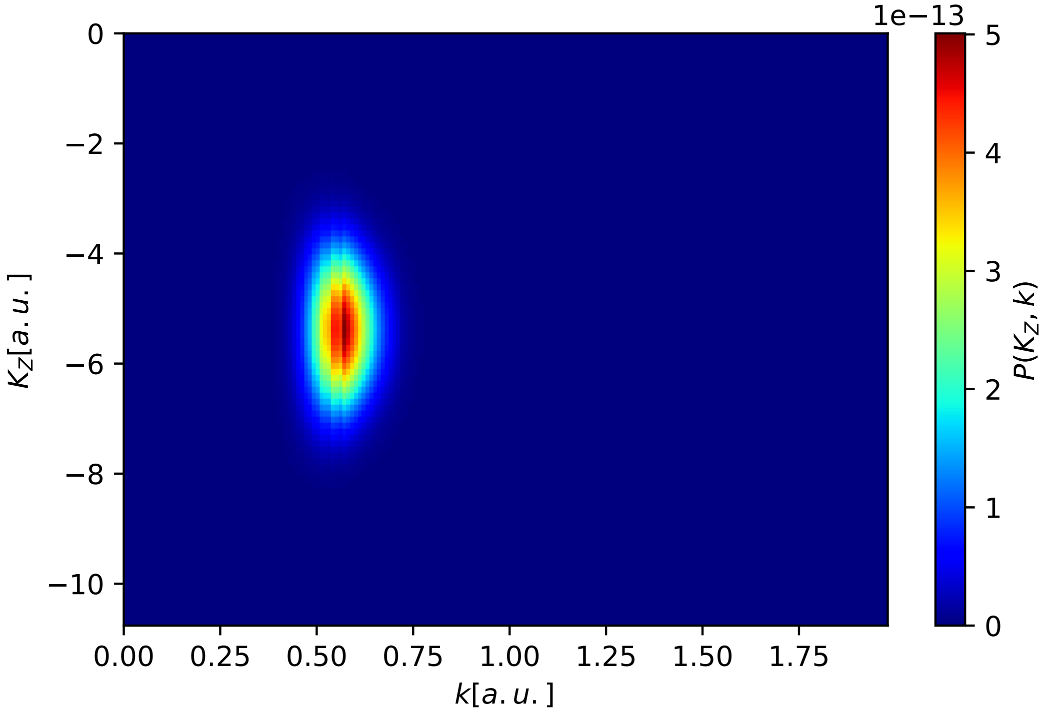

(A) Simultaneous ionization (see eq. (4.136))

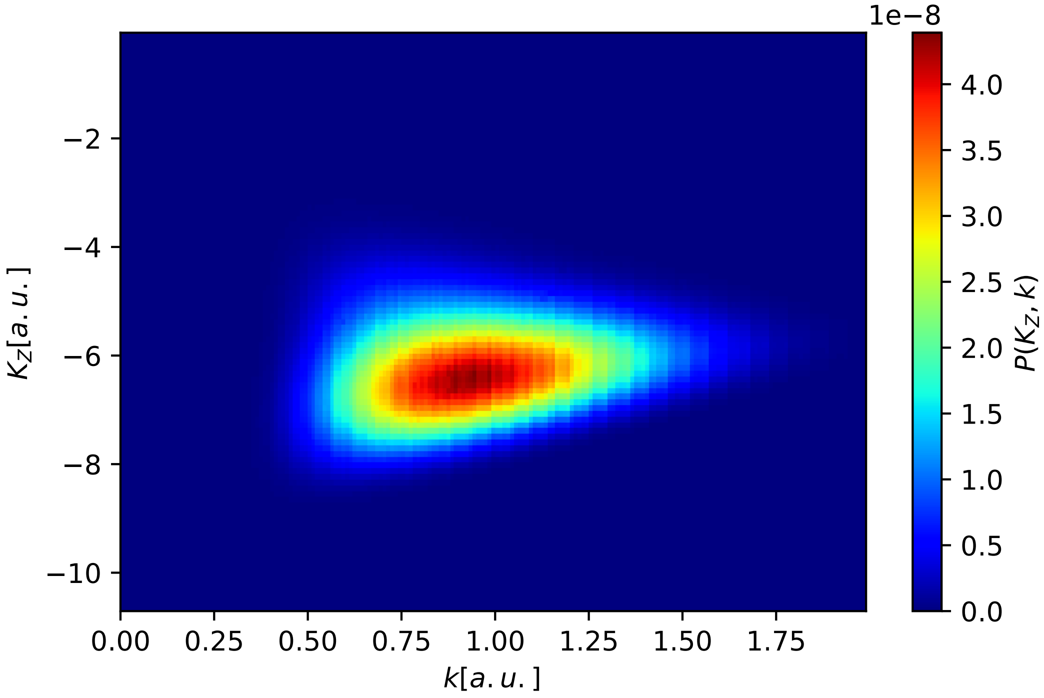

(B) Sequential ionization with Coulomb interaction, see eq. (4.134)

Figure 4.10: Differential ionization probability $P(K_Z, k) := \left.\frac{\mathrm{d}^4 P_{\text{ion}}}{\mathrm{d}^3 K \mathrm{d}k}\right|_{\vec{K}_\perp = 0}$ for (A) simultaneous and (B) sequential double ionization, taking into account Coulomb interaction effects. The simultaneous channel is several orders of magnitude weaker than the sequential channel. The results are calculated for the initial configuration $l_1 = l_2 = 5$, $u_1 = u_2 = \zeta$, and $s_i = 0$. The laser parameters are $\lambda = 3000\,\text{nm}$ and $F_0 = 0.04\,\text{a.u.}$

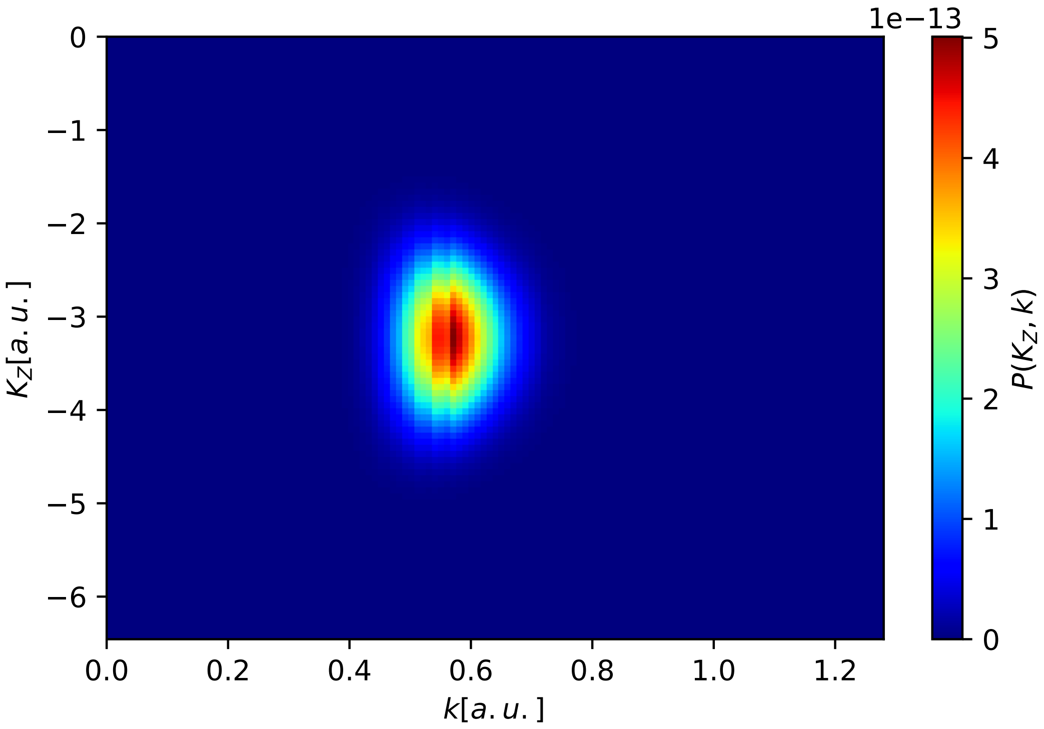

(A) Simultaneous ionization (see eq. (4.136))

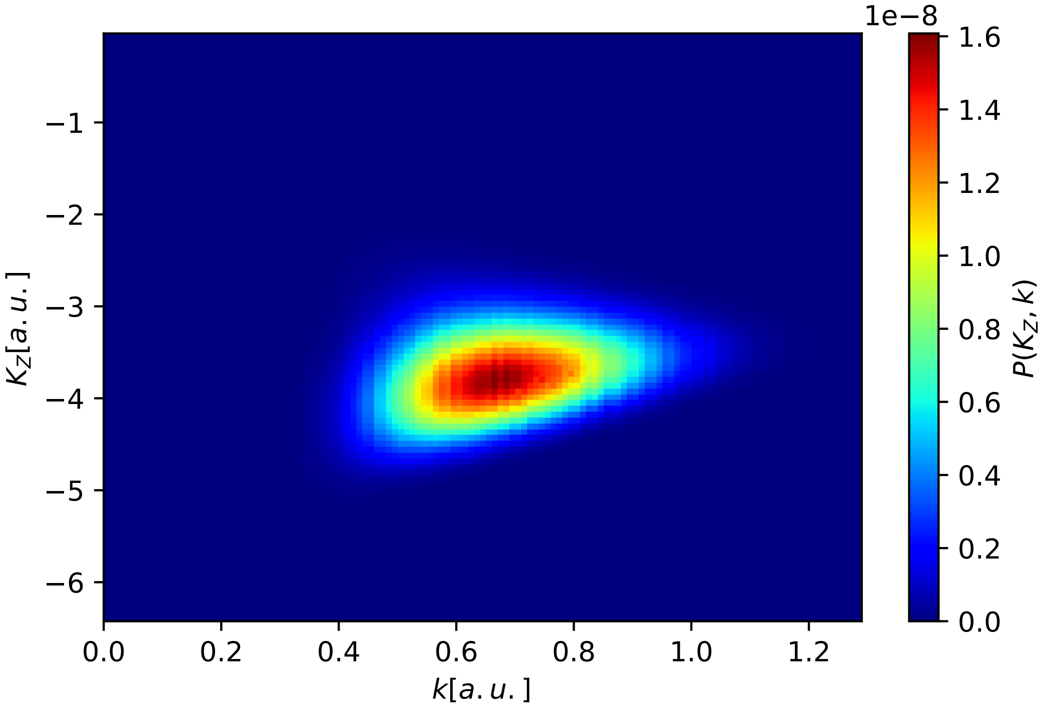

(B) Sequential ionization with Coulomb interaction, see eq. (4.134)

FIGURE 4.11: Differential ionization probability $P(K_Z, k) \coloneqq \left.\frac{\mathrm{d}^4 P_{\text{ion}}}{\mathrm{d}^3 K \mathrm{d}k}\right|_{\vec{K}_\perp = 0}$ for (A) simultaneous and (B) sequential double ionization, taking into account Coulomb interaction effects. The simultaneous channel is several orders of magnitude weaker than the sequential channel. The results are calculated for the initial configuration $l_1 = l_2 = 5$, $u_1 = u_2 = \zeta$, and $s_i = 0$. The laser parameters are $\lambda = 1800\,\mathrm{nm}$ and $F_0 = 0.04\,\mathrm{a.u.}$

In the simultaneous case, the parameter k has the meaning of an energy parameter and contains contributions both from the kinetic and the potential energy of the relative 2-electron motion, while k in the case of sequential ionization is the relative momentum of the 2 electrons, and can be seen as an energy parameter only taking into account kinetic energy while neglecting potential energy. As discussed in section 4.3.3.4, for k around the peak of the sequential distribution ($k \approx 0.8$), the potential energy is negligible, such that both definitions of k become equivalent. However, for the lower end of the sequential distribution, around $k \approx 0.5$, the ratio of potential and kinetic energy is about 30%, meaning that the model for sequential ionization does not yield accurate results in this regime.

Chapter 5

Discussion and Conclusion

5.1 Alternative Model for Correlated Sequential Ionization

In the discussion of the results for correlated sequential ionziation in section 4.3.5, the shift of the peak position in direction of the relative momentum k compared to the uncorrelated case was explained by an effective "dead time" preventing the second ionization to happen right after the first. This "dead time" can be defined in a more explicit way, as done in the following alternative approach to sequential ionization. This is helpful for the discussion as it allows for a link between the SFA and the Wenzel-Kramers-Brillouin (WKB) approximation (see also section 5.2.1.2).

The alternative model is very similar to the one presented in section 4.3.3, however, the influence of the Coulomb repulsion of the electron that was ejected first with the second one is described differently. Having the WKB tunneling picture in mind, the idea is to define a "dead time" after the ejection of the first electron at $t_{r,1}$ that has to pass until the second electron can escape at $t_{r,2}$[1].

As in section 4.3.3, the sequential ionization is described in a 3-step model.

5.1.1 Step 1: Removal of the "first" electron

Just as in section 4.3.3, the removal of the "first" electron happens at $t_{r,1}$ as described in section 4.3.1.

5.1.2 Step 2: Quasiclassical Trajectory of the First Electron

Again as in section 4.3.3, the movement of the first electron in the electric field is described classically. This results in a trajectory $z(t)$ along the field axis in

---

[1] Notice, as mentioned before, that the assignment of discrete times to the ionization process is only well-defined within the saddle point approximation.

the negative z direction according to

$$p_z(t, t_{r,1}) = -\int_{t_{r,1}}^{t} \mathrm{d}t' F(t') \tag{5.1}$$

$$z(t, t_{r,1}) = \frac{1}{m_e} \int_{t_{r,1}}^{t} \mathrm{d}t' p_z(t') \quad . \tag{5.2}$$

However, in contrast to the model presented in section 4.3.3, this trajectory is not used to construct a time-dependent (decreasing) additional ionization potential for the second electron that suppresses its escape for some characteristic time. Instead, it is used to define a sharp cutoff time before which a second ionization is not possible, and after which it can happen without being influenced by the first electron at all. This time $t_{r,2,\mathrm{min}}(t_{r,1})$ is defined as the smallest time $t > t_{r,1}$ for which

$$\min_{z(t,t_{r,1})<z<0} \left(Fz + \frac{1}{|z - z(t, t_{r,1})|} \right) < -I_{P,2} \tag{5.3}$$

is fulfilled. In the picture provided by the WKB approximation, this is the earliest time after the first ionization at which the second electron at energy $-I_{P,2}$ is able to tunnel through a finite barrier in z direction.

5.1.3 Step 3: Removal of the second electron after $t_{r,2,\mathbf{min}}(t_{r,1})$

As soon as $t \geq t_{r,2,\mathrm{min}}(t_{r,1})$, the second electron can escape. In contrast to section 4.3.3.3, the second ionization is not modified by the Coulomb field of the first electron, but once $t \geq t_{r,2,\mathrm{min}}(t_{r,1})$, the second electron can tunnel undisturbed by the first one.

As, within the saddle point approximation, the ionization times $t_{r,i}$ can be related to the final momenta $k_{z,i}$ according to

$$\cos(\omega t_{r,i}) = -1 - \frac{\omega k_{z,i}}{F_0} \quad , \tag{5.4}$$

this "dead time" condition can be reformulated as

$$t_{r,2} > t_{r,2,\mathrm{min}}(t_{r,1}) \iff k_{z,2} > k_{z,2,\mathrm{min}}(k_{z,1}) \quad , \tag{5.5}$$

where

$$k_{z,2,\mathrm{min}}(k_{z,1}) = -\frac{F_0}{\omega} \left(1 + \cos(\omega t_{r,1}(k_{z,1}))\right) \quad . \tag{5.6}$$

The total ionization amplitude for the dead time model (DT) can then be written as

$$M^{\mathrm{Seq,\ DT}}_{l_1,u_1,l_2,u_2}(\vec{k}_1, \vec{k}_2) = \begin{cases} M^{\mathrm{Single}}_{l_1,u_1}(k_{\perp,1}, k_{z,1}) M^{\mathrm{Single}}_{l_2,u_2}(k_{\perp,2}, k_{z,2}) & k_{z,2} > k_{z,2,\mathrm{min}}(k_{z,1}) \\ 0 & \text{else} \end{cases} \quad . \tag{5.7}$$

Fig. 5.1 shows an overview for $\lambda = 3000\,\text{nm}$ and $F_0 = 0.04\,\text{a.u.}$ of how the dead time duration defined according to eq. (5.3) differs depending on $t_{r,1}$ and how this affects the possible combinations of the momenta $k_{z,1}$ and $k_{z,2}$. If the first electron is ejected before or shortly after the peak of the field is reached, it is accelerated long enough that the barrier for the second electron opens up before the end of the pulse. If the first electron is ejected towards the end of the pulse, i.e. its final z-momentum $k_{z,1}$ is close to 0, the barrier does not open before the pulse is over, and sequential ionization does not happen (no combinations of $k_{z,1}$ and $k_{z,2}$). As the ionization probability of both electrons is larger around the peak, ejection of the first electron shortly before the peak is optimal, such that the second electron can escape not too long after the field maximum.

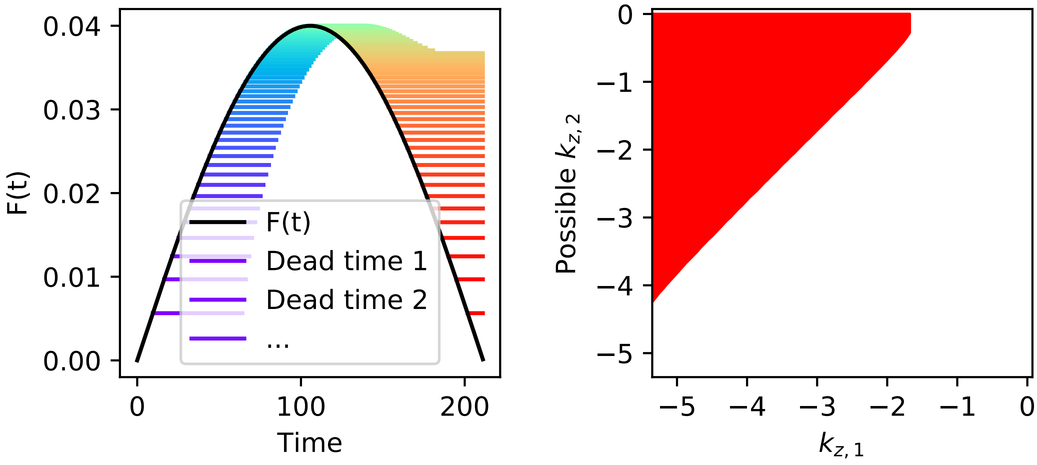

FIGURE 5.1: Left: Dead times found using eq. (5.3) for different ejection times $t_{r,1}$ of the first electron during the pulse. Right: Resulting possible combinations of the z-momenta $k_{z,1}$ and $k_{z,2}$, colored in red. The laser parameters $\lambda = 3000\,\text{nm}$ and $F_0 = 0.04\,\text{a.u.}$ have been used.

Fig. 5.2 compares the momentum distribution obtained with the presented dead time model (fig. 5.2a) to the momentum distribution obtained with the model presented in section 4.3.3 (fig. 5.2b). The distribution is calculated for the initial configuration $l_1 = l_2 = 5$ and $m_1 = m_2 = 0$, and accordingly $s_i = s_f = 0$, while the laser parameters are $\lambda = 3000\,\text{nm}$ and $F_0 = 0.04\,\text{a.u.}$

Not surprisingly, the distribution calculated with the "new" dead time model has a sharper cutoff for low relative momenta k (due to the sharp cutoff time $t_{r,2,\min}(t_{r,1})$), and towards larger values of k it reaches larger values due to the fact that the second ionization is modeled as being undisturbed. On the other hand, the Coulomb interaction increases the second electron's ionization potential in case of the model presented in section 4.3.3. This also causes the peak in k to be slightly shifted to larger relative momenta k for the latter, as for increasing relative k Coulomb suppression effects gradually decrease. However, interestingly, both models agree on the approximate location of the cutoff for low relative momenta k.

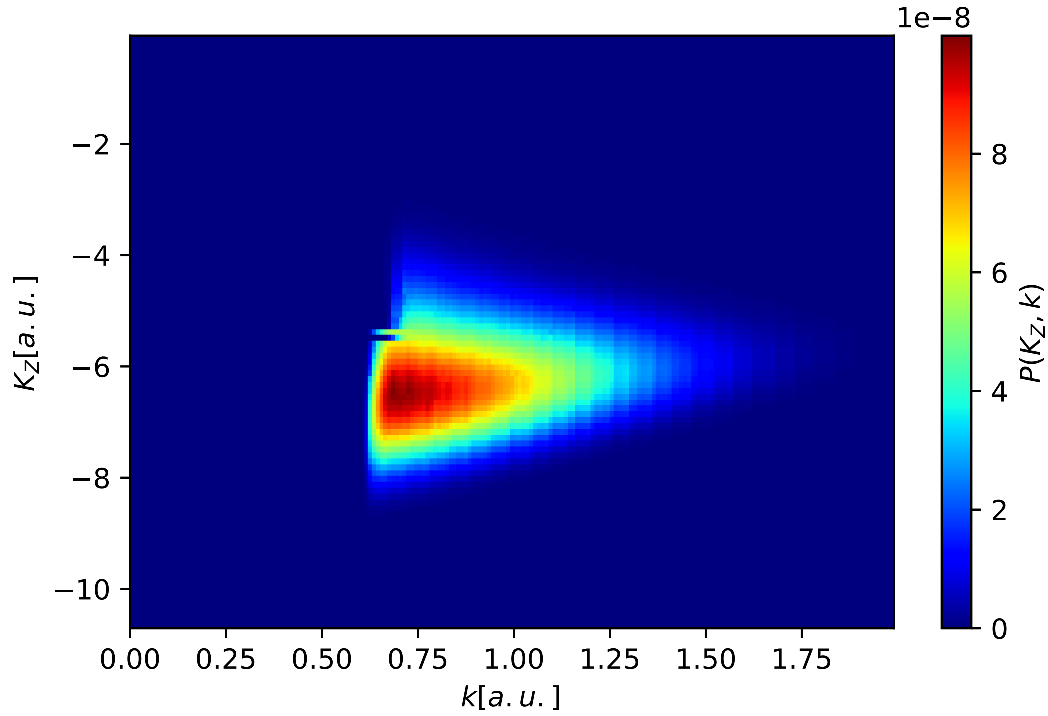

(A) Sequential ionization considering dead times as described in section 5.1

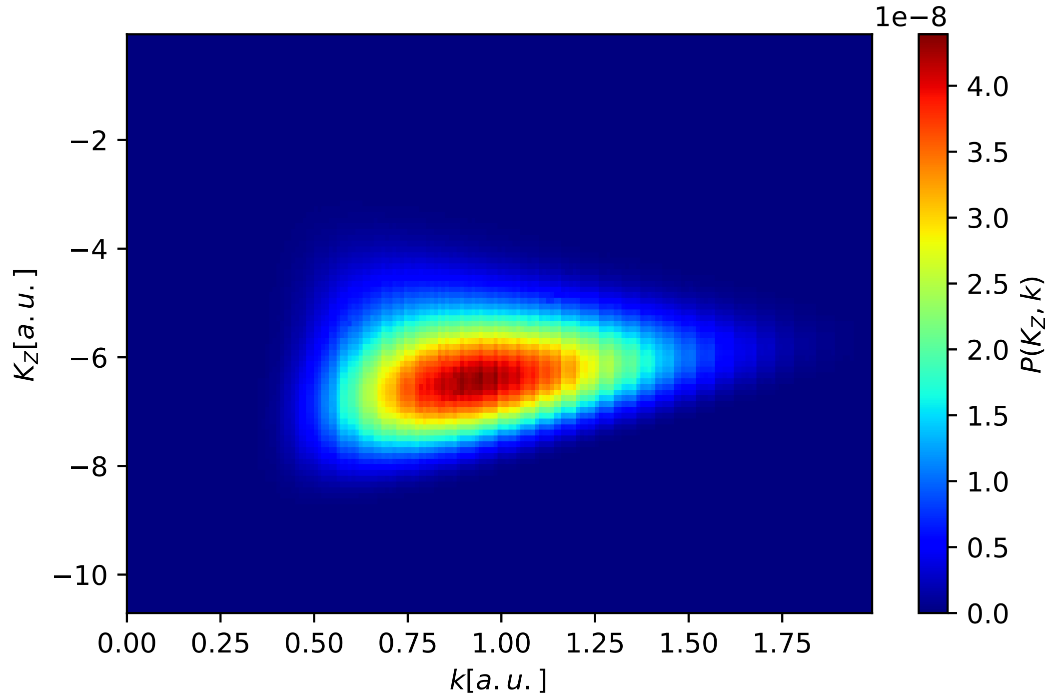

(B) Sequential ionization with time-dependent ionization potential, as described in section 4.3.3.

Figure 5.2: Differential ionization probability $P(K_Z, k) := \left.\frac{\mathrm{d}^4 P_{\mathrm{ion}}}{\mathrm{d}^3 K \mathrm{d}k}\right|_{\vec{K}_\perp = 0}$ for sequential ionization (A) considering dead times and (B) taking into account Coulomb interaction effects via an increased ionization potential. The results are calculated for the initial configuration $l_1 = l_2 = 5$, $u_1 = u_2 = \zeta$, and $s_i = 0$. The laser parameters are $\lambda = 3000\,\mathrm{nm}$ and $F_0 = 0.04\,\mathrm{a.u.}$

5.2 Limitations of the Models

The models for sequential and simultaneous double ionization of C_{60} that were presented in chapter 4 make use of many approximations which result in limitations and weak points that are discussed in the following.

5.2.1 Limitations of the SFA

5.2.1.1 Gauge Dependence

As discussed, while the Schrödinger equation in electromagnetic fields is gauge-invariant like all physical laws, this does not necessarily hold for approximate formulations like the SFA. In this case, the differences between different gauges (and different partitionings) can be orders of magnitude, like, for example, shown for length gauge and velocity gauge for the case of hydrogen in [40]. In [21], it is demonstrated that the ionization rate for a long-range Coulomb potential in velocity gauge SFA is proportional to ω in the quasi-static limit, an obviously unphysical result in the limit $\omega = 0$. In the general case however, there is no reason why one gauge should be superior to the other.

The following remarks are applicable to the SFA in length gauge and $\Lambda = (0, 0)$-partitioning, which was used throughout this work.

5.2.1.2 Neglecting the Potential for the Final State

As mentioned in paragraph 2.3.3.2.1, the action of the potential energy operator on the ionized Volkov state is neglected in SFA. The implication of this can be seen best when comparing the tunneling exponent derived in SFA and saddle point approximation to the tunneling exponent predicted by the Wenzel-Kramers-Brillouin (WKB) approximation.

The WKB approximation can be applied to predict the tunneling probability of a plane wave impacting a barrier. The position-space representation of a right-moving solution of energy E of the 1D-Schrödinger equation for a particle in a constant potential V_0 reads

$$\psi(x) \propto \exp(ip_0 x) \tag{5.8}$$

up to a normalization prefactor, where $p_0 = \sqrt{2m(E - V_0)}$. Note that this relation also holds for $V_0 > E$, where p_0 becomes imaginary and therefore $\psi(x)$ decays for growing x. For a non-constant potential $V(x)$ that changes its value on length scales much smaller than $\frac{1}{p_0}$, an approximate solution is

$$\psi(x) \propto \exp\left(i \int^x p(x)\right) \quad , \tag{5.9}$$

where $p(x) = \sqrt{2m(E - V(x))}$.

Assume a potential of the form

$$V(x) = F_0 x \quad , \tag{5.10}$$

which corresponds to a dipole approximated laser field of constant field strength in length gauge for a negative charge, and a plane wave with energy $-I_P$, where $I_P > 0$. The plane wave tunnels from the origin (where its energy is lower than $V(0) = 0$) in the direction of negative x, until its energy is larger than $V(x_{\text{end}})$, i.e. $x_{\text{end}} = -\frac{I_P}{F_0}$. From the WKB method, the relation

$$\psi(x_{\text{end}}) = \psi(0) \exp\left(-\frac{3}{2}\frac{\sqrt{2m}I_P^{3/2}}{F}\right) \tag{5.11}$$

can be derived. This exponent is exactly the same as the one found in SFA in length gauge and $\Gamma = (0,0)$-partitioning, e.g. in eq. (2.208). This allows for an illustrative interpretation of the SFA exponent: It is the WKB exponent of a bound electron impacting the barrier created by the field, *neglecting* the Coulomb potential which would modify $V(x)$. Instead, the SFA only considers the effect of the field on the potential barrier, as shown schematically in fig. 5.3.

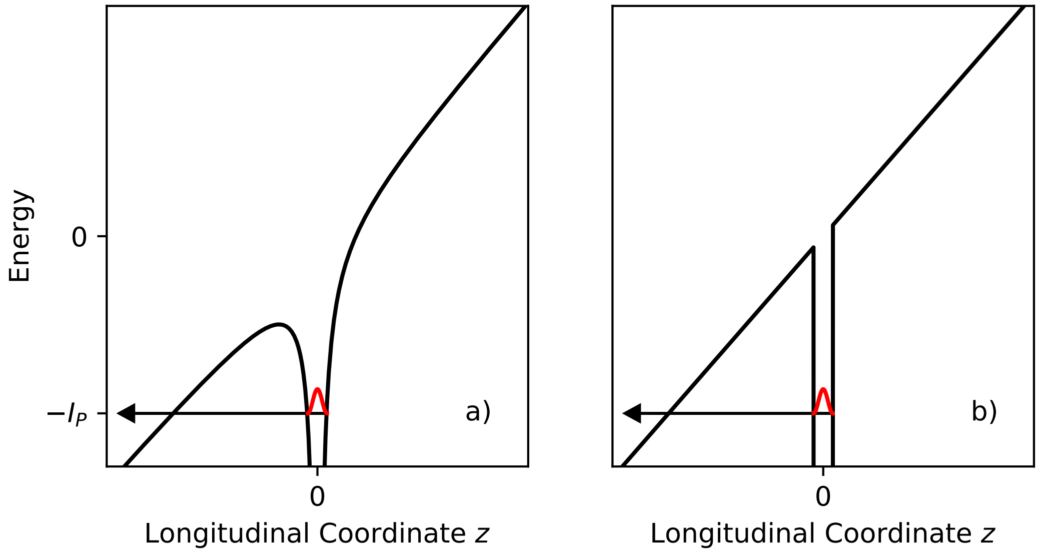

FIGURE 5.3: Schematic comparison of (a) the potential barrier created by a Coulomb potential disturbed by an external dipole approximated field, compared to (b) the barrier that is effectively considered in SFA. In SFA, the exact shape of the Coulomb potential is neglected. In this schematic representation, the width of the SFA potential at the origin is finite for illustration purposes, but it actually is infinitely narrow.

Because of the neglect of the Coulomb potential (apart from the fact that the ground state created by it is considered), the ionization process is treated in SFA neglecting all bound states of the potential except for the initial ground state, and neglecting the influence of the ion on the ejected electron once it is in its final continuum state. The former assumption means that resonant ionization is not described in SFA. The latter assumption holds for short-range potentials, however, for long-range potentials it only holds in the case sufficiently strong fields.

5.2.1.3 Neglecting the External Field for the Initial State

As mentioned in paragraph 2.3.3.2.1, in SFA in $\Lambda = (0,0)$-partitioning, the initial state is treated as it would not "feel" the external field until it is coupled to the final state at a discrete instant in time. One consequence of this is that the depletion of the initial state is neglected, as was already discussed, however, it is also neglected that if the external field is quasi-static, the ground state can be modified adiabatically due to it and its energy can be shifted. This in principle leads to a field-dependent ionization potential. This was not considered in this work, and the effect of it is discussed using perturbation theory for the rigid-rotor-states in the following.

Consider the single electron Hamiltonian in length gauge at fixed time t_0

$$\hat{\mathrm{H}} = \hat{\mathrm{H}}_0 + F(t_0)\hat{\mathrm{z}} \quad , \tag{5.12}$$

and a rigid-rotor eigenstate (not symmetry-adapted for simplicity)

$$\hat{\mathrm{H}}_0 \left| l,m \right\rangle = E_l \left| l,m \right\rangle \quad . \tag{5.13}$$

Please refer to eqs. (2.28 and 2.33) for the definitions of $|l,m\rangle$ and E_l. The resulting energy shift reads (up to quadratic order)

$$\Delta E = E_1 + E_2 \quad , \tag{5.14}$$

where

$$E_1 = \langle l,m|F(t_0)\hat{\mathrm{z}}|lm\rangle = 0 \tag{5.15}$$

is the linear correction which vanishes due to symmetry reasons, and

$$E_2 = \sum_{(l',m')\neq(l,m) \text{ and } l'\geq l} \frac{|\langle l'm'|F(t_0)\hat{\mathrm{z}}|lm\rangle|^2}{E_l - E_{l'}} \tag{5.16}$$

$$= -2m_e r_0^4 F^2(t_0)\left(\frac{1}{2(l+1)}\frac{(l+1)^2-m^2}{(2l+2)^2-1}\right) \quad , \tag{5.17}$$

where it was used that

$$xP_{lm}(x) = \frac{l-m+1}{2l+1}P_{l+1,m}(x) + \frac{l+m}{2l+1}P_{l-1,m}(x) \quad , \tag{5.18}$$

where $P_{lm}(x)$ are the associated Legendre polynomials, is the non-vanishing quadratic correction. The sum only runs over $l' \geq l$ because within the rigid-rotor model, all lower-lying l-states are occupied by the non-active π electrons. The results for E_2 using different field strengths are shown in table 5.1. For the extreme case of $F(t_0) = 0.04$ a.u. and $|m| = 0$, the shift is -0.13 a.u., which is significant in comparison to the single ionization potentials $I_{P,1}(k_\perp - 0) = 0.27$ a.u. and $I_{P,2}(k_\perp - 0) = 0.41$ a.u.

	E_2 [a.u.]	
$\|m\|$	$F(t_0) = 0.03\,\text{a.u.}$	$F(t_0) = 0.04\,\text{a.u.}$
0	-0.07	-0.13
1	-0.07	-0.12
2	-0.06	-0.11
3	-0.05	-0.10
4	-0.04	-0.07
5	-0.02	-0.04

TABLE 5.1: Second order energy shift E_2 of the rigid-rotor ground state $|l = 5, m\rangle$ for different values of $F(t_0)$ and $|m|$.

That being said, it is questionable how well the rigid-rotor model is applicable here. More importantly, when taking into account the interaction of the ground state with the external field, the non-active electrons have to be considered as well. Assuming freely moving charges, the external field will induce a polarization in the sphere of C_{60}, leading to a shielding of the field inside the molecule and to an alteration of the field in its vicinity, which is discussed in the following.

5.2.2 Limitations of the Single/Double Active Electron Approximations

Throughout this work, it has been assumed that there is only one active electron in case of single ionization and that there are two active electrons in case of double ionization. The effects of the remaining electrons are reflected in the choice of the initial state ($l = 5$) in the rigid-rotor model following the Pauli exclusion principle and of course in the experimentally obtained ionization potential. However, besides this “mean field” there is no interaction included, and the interaction of the remaining electrons with the external field is neglected as well.

As C_{60} is modeled as a conducting sphere in this work, the electrons are assumed to move freely on the sphere. In electric fields, this leads to polarization effects effectively shielding the electric field. The potential of a conducting sphere of radius r_0 inside a constant electric field $\vec{F} = F\vec{e}_z$ reads [41]

$$V(r,\theta) = F\left(r - \frac{r_0^3}{r^2}\right)\cos(\theta) \quad , \tag{5.19}$$

where θ is the angle to the z-axis the field is pointing at. Fig. 5.4 shows the resulting potential in the x-z-plane in comparison with the undisturbed potential for a field strength of $F = 0.03\,\text{a.u.}$ The potential inside the molecule is $-I_{P,1}$. The polarization of the conducting sphere shields the electric field in the vicinity of the molecule, increasing the size of the barrier the tunneling electron has to penetrate. This modified barrier shape is neglected in the presented model,

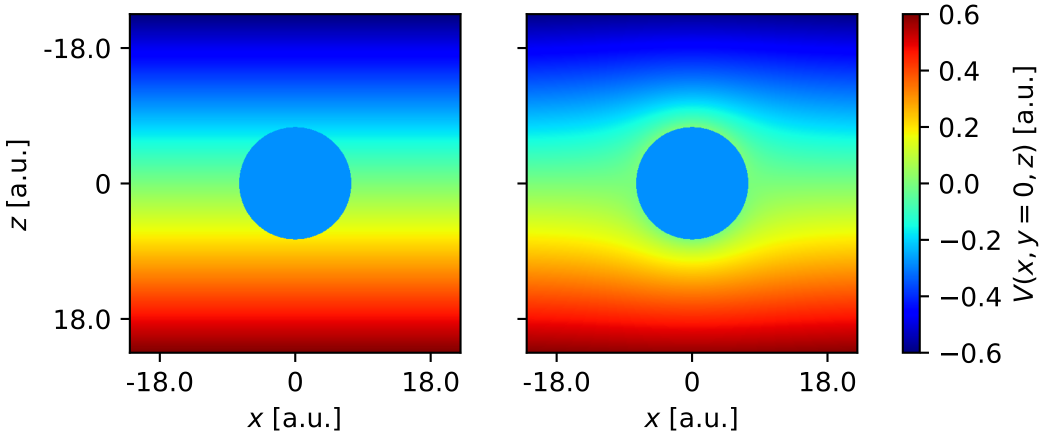

FIGURE 5.4: Undisturbed potential (left) resulting from a constant field of field strength $F = 0.03\,\text{a.u.}$ and potential with a conductive sphere with the same radius as C_{60} (right). Inside the molecule, the potential energy of the active electron is $-I_{P,1}$.

similar to the way the shape of the barrier created by the Coulomb potential is neglected in SFA (see section 5.2.1.2).

5.2.3 Non-adiabatic Effects in Sequential Ionization

In the model for sequential ionization, it was assumed that the second electron can be found in the ion's ground state directly after the removal of the first electron. While in the quasi-static limit, the timescale of the ionization itself (i.e. the tunneling of the first electron's wave packet) is much smaller than the timescale of the field oscillation, it is less obvious how the timescale after which the ion can be found in its ground state compares to the time difference of the first electron's and the second electron's ionization. The discussion of the "dead times" that can be found in appendix 5.1 suggests that this time difference is much smaller than the timescale of the field (see fig. 5.1) for the laser parameters used in this work. Therefore, the ionization time difference might be comparable to the motion timescale of the ion's electronic state, and the assumption that the second electron is in the ion's ground state before it is ionized again might be poor.

5.2.4 Lateral Momenta in Sequential Ionization

The model for correlated sequential ionization presented in section 4.3 neglects the possible lateral momentum components of the first electron's wave packet after ionization, and only considers a trajectory in z direction. This is a simplifying assumption as the first wave packet has contributions from nonzero lateral momenta as well. In the more realistic case, the effective distance between the first electron's wave packet and the ion is larger, which dampens the Coulomb blockade effect. The fact that nonzero lateral momenta for the trajectory of the second electron are neglected therefore leads to an underestimation of the ionization yield in sequential ionization.

5.2.5 Limitations of the “Effective Distance Approximation”

In order to simplify the 4-dimensional integral in eq. (4.68), the radial coordinate r in the expression

$$e^{ikr}F\left(\frac{i}{\mu k}+l+1,2l+2,-2ikr\right) \tag{5.20}$$

was replaced by an effective value $\bar{r}$. This effective value was determined using eq. (4.69). The physical meaning of this equation is that $\bar{r}$ is calculated as the middle ground between the final state’s radial Coulomb function “pushing” towards larger separations r and the initial state that is confined to a finite radius r_0, a confinement that is amplified by the exponential dependence of the SFA ionization rate on Z. Due to the introduction of this effective value, it was possible to reduce the expression to a 2D integral.

It would be of course a better solution to fully solve the 4D integral, this is however challenging as it has to be done not only once, but for many combinations of initial states, final angular momenta and final momenta[2]. An intermediate approach would be to use an effective $\bar{r}$ that could be chosen depending on some of these parameters, for example depending on the final relative motion parameter k and relative angular momentum l. This could be an efficient starting point for future work to improve the model.

5.2.6 Limitations of the Dipole Approximation

As mentioned in section 2.2.2, the dipole approximation breaks down both in the limit of very short wavelengths and in the limit of very long wavelengths in combination with very large intensities. While the former limit is not an issue when using infrared light, the latter is more problematic. For example, for wavelengths around 3000 nm, the applicability regime of the dipole approximation ends at around $1\times10^{14}\,\mathrm{W/m^2}$ according to [24]. While this intensity is above the over-the-barrier threshold of C_{60} and therefore was not used in this work, intensities close to it have been considered. In the case of the 8000 nm calculations for fig. 3.9 however, the limit intensity is already around $1\times10^{13}\,\mathrm{W/m^2}$, which is below the intensities considered there. Strictly speaking, the dipole approximation is therefore not applicable to this calculation. It should be mentioned however that fig. 3.9 compares the SFA model and the numerical model potential approach, and dipole approximation was used for both approaches.

5.3 Related Work

After finishing this work, the author was pointed to [42], where an analytical approach to the double ionization of Helium in long laser pulses in the quasi-static regime is presented. The differences and similarities between the present

---

[2] Some combinations are equal due to symmetry relations, but the number of combinations is still high.

work and [42] are quite instructive and worth discussing in some more detail.

The approach in [42] consists of different levels of approximation, starting from the strong-field approximation alone. Numerical results are provided for the coarsest level of approximation. This model neglects the simultaneous channel (called "double tunneling" in [42]) altogether, which, for small atoms and long pulse durations, seems justified in light of the conclusions of the present work. The sequential channel on the other hand is modeled in a 2-step model that is very similar to the 3-step model presented in section 4.3.3[3]. In this 2-step model, the single ionization problem in the field is treated in absence of the second electron, and then the time-dependent solution of the first electron is used to derive the ionization dynamics of the second electron. For the description of the second electron's removal, both interactions with the field and interactions with the other electron are taken into account.

So far, this is in accordance with the present work. However, the interaction in the second step is incorporated differently. The interaction of the first electron with the second one is treated as a perturbation to the leading order SFA, following the assumption that "the physics of multi-electron ionization is such that if one electron is in the continuum, the Coulomb repulsion from the other electron is rather weak". Consequently, the interaction of both electrons does not contribute to the ionization potential of the second electron. Instead, the interaction is incorporated as an additional transition matrix element that occurs because of the Coulomb perturbation instead of the external field.

In the present work on the other hand, the interaction energy of the final state is included explicitly (see eq. 4.111), while the transition matrix element of the Coulomb interaction is neglected — the leading order SFA applied to the ionization of the second electron neglects all interactions except for the interaction with the external field. The inclusion of the interaction energy plays an important role, as it modifies the exponential part of the result after application of the saddle point approximation. The interaction energy term is e.g. responsible for the significant difference between the two plots shown in fig. 4.9.

As already mentioned, the model in [42] considers long laser pulses. For such pulses, the probability of a strong interaction of both electrons after ionization is very low, as there is no confinement of the ionization to a short time window. This is in contrast to the present work, where half-cycle pulses are considered. It therefore makes sense that the interaction energy is assumed to be low in [42], while in the present work it is assumed to be significant. The approach in [42] extends on the leading order SFA by incorporating "pre-exponential" correction terms. For short half-cycle pulses, this is a secondary effect, however it might be an interesting addition to include this into the framework for sequential ionization presented in section 4.3.3 as well.

---

[3] Note however that in [42], the term "nonsequential" is used to refer to correlated ionization.

5.4 Conclusion

Inspired by the recent advances in the experimental realization of half-cycle pulses in the infrared regime [10], the objective of this work was to create a model description of the correlated double ionization of C_{60} in such pulses. The expectation was that, due to the short time for which the field is present, the ionization is likely to be correlated, and therefore the final ionization spectrum should exhibit significant features of the Coulomb blockade.

To this end, a method based on the strong-field-approximation (SFA) and the saddle point approximation (SPA) in length gauge and $\Lambda = (0, 0)$-partitioning has been introduced, which allowed for the creation of "almost analytical" models for single ionization, correlated simultaneous double ionization, and correlated sequential double ionization of the C_{60} fullerene.

For the numerically simpler case of single ionization, this approach has been compared to a full numerical solution of the time-dependent Schrödinger equation (TDSE) for a single active electron in a spherical shell model potential, in order to validate the SFA and SPA approximations used. It was found that, while the predicted ionization yields roughly agree on the order of magnitude in the applicable laser regime, there are deviations in the double-logarithmic slopes.

The method was then generalized to the 2-electron case, where it was used to model both simultaneous and sequential double ionization. Indeed, the resulting momentum distributions both exhibit features of the Coulomb blockade. It was found that for the quasi-static laser regime treated in this work, the simultaneous channel is negligible compared to the sequential. This is due to the fact that in sequential ionization, the Coulomb interaction energy of 2 electrons tunneling simultaneously is dictated by the size of the molecule, while the interaction energy of 2 electrons tunneling sequentially can be lower and is only restricted by the duration of the laser pulse. The simultaneous ionization yield mainly depends on the geometry, while the sequential ionization yield is sensitive to the time window during which it can occur. If the pulse duration is sufficiently long, sequential ionization dominates due to smaller ionization potentials.

The models that were developed in this thesis make use of many approximations, which leads to several limitations and weak points. Besides the limitations of the SFA, limitations arising from the fact that multi-body interactions are neglected and non-adiabatic dynamics during sequential ionization are important here, while others are more technical in nature. While some of these limitations are hard to address without using a fundamentally different approach, others could be interesting and efficient starting points for future work to improve on the model. The following section will give suggestions on where some of these starting point could be.

5.5 Outlook

Possibly the most important improvement of both the model for sequential ionization and the model for simultaneous ionization would be to include many-electron polarization effects. This could be done, for example, by considering an effective (perhaps position-dependent) field that includes the shielding of the external field by the polarized molecule (see section (5.2.2)). Furthermore, it could be helpful to find ways to use more realistic assumptions for the electronic structure of C_{60} to begin with. One possible way could be to use eigenstates of a finite shell potential (like the one in section 3.2) as the initial state. In this case however, a 6D integral has to be solved in the case of simultaneous double ionization. It remains to be investigated how this can be done efficiently.

Specifically to the model for simultaneous double ionization, one possible starting point for future work, namely a possible improvement on the “effective-distance-approximation”, has already been discussed in section 5.2.5.

With regard to the model for correlated sequential double ionization, it would be desirable to use a more accurate model for the dynamics of the second electron before its own ejection and after the ejection of the first one. Such a model should include the relaxation of the ion back into its ground state and make an assumption about the state of the ion right after its first ionization. Apart from that, as discussed, the ionization yield in correlated sequential double ionization is underestimated because the trajectory of the first electron is calculated neglecting lateral momenta. Hence, a presumably easy improvement of the model for correlated sequential double ionization would be the incorporation of nonzero lateral momenta into the first electron’s trajectory. In this case, the ionization amplitude of the second electron would not only depend on the $k_{z,1}$ momentum component of the first electron, but also on its $k_{\perp,1}$ momentum component. This will increase the computational complexity, but should be easy to implement in principle.

With regard to the use of more realistic laser pulse shapes, notice that the ionization in the quasi-static limit does not depend on the exact pulse shape (up to a prefactor that can easily be adapted), but only on the field at “tunneling time”. Hence, pulse shapes different from the one assumed in eq. (4.1) can be incorporated into the model without problems, as long as the dynamics remain quasi-static. This can be used to adapt the model to specific laser pulses used in an experiment. Furthermore, considering the sensitivity of the sequential ionization to the duration of the laser pulse, it might be interesting in principle to examine the ionization of C_{60} in half-cycle pulses of shorter wavelength beyond the quasi-static regime. To get a very rough estimate for the regime at which one might expect sequential ionization to become comparable in magnitude to simultaneous ionization, one could ask after which time Δt, given a constant field strength F_0, a classical electron originally at 0 momentum has moved farer than the length scale of C_{60}, i.e. r_0. This time scale is

$$\Delta t = \sqrt{\frac{2r_0}{F_0}} \quad , \tag{5.21}$$

which, for example for the field strength $F_0 = 0.04\,\text{a.u.}$ mainly used in this work, would correspond to a pulse duration of 0.51 fs. For the half cycle shape used in this work, this would correspond to a wavelength of 307 nm.

Appendix A

Code Snippets

The `Python` code used for the calculation of the single, simultaneous double and sequential double ionization in sections 3.1, 4.2, and 4.3 respectively is available via the `github` repository `github.com/ischubert/c_60_coulomb_blockade`[1]. The code used for the TDSE model potential calculation in section 3.2 was a modified version of the `/bsplin/fixbnd/run_bas1e.csh`-code for the electronic structure and `/TIME_PROP/TP_ATOM_1e/RUN_TP_SEQ_ATOM_1e.csh` for the time propagation, both codes being part of the `AMO_TOOLS` from the AMO group at Humboldt-Universität zu Berlin. This modified version will be included in the `AMO_TOOLS`.

It is neither useful nor feasible to give the entire source code here, instead, the following parts of the code are presented:

- Code snippets highlighting central parts of the newly written `Python` codes for
  - Single ionization (analytical approach)
  - Simultaneous double ionization
  - Sequential double ionization
- The modification of the `/bsplin/fixbnd/run_bas1e.csh` code the author wrote to include the spherical shell model potential for the TDSE calculation.

A.1 Python Code for SFA Calculations

A.1.1 Single Ionization

The following function returns the ionization matrix element for single ionization of C_{60} as it was discussed in section 3.1.

```
def b_single(omega,F_0,k_z_vec,k_perp_vec,tau,lvec,step):
    results = np.zeros(
        (len(k_z_vec),len(k_perp_vec),len(lvec)),
        dtype=np.complex
    )
```

---

[1] Please contact the author via ingmar@physik.hu-berlin.de for access rights to the repository.

```
    for ind_k_z,k_z in enumerate(tqdm.tqdm(k_z_vec)):
        for ind_k_perp,k_perp in enumerate(k_perp_vec):
            for ind_l,l in enumerate(lvec):
                results[
                    ind_k_z,
                    ind_k_perp,
                    ind_l
                ] = complete_prefactor_single(
                    omega,F_0,
                    k_z,k_perp,tau,
                    l,step
                ) * x_integral_single(
                    omega,F_0,
                    k_z,k_perp,
                    l,step
                )
    return [
        k_z_vec,
        k_perp_vec,
        lvec,
        results
    ]
```

It makes use of the following functions calculating the integral over x (see eq. (3.51)):

```
def exp_handle_single(omega,F_0,k_z,k_perp,step):
    return lambda x: np.exp(
        - 2/3 * np.sqrt(2*me)/F_of_t_1_single(
            omega,F_0,
            k_z
        ) * (
            tilde_ion_pot_single(
                k_perp,step
            ) + F_of_t_1_single(
                omega,F_0,
                k_z
            ) * a*x
        )**(3/2)
    )

def x_integrand_handle_single(
    omega,F_0,
    k_z,k_perp,
    l,step
):
    exp_handle = exp_handle_single(
        omega,F_0,
```

```
        k_z,k_perp,
        step
    )
    return lambda x: x * scipy.special.lpmn(
        0,l,x
    )[0][-1][-1] * exp_handle(x)

def x_integral_single(omega,F_0,k_z,k_perp,l,step):
    return scipy.integrate.quad(
                    lambda x: x_integrand_handle_single(
                        omega,F_0,
                        k_z,k_perp,
                        l,step
                    )(x),
                    -1,1
    )[0]
```

A.1.2 Simultaneous Double Ionziation

Simultaneous double ionization works quite similar to single ionization, with the complication that there are more different parameters and variables. The following functions perform the integral over x_1 and x_2 (see eq. (4.76)):

```
def x1_x2_integrand_handle(
    omega,F_0,
    K_Z,tilde_ion_pot,
    abs_m1,abs_m2,l,ls
):

    if not (abs_m1>=0 and abs_m2>=0):
        raise(Exception(
            'abs_m1 and abs_m2 have to be'\
            + ' non-negative both, but were ' + str(
                abs_m1
            ) + ' and ' + str(
                abs_m2
            )))

    exp_handle = wkb_factor_with_field_term_as_handle(
        omega,F_0,
        K_Z,tilde_ion_pot
    )

    return lambda x1,x2: (x1+x2)/2 * scipy.special.lpmn(
        abs_m1,l1,x1
    )[0][-1][-1] * scipy.special.lpmn(
        abs_m1,ls,x1
    )[0][-1][-1] * scipy.special.lpmn(
```

```
        abs_m2,l2,x2
    )[0][-1][-1] * scipy.special.lpmn(
        abs_m2,l-ls,x2
    )[0][-1][-1] * exp_handle(x1,x2)

def x1_x2_integral(
    omega,F_0,
    K_Z,tilde_ion_pot,
    abs_m1,abs_m2,l,ls
):
    integrand = x1_x2_integrand_handle(
        omega,F_0,
        K_Z,tilde_ion_pot,
        abs_m1,abs_m2,l,ls
    )
    return scipy.integrate.quad(
                lambda x1:scipy.integrate.quad(
                    lambda x2: integrand(x1,x2),
                    -1,1)[0],
                -1,1)
```

A.1.3 Sequential Double Ionization

The sequential double ionization is constructed from the single ionization using a modified ionization potential that depends on the detected momentum of the first degree of freedom, as discussed in section 4.3.3.3. The following code snippet calculates this conditional ionization, using the function `iFas.b_single` that was already presented.

```
results_2_conditioned_on_k_z_1 = np.zeros((
    len(k_z_vec1),
    *results_2_for_l2.shape
),dtype = np.complex)

for ind_kz_1, [tb1, k_z1] in enumerate(
    zip(tb1vec,k_z_vec1)
):
    for ind_kz_2, [tb2, k_z2] in enumerate(
        zip(tb2vec,k_z_vec2)
    ):
        if tb2>tb1:
            z_now = z_of_t(tb2,tb1)
            step_now = {
                'step': 'second',
                'z_now': z_now
            }
            results_2_conditioned_on_k_z_1[
                ind_kz_1,
```

```
                ind_kz_2,
                :
            ] = iFas.b_single(
                omega,F_0_a_u,
                [k_z2],k_perp_vec,tau,
                lvec2,step_now
            )[-1][0,:,0]
        else:
            results_2_conditioned_on_k_z_1[
                ind_kz_1,
                ind_kz_2,
                :
            ] = np.zeros(
                results_2_conditioned_on_k_z_1.shape[2],
                dtype = np.complex
            )
```

A.2 Fortran Code for TDSE Calculations

As already mentioned, an existent code was used for the model potential TDSE calculations. It was modified to support the model potential used in this work as well. The lines containing the definition of the model potential are shown in the following.

```
C*
C*
C*        IPOLAR = -8: use potential well to describe C60
C*
C*
      IF (ABS(ipolar) .EQ. 8) THEN
        IF (ABS(x-zeta1(1,1)) .LT. gamm2(1,1)/2) THEN
          q = q + 2.0 * gamm1(1,1)
        ELSE
          q = q + 2.0 * 0.0
        ENDIF
      ENDIF
C*
```

Appendix B

B Spline Basis Sets

The basis sets used in section 3.2 denoted by the letters A, B, C, D, and E are presented in the following. The differences between the files lie in the box radius and the number of B splines specified, and are summarized in table 3.1.

B.1 Basis Set A

File name: `fub034s.bsp`

```
*
*
*        Input file for a calculation of the one-electron
*       ==================================================
*        orbitals of the model potential for the c60
*       ==================================================
*
*    Basis A
*   ========
*
*      General parameters:
*     ====================
*
$GENPAR
*
   Nuclear charge Z_nuc:     0.00D+00
*
   Box radius R_max      :    6000.00D+00
*
   Order of the B splines (k):  9
*
*
*      Angular momenta l to be considered:
*     ====================================
*
$ANGPAR
*
   Number of s-, p-, and d-type core orbitals:  0  0  0
*                                              ! Max.: 4  3  1
*
   (l_min+1) and (l_max+1):  1  21
*                          ! (l_max+1) may be overwritten by lcore
*
*
*      Define B splines for the different values of l:
*     ================================================
*      ( Every row must contain l, the number of B splines for
*        that l, and the first non-zero knot of the B-spline
*        sequence for that l.
*        Note: The number of rows must be chosen consistently
*              with the number of l values given above.)
*
   l+1, no. of B splines, 1st non-zero knot:  1   1000   5.0D-02
   l+1, no. of B splines, 1st non-zero knot:  2   1000   5.0D-02
   l+1, no. of B splines, 1st non-zero knot:  3   1000   5.0D-02
   l+1, no. of B splines, 1st non-zero knot:  4   1000   5.0D-02
   l+1, no. of B splines, 1st non-zero knot:  5   1000   5.0D-02
   l+1, no. of B splines, 1st non-zero knot:  6   1000   5.0D-02
   l+1, no. of B splines, 1st non-zero knot:  7   1000   5.0D-02
   l+1, no. of B splines, 1st non-zero knot:  8   1000   5.0D-02
   l+1, no. of B splines, 1st non-zero knot:  9   1000   5.0D-02
   l+1, no. of B splines, 1st non-zero knot:  10          1000   5.0D-02
   l+1, no. of B splines, 1st non-zero knot:  11          1000   5.0D-02
   l+1, no. of B splines, 1st non-zero knot:  12          1000   5.0D-02
   l+1, no. of B splines, 1st non-zero knot:  13          1000   5.0D-02
   l+1, no. of B splines, 1st non-zero knot:  14          1000   5.0D-02
   l+1, no. of B splines, 1st non-zero knot:  15          1000   5.0D-02
   l+1, no. of B splines, 1st non-zero knot:  16          1000   5.0D-02
   l+1, no. of B splines, 1st non-zero knot:  17          1000   5.0D-02
   l+1, no. of B splines, 1st non-zero knot:  18          1000   5.0D-02
```

```
   l+1, no. of B splines, 1st non-zero knot:  19         1000  5.0D-02
   l+1, no. of B splines, 1st non-zero knot:  20         1000  5.0D-02
   l+1, no. of B splines, 1st non-zero knot:  21         1000  5.0D-02
*
*
*     Parameters defining the r grid:
*     ===============================
*
*     ( Define the r grid used, e.g., for numerical integration
*       of the two-electron integrals )
*
$GRDPAR
*
   Number of grid pts., 1st non-zero grid point:  6000  5.0D-06
*
*
*     Parameters defining the polarisation potentials:
*     ================================================
*
$POLPAR
*
   Add polarisation potentials ( 0=no, 1=yes ):  -8   ! if <>1,
*                                                     ! it is
*                                                     ! set to 0.
*
*     If the last question was answered yes(!=0), the polarisation
*     potentials for all values of l have to be defined (but may
*     be set to zero by setting the corresponding alpha(l)=0):
*     Otherwise no(=0), no polarisation potential need to occur!!
*
*     If the last question was answered with a number <0, a model
*     potential has to be defined too.
*
*     If the option -8 is chosen, the width and depth of the model potential has to be defined
*     in the following. Depth in a.u. (=Hartree), width and Radius in a.u. (=Bohr radii)
*
*
   l+1, alpha_{l+1}, rho{l+1}:  1   0.0D+00  1.0D+00
        Number of potential terms:  1
        Potential depth, Potential width, Radius    :    5.800D-01  2.000D-00  6.614D+00
*
   l+1, alpha_{l+1}, rho{l+1}:  2   0.0D+00  1.0D+00
        Number of potential terms:  1
        Potential depth, Potential width, Radius    :    5.800D-01  2.000D-00  6.614D+00
*
   l+1, alpha_{l+1}, rho{l+1}:  3   0.0D+00  1.0D+00
        Number of potential terms:  1
        Potential depth, Potential width, Radius    :    5.800D-01  2.000D-00  6.614D+00
*
   l+1, alpha_{l+1}, rho{l+1}:  4   0.0D+00  1.0D+00
        Number of potential terms:  1
        Potential depth, Potential width, Radius    :    5.800D-01  2.000D-00  6.614D+00
*
   l+1, alpha_{l+1}, rho{l+1}:  5   0.0D+00  1.0D+00
        Number of potential terms:  1
        Potential depth, Potential width, Radius    :    5.800D-01  2.000D-00  6.614D+00
*
   l+1, alpha_{l+1}, rho{l+1}:  6   0.0D+00  1.0D+00
        Number of potential terms:  1
        Potential depth, Potential width, Radius    :    5.800D-01  2.000D-00  6.614D+00
*
   l+1, alpha_{l+1}, rho{l+1}:  7   0.0D+00  1.0D+00
        Number of potential terms:  1
        Potential depth, Potential width, Radius    :    5.800D-01  2.000D-00  6.614D+00
*
   l+1, alpha_{l+1}, rho{l+1}:  8   0.0D+00  1.0D+00
        Number of potential terms:  1
        Potential depth, Potential width, Radius    :    5.800D-01  2.000D-00  6.614D+00
*
   l+1, alpha_{l+1}, rho{l+1}:  9   0.0D+00  1.0D+00
        Number of potential terms:  1
        Potential depth, Potential width, Radius    :    5.800D-01  2.000D-00  6.614D+00
*
   l+1, alpha_{l+1}, rho{l+1}:  10   0.0D+00  1.0D+00
        Number of potential terms:  1
        Potential depth, Potential width, Radius    :    5.800D-01  2.000D-00  6.614D+00
*
   l+1, alpha_{l+1}, rho{l+1}:  11   0.0D+00  1.0D+00
        Number of potential terms:  1
        Potential depth, Potential width, Radius    :    5.800D-01  2.000D-00  6.614D+00
*
   l+1, alpha_{l+1}, rho{l+1}:  12   0.0D+00  1.0D+00
        Number of potential terms:  1
        Potential depth, Potential width, Radius    :    5.800D-01  2.000D-00  6.614D+00
*
   l+1, alpha_{l+1}, rho{l+1}:  13   0.0D+00  1.0D+00
        Number of potential terms:  1
        Potential depth, Potential width, Radius    :    5.800D-01  2.000D-00  6.614D+00
*
   l+1, alpha_{l+1}, rho{l+1}:  14   0.0D+00  1.0D+00
        Number of potential terms:  1
        Potential depth, Potential width, Radius    :    5.800D-01  2.000D-00  6.614D+00
*
   l+1, alpha_{l+1}, rho{l+1}:  15   0.0D+00  1.0D+00
        Number of potential terms:  1
        Potential depth, Potential width, Radius    :    5.800D-01  2.000D-00  6.614D+00
*
```

```
   l+1, alpha_{l+1}, rho{l+1}:  16    0.0D+00   1.0D+00
        Number of potential terms:   1
        Potential depth, Potential width, Radius   :   5.800D-01   2.000D-00   6.614D+00
*
   l+1, alpha_{l+1}, rho{l+1}:  17    0.0D+00   1.0D+00
        Number of potential terms:   1
        Potential depth, Potential width, Radius   :   5.800D-01   2.000D-00   6.614D+00
*
   l+1, alpha_{l+1}, rho{l+1}:  18    0.0D+00   1.0D+00
        Number of potential terms:   1
        Potential depth, Potential width, Radius   :   5.800D-01   2.000D-00   6.614D+00
*
   l+1, alpha_{l+1}, rho{l+1}:  19    0.0D+00   1.0D+00
        Number of potential terms:   1
        Potential depth, Potential width, Radius   :   5.800D-01   2.000D-00   6.614D+00
*
   l+1, alpha_{l+1}, rho{l+1}:  20    0.0D+00   1.0D+00
        Number of potential terms:   1
        Potential depth, Potential width, Radius   :   5.800D-01   2.000D-00   6.614D+00
*
   l+1, alpha_{l+1}, rho{l+1}:  21    0.0D+00   1.0D+00
        Number of potential terms:   1
        Potential depth, Potential width, Radius   :   5.800D-01   2.000D-00   6.614D+00
*
*
*     Parameters for the Hartree-Fock calculation:
*     ============================================
*
*     ( Not needed, if no core orbitals are present, as in a
*       calculation for H, He^+, Li^{2+}, ..., but if they are
*       present in such a case, they will simply be ignored.)
*
$FCHFPR
*
   Convergence criterion, max. number of iterations:  1.0D-9  50
*
*     Define the mixing parameters between the new and the old
*     HF wavefunctions (up to iteration number ID, 100*DI% of
*     the new wavefunction is used, after iteration ID, 100*DF%
*     is used in the next iteration):
*
   Mixing parameters ID, DI, and DF:   10    0.90D+00   0.7D+00
*                                                ! DI,DF .LE. 1.0
*
*
*     Choice of the initial-guess orbitals:
*     =====================================
*       ISL = 1  :   use corresponding hydrogenic wavefunctions
*       ISL = 0  :   read from a previous program run (without
*                    polarisation), the files having standard names
*       ISL<>0,1:    read from a previous program run, but the
*                    file names are given explicitly.
*
   Initial guess parameter ISL:   1
*
*
*     Effective nuclear charges for producing initial-guess
*     hydrogenic wavefunctions for every core orbital (1s,
*     2s, 2p, ...) [Not needed, if ISL<>1]:
*
$EFFZPR
*
   Core-orbital number, eff. nucl. charge:  1   2.0
*
*
*     File names containing the initial orbitals:
*     ( Only needed, if ISL<>0,1 )
*
$FILPAR
*
```

B.2 Basis Set B

Note that while the code has the ability to describe multi-electron systems within the Hartree-Fock approximation, this is not used in section 3.2 since the ionization is treated as an effective one-particle problem here. Therefore, the `$FCHFPR` and `$EFFZPR` sections are left out in the following. The `$POLPAR` section specifies the model potential which was the same for all basis sets, so it can be left out as well.

File name: `fub032s.bsp`

```
*
*
*       Input file for a calculation of the one-electron
*       ================================================
```

```
*        orbitals of the model potential for the c60
*        ============================================
*
*   Basis B
*   =======
*
*     General parameters:
*     ===================
*
$GENPAR
*
   Nuclear charge Z_nuc:    0.00D+00
*
   Box radius R_max     :   3000.00D+00
*
   Order of the B splines (k):  9
*
*
*     Angular momenta l to be considered:
*     ===================================
*
$ANGPAR
*
   Number of s-, p-, and d-type core orbitals:  0  0  0
*                                                 ! Max.: 4  3  1
*
   (l_min+1) and (l_max+1):  1  21
*                            ! (l_max+1) may be overwritten by lcore
*
*
*     Define B splines for the different values of l:
*     ===============================================
*     ( Every row must contain l, the number of B splines for
*       that l, and the first non-zero knot of the B-spline
*       sequence for that l.
*       Note: The number of rows must be chosen consistently
*             with the number of l values given above.)
*
   l+1, no. of B splines, 1st non-zero knot:  1  1000  5.0D-02
   l+1, no. of B splines, 1st non-zero knot:  2  1000  5.0D-02
   l+1, no. of B splines, 1st non-zero knot:  3  1000  5.0D-02
   l+1, no. of B splines, 1st non-zero knot:  4  1000  5.0D-02
   l+1, no. of B splines, 1st non-zero knot:  5  1000  5.0D-02
   l+1, no. of B splines, 1st non-zero knot:  6  1000  5.0D-02
   l+1, no. of B splines, 1st non-zero knot:  7  1000  5.0D-02
   l+1, no. of B splines, 1st non-zero knot:  8  1000  5.0D-02
   l+1, no. of B splines, 1st non-zero knot:  9  1000  5.0D-02
   l+1, no. of B splines, 1st non-zero knot:  10         1000  5.0D-02
   l+1, no. of B splines, 1st non-zero knot:  11         1000  5.0D-02
   l+1, no. of B splines, 1st non-zero knot:  12         1000  5.0D-02
   l+1, no. of B splines, 1st non-zero knot:  13         1000  5.0D-02
   l+1, no. of B splines, 1st non-zero knot:  14         1000  5.0D-02
   l+1, no. of B splines, 1st non-zero knot:  15         1000  5.0D-02
   l+1, no. of B splines, 1st non-zero knot:  16         1000  5.0D-02
   l+1, no. of B splines, 1st non-zero knot:  17         1000  5.0D-02
   l+1, no. of B splines, 1st non-zero knot:  18         1000  5.0D-02
   l+1, no. of B splines, 1st non-zero knot:  19         1000  5.0D-02
   l+1, no. of B splines, 1st non-zero knot:  20         1000  5.0D-02
   l+1, no. of B splines, 1st non-zero knot:  21         1000  5.0D-02
*
*
*     Parameters defining the r grid:
*     ===============================
*
*     ( Define the r grid used, e.g., for numerical integration
*       of the two-electron integrals )
*
$GRDPAR
*
   Number of grid pts., 1st non-zero grid point:  6000  5.0D-06
*
[...]
```

B.3 Basis Set C

File name: `fub033s.bsp`

```
*
*
*        Input file for a calculation of the one-electron
*        ============================================
*        orbitals of the model potential for the c60
*        ============================================
*
*   Basis C
*   =======
*
*     General parameters:
*     ===================
*
$GENPAR
```

```
*
   Nuclear charge Z_nuc:    0.00D+00
*
   Box radius R_max     :   3000.00D+00
*
   Order of the B splines (k):  9
*
*
*     Angular momenta l to be considered:
*     ====================================
*
$ANGPAR
*
   Number of s-, p-, and d-type core orbitals:  0  0  0
*                                              ! Max.: 4  3  1
*
   (l_min+1) and (l_max+1):  1  21
*                          ! (l_max+1) may be overwritten by lcore
*
*
*     Define B splines for the different values of l:
*     ================================================
*     ( Every row must contain l, the number of B splines for
*       that l, and the first non-zero knot of the B-spline
*       sequence for that l.
*       Note: The number of rows must be chosen consistently
*             with the number of l values given above.)
*
   l+1, no. of B splines, 1st non-zero knot:  1  2000  5.0D-02
   l+1, no. of B splines, 1st non-zero knot:  2  2000  5.0D-02
   l+1, no. of B splines, 1st non-zero knot:  3  2000  5.0D-02
   l+1, no. of B splines, 1st non-zero knot:  4  2000  5.0D-02
   l+1, no. of B splines, 1st non-zero knot:  5  2000  5.0D-02
   l+1, no. of B splines, 1st non-zero knot:  6  2000  5.0D-02
   l+1, no. of B splines, 1st non-zero knot:  7  2000  5.0D-02
   l+1, no. of B splines, 1st non-zero knot:  8  2000  5.0D-02
   l+1, no. of B splines, 1st non-zero knot:  9  2000  5.0D-02
   l+1, no. of B splines, 1st non-zero knot:  10          2000  5.0D-02
   l+1, no. of B splines, 1st non-zero knot:  11          2000  5.0D-02
   l+1, no. of B splines, 1st non-zero knot:  12          2000  5.0D-02
   l+1, no. of B splines, 1st non-zero knot:  13          2000  5.0D-02
   l+1, no. of B splines, 1st non-zero knot:  14          2000  5.0D-02
   l+1, no. of B splines, 1st non-zero knot:  15          2000  5.0D-02
   l+1, no. of B splines, 1st non-zero knot:  16          2000  5.0D-02
   l+1, no. of B splines, 1st non-zero knot:  17          2000  5.0D-02
   l+1, no. of B splines, 1st non-zero knot:  18          2000  5.0D-02
   l+1, no. of B splines, 1st non-zero knot:  19          2000  5.0D-02
   l+1, no. of B splines, 1st non-zero knot:  20          2000  5.0D-02
   l+1, no. of B splines, 1st non-zero knot:  21          2000  5.0D-02
*
[...]
```

B.4 Basis Set D

File name: `fub036s.bsp`

```
*
*
*       Input file for a calculation of the one-electron
*       =================================================
*       orbitals of the model potential for the c60
*       =================================================
*
*   Basis D
*   =======
*
*     General parameters:
*     ===================
*
$GENPAR
*
   Nuclear charge Z_nuc:    0.00D+00
*
   Box radius R_max     :   600.00D+00
*
   Order of the B splines (k):  9
*
*
*     Angular momenta l to be considered:
*     ====================================
*
$ANGPAR
*
   Number of s-, p-, and d-type core orbitals:  0  0  0
*                                              ! Max.: 4  3  1
*
   (l_min+1) and (l_max+1):  1  21
*                          ! (l_max+1) may be overwritten by lcore
*
*
*     Define B splines for the different values of l:
```

```
*     ==============================================
*     ( Every row must contain l, the number of B splines for
*       that l, and the first non-zero knot of the B-spline
*       sequence for that l.
*       Note: The number of rows must be chosen consistently
*             with the number of l values given above.)
*
   l+1, no. of B splines, 1st non-zero knot:  1  1000  5.0D-02
   l+1, no. of B splines, 1st non-zero knot:  2  1000  5.0D-02
   l+1, no. of B splines, 1st non-zero knot:  3  1000  5.0D-02
   l+1, no. of B splines, 1st non-zero knot:  4  1000  5.0D-02
   l+1, no. of B splines, 1st non-zero knot:  5  1000  5.0D-02
   l+1, no. of B splines, 1st non-zero knot:  6  1000  5.0D-02
   l+1, no. of B splines, 1st non-zero knot:  7  1000  5.0D-02
   l+1, no. of B splines, 1st non-zero knot:  8  1000  5.0D-02
   l+1, no. of B splines, 1st non-zero knot:  9  1000  5.0D-02
   l+1, no. of B splines, 1st non-zero knot:  10         1000  5.0D-02
   l+1, no. of B splines, 1st non-zero knot:  11         1000  5.0D-02
   l+1, no. of B splines, 1st non-zero knot:  12         1000  5.0D-02
   l+1, no. of B splines, 1st non-zero knot:  13         1000  5.0D-02
   l+1, no. of B splines, 1st non-zero knot:  14         1000  5.0D-02
   l+1, no. of B splines, 1st non-zero knot:  15         1000  5.0D-02
   l+1, no. of B splines, 1st non-zero knot:  16         1000  5.0D-02
   l+1, no. of B splines, 1st non-zero knot:  17         1000  5.0D-02
   l+1, no. of B splines, 1st non-zero knot:  18         1000  5.0D-02
   l+1, no. of B splines, 1st non-zero knot:  19         1000  5.0D-02
   l+1, no. of B splines, 1st non-zero knot:  20         1000  5.0D-02
   l+1, no. of B splines, 1st non-zero knot:  21         1000  5.0D-02
*
[...]
```

B.5 Basis Set E

File name: `fub035s.bsp`

```
*
*
*       Input file for a calculation of the one-electron
*       ==============================================
*       orbitals of the model potential for the c60
*       ==============================================
*
*   Basis E
*   =======
*
*     General parameters:
*     ===================
*
$GENPAR
*
   Nuclear charge Z_nuc:    0.00D+00
*
   Box radius R_max     :   600.00D+00
*
   Order of the B splines (k):  9
*
*
*     Angular momenta l to be considered:
*     ===================================
*
$ANGPAR
*
   Number of s-, p-, and d-type core orbitals:  0  0  0
*                                                 ! Max.: 4  3  1
*
   (l_min+1) and (l_max+1):  1  21
*                            ! (l_max+1) may be overwritten by lcore
*
*
*     Define B splines for the different values of l:
*     ==============================================
*     ( Every row must contain l, the number of B splines for
*       that l, and the first non-zero knot of the B-spline
*       sequence for that l.
*       Note: The number of rows must be chosen consistently
*             with the number of l values given above.)
*
   l+1, no. of B splines, 1st non-zero knot:  1  3000  5.0D-02
   l+1, no. of B splines, 1st non-zero knot:  2  3000  5.0D-02
   l+1, no. of B splines, 1st non-zero knot:  3  3000  5.0D-02
   l+1, no. of B splines, 1st non-zero knot:  4  3000  5.0D-02
   l+1, no. of B splines, 1st non-zero knot:  5  3000  5.0D-02
   l+1, no. of B splines, 1st non-zero knot:  6  3000  5.0D-02
   l+1, no. of B splines, 1st non-zero knot:  7  3000  5.0D-02
   l+1, no. of B splines, 1st non-zero knot:  8  3000  5.0D-02
   l+1, no. of B splines, 1st non-zero knot:  9  3000  5.0D-02
   l+1, no. of B splines, 1st non-zero knot:  10         3000  5.0D-02
   l+1, no. of B splines, 1st non-zero knot:  11         3000  5.0D-02
   l+1, no. of B splines, 1st non-zero knot:  12         3000  5.0D-02
   l+1, no. of B splines, 1st non-zero knot:  13         3000  5.0D-02
   l+1, no. of B splines, 1st non-zero knot:  14         3000  5.0D-02
```

```
    l+1, no. of B splines, 1st non-zero knot:  15          3000  5.0D-02
    l+1, no. of B splines, 1st non-zero knot:  16          3000  5.0D-02
    l+1, no. of B splines, 1st non-zero knot:  17          3000  5.0D-02
    l+1, no. of B splines, 1st non-zero knot:  18          3000  5.0D-02
    l+1, no. of B splines, 1st non-zero knot:  19          3000  5.0D-02
    l+1, no. of B splines, 1st non-zero knot:  20          3000  5.0D-02
    l+1, no. of B splines, 1st non-zero knot:  21          3000  5.0D-02
*
[...]
```

Bibliography

[1] J. R. Oppenheimer, "Three notes on the quantum theory of aperiodic effects", Phys. Rev. **31**, 66–81 (1928).

[2] T. H. Maiman, "Stimulated optical radiation in ruby", Nature **187**, 493–494 (1960).

[3] W. Sibbett, A. A. Lagatsky, and C. T. A. Brown, "The development and application of femtosecond laser systems", Opt. Express **20**, 6989–7001 (2012).

[4] National Center for Biotechnology Information, *Pubchem compound database; cid 123591*, `https://pubchem.ncbi.nlm.nih.gov/compound/123591` (visited on 10/19/2018).

[5] H. W. Kroto, J. R. Heath, S. C. O'Brien, R. F. Curl, and R. E. Smalley, "C_{60}: Buckminsterfullerene", Nature **318**, 162 (1985).

[6] A. Goel, J. B. Howard, and J. B. V. Sande, "Size analysis of single fullerene molecules by electron microscopy", Carbon **42**, 1907 –1915 (2004).

[7] A. V. Pogulay, R. R. Abzalimov, S. Nasibullaev, A. S. Lobach, T. Drewello, and Y. V. Vasil'Ev, "Ionization energies of the C_{60} fullerene and its hydrogenated derivatives $C_{60}H_{18}$ and $C_{60}H_{36}$ determined by electron ionization", Int. J. Quant. Chem. **233**, 165–172 (2004).

[8] V. Bhardwaj, P B Corkum, and D M Rayner, "Internal laser-induced dipole force at work in C_{60} molecule", Phys. Rev. Lett. **91**, 203004 (2003).

[9] V. Bhardwaj, P B Corkum, and D M Rayner, "Recollision during the high laser intensity ionization of C_{60}", Phys. Rev. Lett. **93**, 043001 (2004).

[10] T. J. Hammond, D. M. Villeneuve, and P. B. Corkum, "Producing and controlling half-cycle near-infrared electric-field transients", Optica **4**, 826–830 (2017).

[11] A. Saenz, "Molecular hydrogen exposed to a suddenly turned-on strong electric field or low-frequency laser", J. Phys. B **33**, 3519–3530 (2000).

[12] A. Saenz, "Photoabsorption and photoionization of HeH^+", Phys. Rev. A **67**, 033409 (2003).

[13] M. Awasthi, Y. V. Vanne, and A. Saenz, "Non-perturbative solution of the time-dependent Schrödinger equation describing H_2 in intense short laser pulses", J. Phys. B **38**, 3973–3985 (2005).

[14] Y. V. Vanne and A. Saenz, "Ionization of molecular hydrogen and deuterium by frequency-doubled Ti:sapphire laser pulses", Phys. Rev. A **80**, 053422 (2009).

[15] J. Förster, Y. V. Vanne, and A. Saenz, "Ionization behavior of molecular hydrogen in intense laser fields: influence of molecular vibration and alignment", Phys. Rev. A **90**, 053424 (2014).

[16] M. R. Savina, L. L. Lohr, and A. H. Francis, “A particle-on-a-sphere model for C_{60}”, Chem. Phys. Lett. **205**, 200 –206 (1993).

[17] Q. C. Qiu and A. Ceulemans, “Icosahedral symmetry adaptation of $|JM\rangle$ bases”, Mol. Phys. **100**, 255–264 (2002).

[18] I. J. Schoenberg, “Contributions to the problem of approximation of equidistant data by analytic functions: Part A. — On the problem of smoothing or graduation. A first class of analytic approximation formulae”, Quart. Appl. Math. **4**, 45–99 (1946).

[19] H. Bachau, E. Cormier, P. Decleva, J. E. Hansen, and F. Martín, “Applications of B-splines in atomic and molecular physics”, Rep. Prog. Phys. **64**, 1815–1943 (2001).

[20] C. de Boor, *A practical guide to spline*, Vol. 27 (Springer, 1978).

[21] Y. V. Vanne, “Ionization of molecular hydrogen in ultrashort intense laser pulses”, PhD thesis (Humboldt-Universität zu Berlin, Mathematisch - Naturwissenschaftliche Fakultät I, 2010).

[22] A. Saenz and P Lambropoulos, “Theoretical two-, three- and four-photon ionization cross sections of helium in the XUV range”, J. Phys. B **32**, 5629 (1999).

[23] X. Tang, H. Rudolph, and P. Lambropoulos, “Nonperturbative time-dependent theory of helium in a strong laser field”, Phys. Rev. A **44**, R6994–R6997 (1991).

[24] A. Ludwig, J. Maurer, B. W. Mayer, C. R. Phillips, L. Gallmann, and U. Keller, “Breakdown of the dipole approximation in strong-field ionization”, Phys. Rev. Lett. **113**, 243001 (2014).

[25] L. V. Keldysh, “Ionization in the field of a strong electromagnetic wave”, Sov. Phys. JETP **20**, 1307 (1965).

[26] M. Awasthi, Y. V. Vanne, and A. Saenz, “Non-perturbative solution of the time-dependent Schrödinger equation describing H_2 in intense short laser pulses”, J. Phys. B **38**, 3973–3985 (2005).

[27] F. H. M. Faisal, “Multiple absorption of laser photons by atoms”, J. Phys. B **6**, L89–L92 (1973).

[28] H. R. Reiss, “Effect of an intense electromagnetic field on a weakly bound system”, Phys. Rev. A **22**, 1786–1813 (1980).

[29] D. M. Wolkow, “Über eine Klasse von Lösungen der Diracschen Gleichung”, Z. Phys. **94**, 250–260 (1935).

[30] B. Riemann, *Gesammelte Mathematische Werke*, 2nd ed. (1892), pp. 424–430.

[31] T. Oliphant, *Guide to NumPy* (Trelgol Publishing, 2006).

[32] K. C. Kulander and T. N. Rescigno, “Effective potentials for time-dependent calculations of multiphoton processes in atoms”, Comp. Phys. Comm. **63**, 523 (1991).

[33] M. Awasthi, Y. V. Vanne, A. Saenz, A. Castro, and P. Decleva, “Single-active-electron approximation for describing molecules in ultrashort laser pulses and its application to molecular hydrogen”, Phys. Rev. A **77**, 063403 (2008).

[34] M. Awasthi and A. Saenz, "Breakdown of the single-active-electron approximation for one-photon ionization of the $B^1\Sigma_u^+$ state of H_2 exposed to intense laser fields", Phys. Rev. A **81**, 063406 (2010).

[35] E. Jones, T. Oliphant, P. Peterson, et al., *SciPy: Open source scientific tools for Python*, `http://www.scipy.org/` (visited on 03/14/2019).

[36] L. D. Landau and E. M. Lifschitz, *Lehrbuch der theoretischen Physik*, 7th ed., Vol. 3 (Akademie-Verlag Berlin, 1979) Chap. 5, pp. 101–129.

[37] M. van Gelderen, "The shift operators and translations of spherical harmonics", DEOS Prog. Lett. **98**, 75–67 (1998).

[38] J. F. Rico, R. López, I. Ema, and G. Ramírez, "Translation of real solid spherical harmonics", Int. J. Quant. Chem. **113**, 1544–1548 (2013).

[39] Github Username fedro4, *Github repository "specfunc"*, `https://github.com/fedro4/specfunc` (visited on 03/27/2019).

[40] J. Bauer, "Low-frequency–high-intensity limit of the Keldysh-Faisal-Reiss theory", Phys. Rev. A **73**, 023421 (2006).

[41] D. J. Griffiths, *Introduction to electrodynamics: Pearson New International Edition* (Pearson Education M.U.A., 2014), pp. 145–147.

[42] A Heinrich, M Lewenstein, and A Sanpera, "Nonsequential double ionization of helium in low-frequency laser fields", J. Phys. B **37**, 2087–2102 (2004).

Acknowledgements

I would like to thank my supervisors, Prof. Dr. Alejandro Saenz and Prof. Dr. Thomas Brabec, for many stimulating discussions, for their constructive criticism, and for their support. I also would like to thank the AMO group members at the Humboldt-Universität zu Berlin and the group members at the University of Ottawa for fruitful discussions and for creating an enjoyable work atmosphere.

I would like to thank the *Studienstiftung des deutschen Volkes* for the material and non-material support during my Bachelor and Master studies, and for making possible my stay in Ottawa.

Last but not least, I would like to thank my girlfriend Dominique for her loving support.

Selbstständigkeitserklärung

Declaration of Authorship

Ich, Ingmar Fabian Schubert, erkläre hiermit, dass ich die vorliegende Arbeit selbstständig verfasst und noch nicht für andere Prüfungen eingereicht habe. Sämtliche Quellen einschließlich Internetquellen, die unverändert oder abgewandelt wiedergegeben werden, insbesondere Quellen für Texte, Grafiken, Tabellen und Bilder, sind als solche kenntlich gemacht. Mir ist bekannt, dass bei Verstößen gegen diese Grundsätze ein Verfahren wegen Täuschungsversuchs bzw. Täuschung eingeleitet wird.

Berlin, den